Study of Zeeman Coherences in Atomic Rubidium using a Laguerre Gaussian beam

A THESIS

submitted by

J. Anupriya

for the award of the degree

of

DOCTOR OF PHILOSOPHY

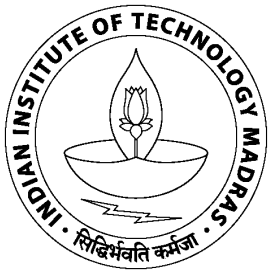

DEPARTMENT OF PHYSICS

INDIAN INSTITUTE OF TECHNOLOGY MADRAS

May 2012

To my father, Mr.V. S. Jayakumar; my mother, Mrs. J. Latha; my brother, J. Karthik Srinivas and my dear husband, K. Kalyanaraman

THESIS CERTIFICATE

This is to certify that the thesis titled **Study of Zeeman Coherences in Atomic Rubidium Using a Laguerre Gaussian Beam**, submitted by **J. Anupriya**, to the Indian Institute of Technology Madras, for the award of the degree of **Doctor of Philosophy**, is a bonafide record of the research work done by her under my supervision. The contents of this thesis, in full or in parts, have not been submitted to any other Institute or University for the award of any degree or diploma.

Dr. M. Pattabiraman
Research Guide
Assistant Professor
Dept. of Physics
IIT Madras, Chennai 600 036

Place: Chennai

ACKNOWLEDGMENTS

I would like to thank my guide Dr. M. Pattabiraman for his continued support, patience, encouragement and guidance during these past five years of my graduate career both at times of ups and downs. I would cherish all the extensive scientific discussions that I had with him during my stay in his lab. I would also like to acknowledge the help of my doctoral committee members, Dr. V. Sanakaranarayanan, Dr. M.V.Satyanarayana, Dr. Anil Prabhakar and Dr. K. Mangala Sunder for their continuous mentoring through my doctoral committee meetings.

I am grateful to Dr.Andal Narayanan and her group members at Raman Research Institute - Preethi, Manoj, Asha, Meena and Parvathi for letting me use their resources for my projects. Meena helped me with the electronics associated with the ECDL unit. Dr.Andal Narayanan, Preeti and Asha have been very receptive to my phone calls whenever I had some problems with the laser.

Dr.Vasanth Natarajan, Indian Institute of Science, was very kind to permit me to do experiments in his lab and his valuable comments on my work were very helpful. I met some wonderful friends Shivi Shetty, Samyudatha, Santhosh and Durgesh who made my stay in IISc Bangalore a memorable one. I can never forget the time spent with them.

It was a pleasure working along with my colleague, Dr.Nibedita Ram who has been a good lab partner and guided me in the initial years in the lab.

My scientific discussions with Dr. Novikova over emails helped me a lot in understanding certain concepts such as the extraction of contributions to the higher order coherence in the ellipticity dependent nonlinear magneto-optical rotation measurements.

IIT Madras has been a second home to me. The faculty of the physics department has always been around to guide me, particularly Dr. R. Nirmala, who has always been there with a warm smile to boost my spirits. I would also like to thank Dr. Shanti Bhattacharya and Dr. M. P. Kothiyal for their valuable suggestions in regards to optical alignment.

I cannot forget my interactions with late Ms. Sumathy in the electronics department. I want to thank Senthi from the photograph section for fabricating the computer generated hologram that was used to create the Laguerre Gaussian beam.

Finally, I would like to thank my family - my father, my mother, my brother and my husband, for without their support, encouragement, guidance, love and co-operation, I would not be here writing this acknowledgement. A special thanks to my father for letting my mother stay with me throughout the course of my Ph.D. Many thanks to my mother, my friend for having stayed with me and having accompanied me to my lab during late nights. It's a blessing to have parents like them who have been a pillar of support in all my ordeals. I can also never forget the constant push and encouragement given by my husband, whenever my spirits were down, instilling immense confidence in me.

ABSTRACT

KEYWORDS: Laguerre Gaussian (LG) beam; Zeeman coherence; Hanle effect; Electromagnetically induced transparency (EIT); Electromagnetically induced absorption (EIA); Nonlinear magneto optical rotation (NMOR); Transfer of coherence (TOC); Higher order coherence (HOC); Linewidth.

This thesis focuses on the interaction of the Rubidium (Rb) atoms with a coherent Laguerre-Gaussian (LG) optical field with spatially varying phase factor and mode amplitude. Detailed computational and experimental studies have been carried out to understand the effect of the LG field on Zeeman coherence induced phenomena like electromagnetically induced transparency (EIT), electromagnetically induced absorption (EIA) and nonlinear magneto-optical rotation (NMOR). The LG beam brings about a significant narrowing in the line shapes of EIT and EIA resonances (measured in Hanle configuration) compared to a Gaussian beam. This narrowing is attributed to the azimuthal mode index of the LG field suggesting that optical fields with non-zero orbital angular momentum (OAM) produce long-lived Zeeman coherences.

Resonant NMOR profiles with widths limited by the atomic transit time are also narrower when measured with a LG beam. However NMOR profiles with widths limited by spin-exchange collisions do not exhibit such a narrowing. Thus the spatial profile of the LG field influences resonance line shapes only if the relaxation time is dependent on spatial coordinates as in transit time relaxation.

The influence of the LG field on higher order Zeeman coherences (with $\Delta m \geq \pm 2$) has been investigated by carrying out ellipticity dependent polarization measurement as a function of laser detuning. This study enables us to extract the contribution of higher order Zeeman coherences from the measured data and shows that EIA systems (driven by excited state coherences) couple differently with the LG field compared to EIT systems (driven by ground state coherences).

TABLE OF CONTENTS

LIST OF TABLES

LIST OF FIGURES

ABBREVIATIONS

BS	Beam Splitter
CGH	Computer Generated Hologram
CRO	Cathode Ray Oscilloscope
DFWM	Degenerate Four-Wave Mixing
ECDL	External Cavity Diode Laser
EIT	Electromagnetically Induced Transparency
EIA	Electromagnetically Induced Absorption
FWM	Four-Wave Mixing
GP	Glass Plate
HOC	Higher Order Coherence
HWP	Half Wave Plate
LG	Laguerre Gaussian
NMOR	Nonlinear Magneto-optical Rotation
OAM	Orbital Angular Momentum
OBE	Optical Bloch Equations
PBS	Polarizing Beam Splitter
PD	Photo Diode
QWP	Quarter Wave Plate
RS	Ring-shaped
RWA	Rotating Wave Approximation
SAS	Saturation Absorption Spectroscopy
TOC	Transfer of Coherence

NOTATION

$\vec{E}$	Electric field
$\vec{B}$	Magnetic field
e	Charge of the electron
$\vec{A}(\vec{r},t)$	Vector potential
$\Phi(\vec{r},t)$	Scalar potential
$\wp$	Gauge function
H	Hamiltonian
$\vec{d}$	Dipole matrix element
ρ	Density matrix
ψ	Wave function
$\vec{k}$	Wave vector
χ	Atomic susceptibility
L	Total orbital angular momentum of electron
S	Total spin angular momentum of electron
J	Total angular momentum of electron
F	Total angular momentum of the atom
I	Nuclear spin
m_F	Magnetic quantum number
Ω	Rabi frequency
ε	Ellipticity

λ	Wavelength of the laser
γ	Decoherence rate
c	Velocity of light
Γ	Spontaneous decay rate
n	Refractive index
ω	Frequency of laser
h	Planck's constant
g	Gyromagnetic ratio
μ_B	Bohr magneton
ω_L	Larmor frequency
I	Intensity of laser beam
I_{sat}	Saturation intensity
φ	Nonlinear magneto-optical rotation
z_R	Rayleigh length
$w(z)$	Beam waist
w_o	Beam width
$\Theta_{klp}(\vec{R})$	Phase factor
$\varepsilon_{klp}(\vec{R})$	Mode amplitude
l	Azimuthal mode index
p	Radial mode index

CHAPTER 1

Introduction

The interference of atomic wave functions in the presence of a coherent optical field results in the creation of coherence among the atomic states. Optical field induced coherences among the ground or excited state Zeeman sublevels of a hyperfine state are referred to as Zeeman coherences. The narrow transparency window or absorption in the probe absorption profile brought about by these coherences are responsible for interesting phenomena like Hanle electromagnetically induced transparency/absorption (EIT/EIA), nonlinear magneto-optical rotation (NMOR) etc. (Renzoni *et al.*, 2001; McLeant *et al.*, 1985; Barkov *et al.*, 1989; Budker *et al.*, 2002).

The influence of a spatially varying optical field on such coherent phenomenon is not well understood. This thesis focuses on Zeeman coherences created in the presence of a coherent Laguerre-Gaussian (LG) optical field with spatially varying phase factor and mode amplitude. The LG field which has a doughnut-shaped intensity distribution and zero intensity at the beam center is obtained as a solution of the paraxial wave function in cylindrical coordinates (Allen *et al.*, 1992; Friese *et al.*, 1996). It has a helical phase structure and carries an orbital angular momentum (OAM) of $l\hbar$ per photon along their direction of propagation, in addition to the spin angular momentum depending upon the polarization ($l = \pm1, \pm2,\ldots$ is the azimuthal mode index and denotes order of the LG beam) (Allen *et al.*, 1992; Friese *et al.*, 1996).

The first work on beams with phase or screw dislocations was carried out by Nye and Berry in 1974 where they had talked about dislocations in the wave trains and shown that at the vortex the phase is indeterminate, with the wave amplitude being zero. Vaughan and Willet had examined the TEM_{01}^{*} (superposition of TEM_{01} and TEM_{10} mode) doughnut mode having a helical wave front by frequency analysis and two beam interference techniques (Vaughan and Willetts, 1979; Willetts and Vaughan, 1980; Vaughan and Willetts, 1983). Bazhenov *et al.*

(1990) were the first to produce and study the properties of higher orders of coherent optical fields with wave-front dislocations by using amplitude holograms. They show that when the singularity of the helical wave front (left or right handed) was circumvented, it resulted in producing phase shifts in multiples of 2π. The right and the left handed screw dislocation was found to wind in opposite directions. Optical vortices and phase structured beams were also investigated by Tamm and Weiss (1990) and Harris *et al.* (1994). In all of these studies it was shown that the helical wave front with a singularity arises due to the presence of phase dislocation. Allen *et al.* (1992) were the first one to realize that the helically phased beams (LG beam) has azimuthal angular dependence of $\exp(il\phi)$ where '*l*' is known as the azimuthal mode index or the topological charge and these beam carry an OAM of $l\hbar$ per photon along their direction of propagation. The azimuthal phase index '*l*' corresponds to the phase variation in units of 2π, i.e. the number of 2π phase cycles around the mode circumference (Allen *et al.*, 1992; Arlt *et al.*, 2001). A detailed review on phase structured light can be found in Allen *et al.* (2003) and Andrews (2008).

1.1 Objectives and scope of this work

The optical forces and torque exerted by the LG beam on particles and atoms have been studied extensively and find interesting applications in cooling and trapping of atoms (Friese *et al.*, 1996; Allen *et al.*, 1996; Tabosa and Petrov, 1999). Nonlinear optical studies like the second harmonic generation with higher order LG beams have been reported (Courtial *et al.*, 1997). The rotational frequency shifts induced by the LG beam due to its azimuthal phase dependence have been observed (Allen *et al.*, 1994; Basistiy *et al.*, 2003; Barreiro *et al.*, 2006). Theoretical studies of force and mechanical torque exerted by OAM associated with the LG beam on a two and three-level atomic systems have also been reported (Power *et al.*, 1995; Allen *et al.*, 1996; Lembessis, 1999).

However, the influence of the LG beam on the atomic coherence and the associated spectroscopic phenomena like Hanle EIT/EIA and NMOR is not well known. This thesis focusses on the interaction of the Rubidium (Rb) atoms with a coherent LG optical field with spatially varying phase factor and mode amplitude. Detailed computational and experimental studies have been carried out to understand the effect of the LG field on the Zeeman coherences

arising as a result of such an atom-field interaction. For this purpose, the various Zeeman coherence induced phenomena like Hanle electromagnetically induced transparency (EIT) and electromagnetically induced absorption (EIA) and magneto-optical rotation in the Faraday and the Voigt geometry has been investigated in the presence of the LG beam.

The introductory chapter gives a brief introduction to the basic concepts of atom field interaction followed by density matrix formalism for a two-level atomic system. Optical/ Zeeman coherence induced phenomena like EIT, EIA, Hanle effect, NMOR have been described here. This chapter also covers the experimental details that have been involved in this work, like Rubidium (Rb) atoms, external cavity diode laser (ECDL), saturation absorption spectroscopy (SAS), Laguerre Gaussian (LG) beam, generation of LG beam.

Chapter 2 describes a computational and experimental study on Hanle electromagnetically induced transparency and absorption resonance line shapes with a LG beam. Two-beam Hanle measurement was carried out where the Hanle profile was measured with a Gaussian beam in the presence of the LG beam. To understand the influence of the LG field on the transit effect limited phenomena, a comparative study has been carried out with a ring shaped beam with zero OAM.

Chapter 3 presents the NMOR-I and II measurements that were carried out with the LG field. The nonlinear magneto-optical rotation response of the $Rb^{87}(F_g=2\rightarrow F_e'=3)$ transition with magnetic field applied parallel (Faraday geometry) and perpendicular (Voigt geometry) to the probe field (Gaussian or LG) direction has been studied. To investigate other manifestations of the LG field influence, a computational analysis was carried out with a lambda (Λ) system to study EIT and reduced group velocity in the presence of the LG beam.

Chapter 4 discusses ellipticity dependent polarization rotation measurements with a LG beam. The influence of the LG beam on higher order Zeeman coherences (with $\Delta m \geq \pm 2$) is studied by extracting their contribution from the measured data.

Chapter 5 presents a summary and highlights of the research work along with possible future proposals.

1.2 Atom field interaction

This thesis is primarily based on the interaction of LG optical field with Rb atoms and hence a brief introduction to the basic concept of atom field interaction is discussed in this section.

The minimum-coupling Hamiltonian (the particle is minimally coupled with the electro-magnetic field) associated with an electron of charge, $q=-e$ and mass m interacting with the external magnetic field is given by (Scully and Zubairy, 1997; Gerry and Night, 2005)

$$H=\frac{1}{2m}\left(\vec{p}+e\vec{A}\left(\vec{r},t\right)\right)^2-e\Phi\left(\vec{r},t\right)+V(r), \tag{1.1}$$

where, $\vec{A}\left(\vec{r},t\right)$ and $\Phi\left(\vec{r},t\right)$ are the vector and the scalar potential of the electromagnetical field respectively, $V(r)$ is the electrostatic potential (atom binding potential) and $\vec{p}$ is the canonical momentum operator.

The electric and the magnetic fields can be described in terms of the gauge dependent potentials as follows

$$\left.\begin{aligned}\vec{E}\left(\vec{r},t\right)&=-\nabla\Phi\left(\vec{r},t\right)-\frac{\partial\vec{A}\left(\vec{r},t\right)}{\partial t}\\ \vec{B}\left(\vec{r},t\right)&=-\nabla\times\vec{A}\left(\vec{r},t\right)\end{aligned}\right\}. \tag{1.2}$$

The electric and the magnetic fields are invariant under the following gauge transformation

$$\left.\begin{aligned}\vec{A}'\left(\vec{r},t\right)&=\vec{A}\left(\vec{r},t\right)+\nabla\wp\left(\vec{r},t\right)\\ \Phi'\left(\vec{r},t\right)&=\Phi\left(\vec{r},t\right)-\frac{\partial\wp\left(\vec{r},t\right)}{\partial t}\end{aligned}\right\}, \tag{1.3}$$

where, $\wp$ is the Gauge function and the choice of gauge in this case is the coulomb (radiation) gauge as it has the advantage of completely describing the radiation field by the vector potential. The Coulomb gauge, where the charge is conserved, is described as follows

$$\nabla.\vec{A}\left(\vec{r},t\right)=0 \quad \text{(Transversality condition)} \tag{1.4a}$$

$$\Phi(\vec{r},t)=0. \tag{1.4b}$$

After applying the gauge transformation, the Hamiltonian can be re-written as

$$H'=\frac{1}{2m}\left(\vec{p}+e\left\{\vec{A}(\vec{r},t)+\nabla\wp(\vec{r},t)\right\}\right)^2-e\left[\Phi(\vec{r},t)-\frac{\partial\wp(\vec{r},t)}{\partial t}\right]+V(r). \tag{1.5}$$

The vector potential satisfies the wave equation

$$\nabla^2\vec{A}(\vec{r},t)-\frac{1}{c^2}\frac{\partial^2\vec{A}(\vec{r},t)}{\partial t^2}=0. \tag{1.6}$$

And the solution of the wave equation is given by

$$\vec{A}(\vec{r},t)=A_0\hat{\varepsilon}\exp\left[i\left(\vec{k}\cdot\vec{r}-\omega t\right)\right]. \tag{1.7}$$

On separating out the time and the space coordinates, the vector potential can be written as

$$\vec{A}(\vec{r},t)=A_0\hat{\varepsilon}\exp[-i\omega t]\exp\left[i\vec{k}\cdot\vec{r}\right] \tag{1.8}$$

$$\Rightarrow\vec{A}(\vec{r},t)=A(t)\exp\left[i\vec{k}\cdot\vec{r}\right]. \tag{1.9}$$

The exponential term of (1.9) can be expanded as

$$\exp\left[i\vec{k}\cdot\vec{r}\right]=1+i\vec{k}\cdot\vec{r}+\frac{\left(i\vec{k}\cdot\vec{r}\right)^2}{2!}+..... \tag{1.10}$$

Making the dipole approximation where the atomic dimension is much smaller than the optical wavelength i.e. $\vec{k}\cdot\vec{r}<<1$ (Louden, 1983). Hence (1.10) reduces as

$$\exp\left[i\vec{k}\cdot\vec{r}\right]\approx 1;\ \vec{A}(\vec{r},t)=A(t). \tag{1.11}$$

And $\wp$ is chosen such that the following conditions are satisfied

$$\wp(\vec{r},t)=-\vec{A}(t)\cdot\vec{r} \tag{1.12a}$$

$$\nabla \wp(\vec{r},t) = -\vec{A}(t) \tag{1.12b}$$

$$\begin{aligned}\frac{\partial \wp(\vec{r},t)}{\partial t} &= \frac{\partial}{\partial t}\left(-\vec{A}(t)\cdot\vec{r}\right) = -\left\{\vec{r}\cdot\frac{\partial\vec{A}(t)}{\partial t} + \vec{A}(t)\cdot\underbrace{\frac{\partial\vec{r}}{\partial t}}_{0}\right\} \\ &= -\vec{r}\cdot\frac{\partial\vec{A}(t)}{\partial t} = -\vec{r}\cdot\vec{E}.\end{aligned} \tag{1.12c}$$

On substituting (1.11), (1.12) in (1.5), we have,

$$\begin{aligned}H' &= \frac{1}{2m}\left(\vec{p} + e\left\{\vec{A}(t) - \vec{A}(t)\right\}\right)^2 - e\left[0 - \left\{-\vec{r}\cdot\vec{E}(t)\right\}\right] + V(r) \\ &= \frac{p^2}{2m} + V(r) - e\vec{r}\cdot\vec{E}(t).\end{aligned} \tag{1.13}$$

Incorporating the definition of dipole moment $\left(\vec{d} = e\vec{r}\right)$ in (1.13), we have

$$H' = \frac{p^2}{2m} + V(r) - \vec{d}\cdot\vec{E}(t) \tag{1.14}$$

$$H_o = \frac{p^2}{2m} + V(r) \tag{1.15a}$$

$$H_I = -\vec{d}\cdot\vec{E}(t) \tag{1.15b}$$

$$H' = H_o + H_I, \tag{1.16}$$

where, H_o and H_I represents the unperturbed Hamiltonian and the atom-field interaction Hamiltonian of the system respectively.

1.3 Density matrix formalism for a two-level atomic system

A simple two-level atomic system is given in **Figure 1.1**. The ground and the excited states are given by the column vectors $|b\rangle = \begin{pmatrix}0\\1\end{pmatrix}$ and $|a\rangle = \begin{pmatrix}1\\0\end{pmatrix}$ respectively. The spontaneous decay of the

excited state is given by Γ and ω_{pr} represents the frequency of the incident probe beam. The one-photon detuning is given by $\Delta_{pr} = \omega - \omega_{pr}$, where ω represents the resonant frequency.

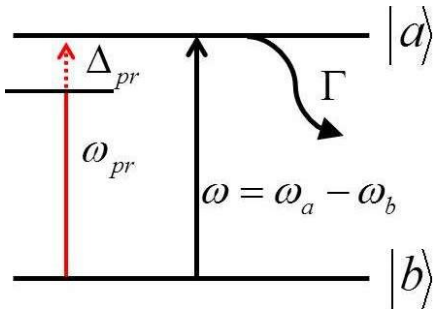

Figure 1.1: A simple two-level atomic system is illustrated, where $|a\rangle$ and $|b\rangle$ represents the excited and ground states respectively.

The wave function $\psi(r,t)$ can be used to describe the atomic system in terms of the probability amplitude $c_a(t)$ and $c_b(t)$ associated with the states $|a\rangle$ and $|b\rangle$ respectively.

$$|\psi(r,t)\rangle = c_a(t)\exp\left[-\frac{iE_a t}{\hbar}\right]\psi_a(\vec{r}) + c_b(t)\exp\left[-\frac{iE_b t}{\hbar}\right]\psi_b(\vec{r}), \quad \textbf{(1.17)}$$

where, the probability of finding the system in the state *i* is given by $|c_i(t)|^2$.

Usually, the Schrodinger equation is used to describe a single particle but if the number of particles increases then the calculations that are involved to describe the evolution of such a system becomes complicated. Moreover, it is not simple to include the decay of the excited state in the wave-function description of the atom-light interaction. Density matrix is a tool that enables the description of an ensemble of atoms and this formalism can be used to study the coherence effects arising due to the atom-field interaction. The density matrix is defined by the projection operator as

$$\rho = |\psi\rangle\langle\psi|. \quad \textbf{(1.18)}$$

Ignoring the time dependence, (1.17) can be re-written as

$$|\psi\rangle = c_a|a\rangle + c_b|b\rangle. \quad \textbf{(1.19)}$$

On substituting (1.19) in (1.18)

$$\rho = \left(c_a |a\rangle + c_b |b\rangle\right)\ \left(c_a^* \langle a| + c_b^* \langle b|\right) \tag{1.20}$$

$$\rho = c_a c_a^* |a\rangle\langle a| + c_a c_b^* |a\rangle\langle b| + c_b c_b^* |b\rangle\langle b| + c_b c_a^* |b\rangle\langle a|$$
$$= c_a c_a^* \begin{pmatrix} 1 \\ 0 \end{pmatrix}(1 \quad 0) + c_a c_b^* \begin{pmatrix} 1 \\ 0 \end{pmatrix}(0 \quad 1) + c_b c_a^* \begin{pmatrix} 0 \\ 1 \end{pmatrix}(1 \quad 0) + c_b c_b^* \begin{pmatrix} 0 \\ 1 \end{pmatrix}(0 \quad 1) \tag{1.21}$$

$$\Rightarrow \rho = \begin{pmatrix} \rho_{aa} & \rho_{ab} \\ \rho_{ba} & \rho_{bb} \end{pmatrix} = \begin{pmatrix} c_a c_a^* & c_a c_b^* \\ c_b c_a^* & c_b c_b^* \end{pmatrix} = \begin{pmatrix} |c_a|^2 & c_a c_b^* \\ c_b c_a^* & |c_b|^2 \end{pmatrix}. \tag{1.22}$$

The diagonal term in the density matrix gives the atomic population and the off-diagonal term represents the atomic coherence associated with the two-level atomic system. To obtain the expression for the atomic susceptibility (χ), the macroscopic polarization $\vec{P}$ is considered which gives the average dipole moment of all the atoms present in the medium and is defined as

$$\vec{P} = N\langle \vec{d} \rangle. \tag{1.23}$$

The dipole moment can be expressed in terms of the density matrix as follows

$$\langle \vec{d} \rangle = Tr\left(\rho \vec{d}\right), \tag{1.24}$$

where, trace of an operator is given by $Tr\left(\hat{O}\right) = \sum_j \langle j | \hat{O} | j \rangle$.

For mixed states, the density matrix is defined as $\rho = \sum_i P_i |\psi_i\rangle\langle\psi_i|$; P_i gives the probability of finding the system in the state $|\psi_i\rangle$ and $\sum_i P_i = 1$ and (1.24) can be written as

$$\langle \vec{d} \rangle = \sum_j \langle j | \rho\, \vec{d} | j \rangle = \sum_i \sum_j P_i \langle j | \psi_i \rangle \langle \psi_i | \vec{d} | j \rangle = \sum_i \sum_j P_i \langle \psi_i | \vec{d} | j \rangle \langle j | \psi_i \rangle. \tag{1.25}$$

Using the completeness relationship $\sum_j |j\rangle\langle j| = \mathrm{I}$ (1.25) reduces as

$$\langle \vec{d} \rangle = \sum_i P_i \langle \Psi_i | \vec{d} | \Psi_i \rangle. \tag{1.26}$$

On substituting (1.26) in (1.23), we have

$$\vec{P} = N\sum_i P_i \left\langle \Psi_i \left| \vec{d} \right| \Psi_i \right\rangle. \tag{1.27}$$

The macroscopic polarization for a two-level atomic system can be written as

$$\vec{P} = N\left\{ \underbrace{\left\langle a \left| \vec{d} \right| a \right\rangle}_{\downarrow 0} + \left\langle a \left| \vec{d} \right| b \right\rangle + \left\langle b \left| \vec{d} \right| a \right\rangle + \underbrace{\left\langle b \left| \vec{d} \right| b \right\rangle}_{\downarrow 0} \right\}. \tag{1.28}$$

The first and the last terms in the RHS of (1.28) is 0 as the dipole moment connects states of opposite parity (parity conservation).

$$\begin{aligned} \vec{P} &= N\left\{ \left\langle a \left| \vec{d} \right| b \right\rangle + \left\langle b \left| \vec{d} \right| a \right\rangle \right\} = Nd_{ba}\left(\rho_{ab} + \rho_{ba}\right) \\ &= Nd_{ba}\left(\tilde{\rho}_{ab}e^{-i\omega t} + \tilde{\rho}_{ba}e^{+i\omega t}\right). \end{aligned} \tag{1.29}$$

The oscillatory terms in the atom interaction Hamiltonian can be removed by making the slow variable transformation i.e., the atom interaction Hamiltonian is transformed into a frame that rotates with the laser frequency (Purves, 2006). The slow variables are defined as,

$$\tilde{\rho}_{ab} = \rho_{ab}e^{+i\omega t}; \tilde{\rho}_{ab}{}^{*} = \rho_{ab},$$
$$\tilde{\rho}_{ba} = \rho_{ba}e^{+i\omega t}.$$

The macroscopic polarization can also be expressed in terms of the electric field vector as

$$\vec{P} = \varepsilon_0 \frac{\vec{E}\chi + \vec{E}^{*}\chi^{*}}{2}. \tag{1.30}$$

Where the electric field vector is given by,

$$\vec{E} = E_{pr}e^{-i\omega_{pr}t}$$

$$\vec{P} = \frac{1}{2}\varepsilon_0 E_{pr}\left(\chi e^{-i\omega_{pr}t} + \chi^{*}e^{+i\omega_{pr}t}\right). \tag{1.31}$$

On comparing (1.29) and (1.31), the final expression for the atomic susceptibility associated with the two-level atomic system is given by

$$\chi = -\frac{2Nd_{ba}^2}{\varepsilon_0 \hbar\Omega}\tilde{\rho}_{ab}. \tag{1.32}$$

The Rabi frequency denoted by Ω appearing in the denominator of (1.32), represents the strength of the atom field interaction and is defined as

$$\Omega = -\frac{\vec{d}\cdot\vec{E}}{\hbar} = -\frac{d_{ba}E_{pr}}{\hbar}. \qquad \textbf{(1.33)}$$

The relation between the Rabi frequency and the intensity of the probe beam is given by

$$\frac{\mathrm{I}}{\mathrm{I}_{sat}} = \frac{2\Omega^2}{\Gamma^2}, \qquad \textbf{(1.34)}$$

where, I_{sat} is the power corresponding to the saturation intensity and it is found to be 1669 $\mu W/cm^2$ for the $\sigma^{\pm 1}$ polarized Rb^{87} atoms locked to $F_g=2 \rightarrow F_e'=3$ transition (Steck, 2010).

In this section, the expression for the atomic susceptibility (χ) has been obtained in terms of the atomic coherence $(\tilde{\rho}_{ab})$ using the density matrix formalism (1.32). The corresponding absorption and the dispersion profiles are given by the imaginary and real part of susceptibility respectively.

1.4 Optical field induced coherences

To describe the optical field induced coherences, the density matrix is expanded in terms of the irreducible tensor (T_q^k) and light induced multipole moments (ρ_q^k) as (Ducloy *et al.*, 1973; Omont, 1977; Budker *et al.*, 2002, 2004)

$$\rho_{\mu F_e m_e;\beta F_g m_g} = \sum_{\mu\beta F_e F_g, kq} \rho_q^k\left(\mu F_e, \beta F_g\right)\, T_q^k\left(\mu F_e, \beta F_g\right), \qquad \textbf{(1.35)}$$

where, μ & β are the labels to specify the state, F_e & F_g represents the hyperfine quantum number of the excited and the ground states respectively and m_e & m_g denotes the magnetic Zeeman sublevels of the excited and the ground states respectively. T_q^k is the irreducible tensor of order k and component $q\,(q=-k,\ .....,\ +k)$ such that $q = m_e - m_g = \Delta m$ (Ducloy *et al.*, 1973).

The multipole moment ρ_0^0 ($q = \Delta m = 0$) corresponds to the population term, ρ_1^1 represents the magnetic dipole moment and ρ_2^2 denotes the electric quadrupole moment. In general, $q = \Delta m \neq 0$ represents the atomic coherence (Ducloy *et al.*, 1973; Omont, 1977; Budker *et al.*, 2002).

Odd orders of ρ describes optical coherences ($F_e \neq F_g$) and even orders with $F_e = F_g$ describe level populations $(\Delta m = 0)$ and Zeeman coherences $(\Delta m \neq 0)$ (Budker *et al.*, 2002). Optical field induced coherences that are created among the ground or excited state Zeeman sublevels are referred to as Zeeman coherences. The coherence that is formed between different hyperfine states $(F_e \neq F_g; k = 0)$ refers to the hyperfine coherence (Omont, 1977; Tremblay and Jacques, 1990; Łobodziński and Gawlik, 1996). The optical, hyperfine and Zeeman coherences that are created during the atom-field interaction has been illustrated for the two level degenerate atomic system ($F_{g1,g2} \rightarrow F_{e1}$) as shown in **Figure 1.2**.

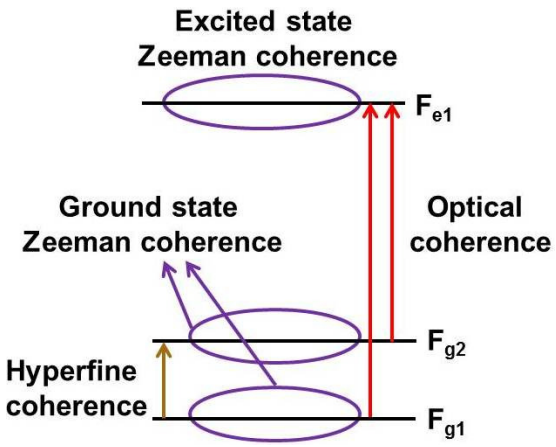

Figure 1.2: Illustration of the optical and Zeeman coherences for the transition $F_{g1,g2} \rightarrow F_{e1}$.

Optical field induced coherences are responsible for phenomena like Hanle electromagnetically induced transparency/absorption (EIT/EIA), non-linear magneto-optical rotation (NMOR) etc. which are discussed in the next section.

1.5 Optical/Zeeman coherence induced phenomenon

1.5.1 Electromagnetically induced transparency (EIT)

EIT is a phenomenon in which the atomic medium is rendered transparent for a resonant probe field in the presence of another pump beam resonant with a common higher/lower energy level (Fleischhauer *et al.*, 2005). The underlying principle behind EIT can be explained in terms of the creation of dark states, that is, the non-coupled state which comprises of the superposition of the ground states.

Different three level schemes such as lambda (Λ), Vee (V) and ladder (cascade) can be used to illustrate the EIT phenomena (Scully and Zubairy, 1997). A typical Λ scheme is shown in **Figure 1.3**.

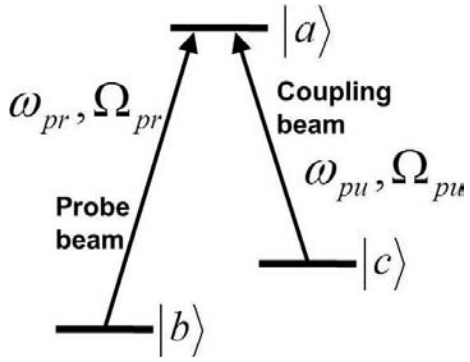

Figure 1.3: The lambda system that can be used to study EIT is shown here.

Ω_{pr} and Ω_{pu} represents the Rabi frequency associated with the probe and the coupling beam. The frequency of the probe and the coupling beam is given by ω_{pr} and ω_{pu} (**Figure 1.3**). **Figure 1.4** illustrates the two excitation pathways namely (i) $|b\rangle \rightarrow |a\rangle$ and (ii) $|b\rangle \rightarrow |a\rangle \rightarrow |c\rangle \rightarrow |a\rangle$ that are involved in the process of EIT (Marangos, 1998). Due to the interaction of the atoms with the optical fields, the bare states $|a\rangle, |b\rangle \& |c\rangle$ no longer form the eigenstates of the interaction Hamiltonian H_I. Therefore the eigenstates of H_I is given by the dressed states which are nothing but the superposition of these bare states.

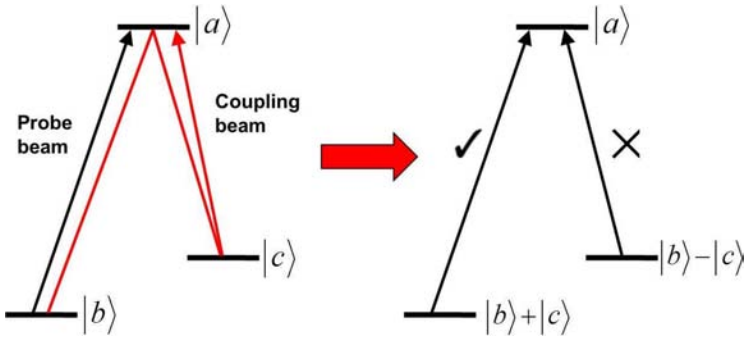

Figure 1.4: Illustration of the excitation pathways and the dressed state picture involved in the EIT process.

The dressed states are given as

$$|C\rangle = \frac{1}{[\Omega_{pr}^2 + \Omega_{pu}^2]^{1/2}}\left(\Omega_{pr}|b\rangle + \Omega_{pu}|c\rangle\right)$$

$$|NC\rangle = \frac{1}{[\Omega_{pr}^2 + \Omega_{pu}^2]^{1/2}}\left(\Omega_{pr}|b\rangle - \Omega_{pu}|c\rangle\right). \quad \textbf{(1.36)}$$

The state $|C\rangle$ called as the coupled state, interacts with both the probe and the coupling beam. On the other hand, $|NC\rangle$ which represents the non-coupled states is completely cut off from the excited state $|a\rangle$. This can be illustrated by considering the transition moment between the states $|NC\rangle$ and $|a\rangle$ which is given by

$$\langle NC|\vec{d}|a\rangle = \frac{\Omega_{pr}}{[\Omega_{pr}^2 + \Omega_{pu}^2]^{1/2}}\langle b|\vec{d}|a\rangle - \frac{\Omega_{pu}}{[\Omega_{pr}^2 + \Omega_{pu}^2]^{1/2}}\langle c|\vec{d}|a\rangle. \quad \textbf{(1.37)}$$

By suitably adjusting the Rabi frequencies Ω_{pr} and Ω_{pu}, the transition moment $\langle NC|\vec{d}|a\rangle$ can be reduced to zero. In other words, destructive interference between the probability amplitude associated with the excitation pathways can be brought about by adjusting the Rabi frequency associated with the probe and the pump beam, thus totally cutting off the dark state from coupling to the higher energy level. This results in the trapping of atoms in the dark state thus making the medium transparent to the probe absorption (Arimondo, 1996; Marangos, 1998; Fleischhauer *et al.*, 2005). The EIT spectrum that is obtained for this lambda system is shown in **Figure 1.5**. The condition for the formation of dark state, $\langle NC|\vec{d}|a\rangle = 0$ is satisfied in **Figure 1.5 (b)** giving rise to EIT.

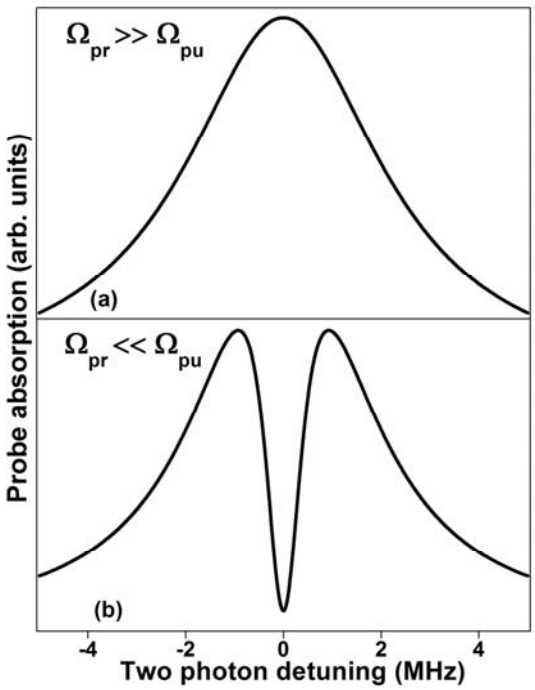

Figure 1.5: The absorption profile as a function of probe detuning for (a) $\Omega_{pr} >> \Omega_{pu}$ and (b) $\Omega_{pr} << \Omega_{pu}$.

1.5.2 Electromagnetically induced absorption (EIA)

EIA is an opposite effect in which there is an enhancement in the probe absorption under the action of a pump beam due to the transfer of coherence (TOC) between the excited and ground states via spontaneous emission in a two-level degenerate system (Akulshin *et al.*, 1998; Lezama *et al.*, 1999; Taichenachev *et al.*, 1999). For the observation of EIA, the ground state must be degenerate to allow for the formation of long lived Zeeman coherences (Lezama *et al.*, 1999; Taichenachev *et al.*, 1999).

There are two ways to obtain EIA in a two-level degenerate system (Goren *et al.*, 2003)

(a) Transfer of coherence (TOC); the polarization of the probe and the pump beam must be different.

(b) Transfer of population (TOP); the polarization of the probe and the pump beam must be same. In this case EIA resonances are formed due to the collisional transfer of population from the ground state to reservoir (other decay channel)

N-type interaction scheme [(**Figure 1.6(a)**] is the simplest atomic system that can be used to demonstrate the EIA process (Taichenachev *et al.*, 1999). A typical EIA profile is shown in **Figure 1.6(b)**.

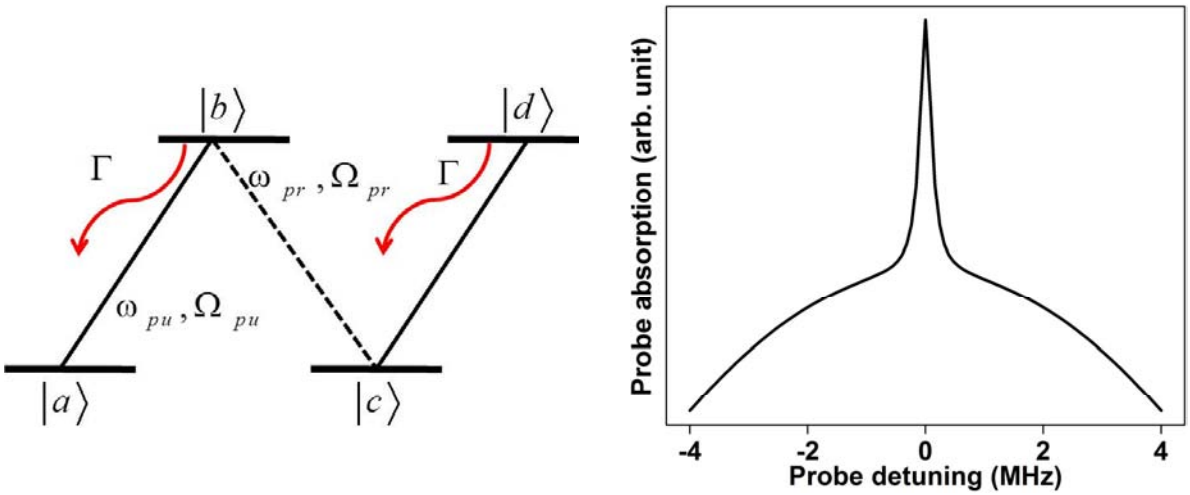

(a) (b)

Figure 1.6: (a) N-type interaction scheme (b) The probe absorption profile as a function of probe detuning to illustrate the EIA process.

1.5.3 Hanle effect

EIT and EIA in a degenerate two level systems can be observed by measuring the transmission or fluorescence of a resonant optical field as a function of a magnetic field scanned through zero. This is referred to as the Hanle configuration (Dancheva *et al.*, 2000). When the magnetic field is scanned along the direction of propagation it is known as the Faraday geometry [**Figure 1.7 (a)**]. In the case of the Voigt geometry, the magnetic field is scanned perpendicular to the direction of propagation [**Figure 1.7 (b)**].

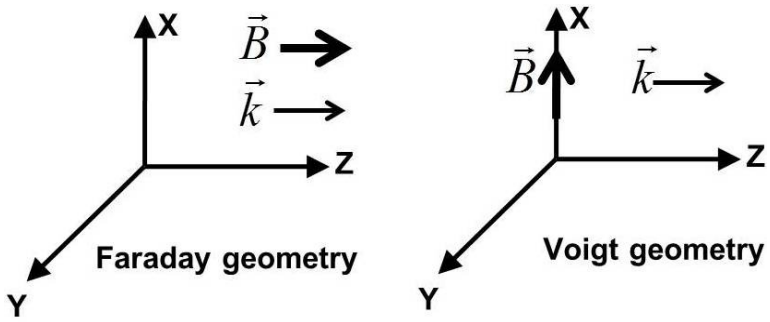

(a) (b)

Figure 1.7: Illustrates (a) Faraday geometry (b) Voigt geometry.

Consider the two level atomic system shown in **Figure 1.8**. The optical field is said to be σ polarized when its electric field vector is directed perpendicular to the quantization axis satisfying the selection rule $\Delta m_f = \pm 1$ (**Figure 1.8**). When the electric field vector is along the direction of the quantization axis, then the optical field is said to be π polarized satisfying the selection rule $\Delta m_f = 0$.

Zeeman coherences will be created among the ground state sublevels when the following condition is satisfied (Harper, 1972)

$$\omega_{g_{-1}g_{+1}} \leq \gamma, \tag{1.38}$$

where, γ represents the decoherence rate and $\omega_{g_{-1}g_{+1}}$ is the frequency difference between the Zeeman sublevels g_{-1} & g_{+1}.

The condition given by (1.38) will be satisfied only when $\omega_{g_{-1}g_{+1}} \approx 0$, i.e. at zero magnetic field. The application of the magnetic field shifts the Zeeman sublevels resulting in the destruction of the Zeeman coherences (**Figure 1.8**). The shift in the Zeeman sublevels is given by the Larmor frequency, ω_L which is related to the magnetic field by the expression

$$\omega_L = \frac{g \mu_B B}{\hbar}, \tag{1.39}$$

where, B is the magnetic field, μ_B is the Bohr magneton ($= h \times 1.399$MHz/Gauss) and g the gyromagnetic ratio.

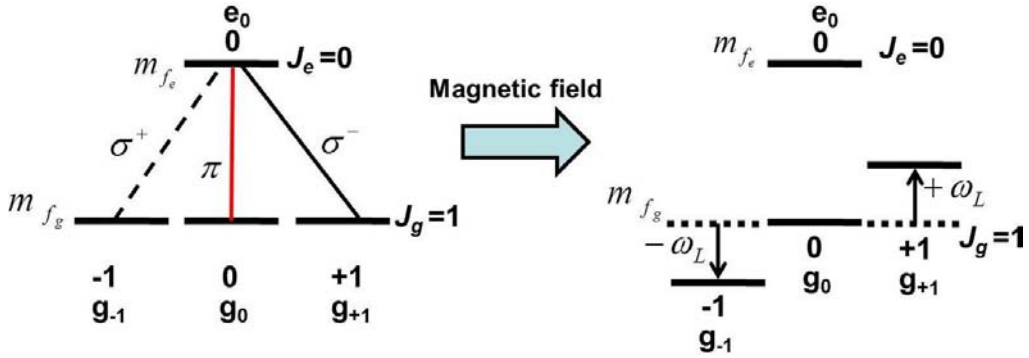

Figure 1.8: The creation and destruction of the ground state Zeeman coherence in the two-level atomic system $J_g = 1 \rightarrow J_e = 0$.

The narrow Hanle EIT/EIA profile arises as a result of the destruction of ground or excited state Zeeman coherence by a magnetic field (Harper, 1972; Renzoni *et al.*, 2001). This explanation is valid only when the quantization axis is chosen along the direction of the magnetic field. When the quantization axis is chosen perpendicular to the direction of the magnetic field, then the Hanle resonances can be explained in terms of the transfer of population (Renzoni *et al.,* 2001). The Hanle EIT and EIA profile is shown in **Figure 1.9 (a)** & **(b)** respectively.

The interaction of the two level atomic system $J_g = 2 \rightarrow J_e = 1$ with the π polarized beam results in the accumulation of the atoms in the magnetic sublevels g_{-2} and g_{+2} due to spontaneous emission **[Figure 1.9 (a)]**. There will be transfer of population among the ground state sublevels on the application of the magnetic field perpendicular to the direction of light polarization. The redistribution of the atoms enhances the population of the absorbing ground state magnetic sublevels. This results in a narrow dip in the probe absorption profile when the magnetic field is scanned through zero- known as the Hanle EIT resonance **[Figure 1.9 (a)]**.

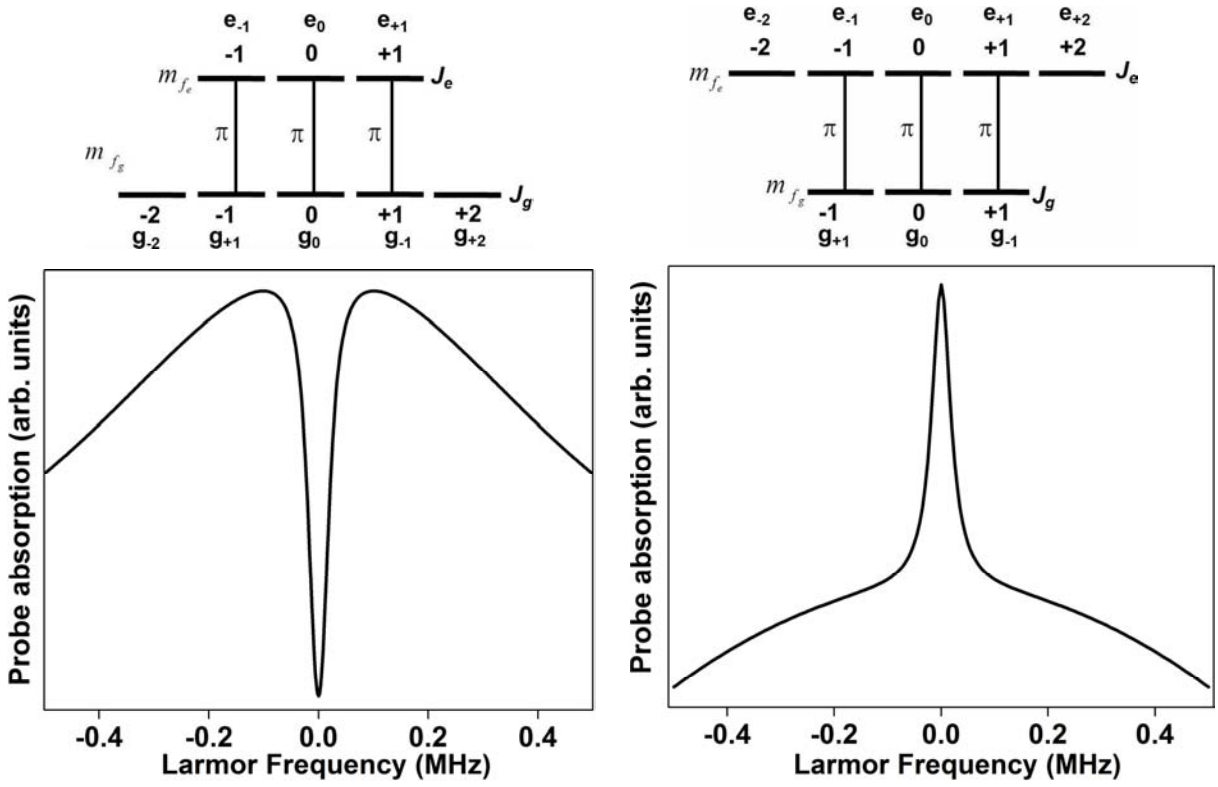

(a) (b)

Figure 1.9: (a) Hanle EIT that has been observed for the transition $J_g = 2 \rightarrow J_e = 1$ (b) Hanle EIA that has been observed for the transition $J_g = 1 \rightarrow J_e = 2$.

For the two level atomic system $J_g = 1 \rightarrow J_e = 2$, the presence of the π polarized beam renders the magnetic sublevel g_0 as the most absorbing state **[Figure 1.9 (b)]**. Application of the external magnetic field redistributes the atoms thus resulting in a decrease in the absorption. Therefore an enhanced absorption peak can be observed at zero magnetic field as shown in **Figure 1.9 (b).** This is known as the Hanle EIA resonance (Alnis and Auzinsh, 2001).

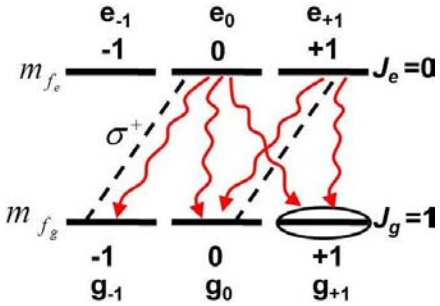

Figure 1.10: Illustrates the formation of oriented state for the transition $J_g = 1 \rightarrow J_e = 1$ due to optical pumping.

Atomic polarization refers to the polarization of the atoms due to optical pumping and they are found to precess at a Larmor frequency ω_L in the presence of the magnetic field. To illustrate atomic polarization, consider the two level atomic system $J_g = 1 \rightarrow J_e = 1$ given in **Figure 1.10.** If the optical field with σ^+ polarization (satisfying the selection rule $\Delta m_f = +1$) interacts with the two level atomic system, optical pumping assembles the atoms in the non-absorbing sublevel $m_f = +1$ as it is not coupled to the excited states. The resulting atomic ensemble is said to be an oriented state (Rochester and Budker, 2000).

1.5.4 Nonlinear magneto-optical rotation (NMOR)

As discussed in the previous section, the magnetic Zeeman sublevels $\left(m_f = \pm 1\right)$ are shifted by $\pm \hbar \omega_L$ on the application of the magnetic field (**Figure 1.8**). Therefore the refractive index associated with the left $\left(\sigma^+\right)$ and the right $\left(\sigma^-\right)$ circularly polarized light will be different resulting in magneto-optical activity known as the Faraday effect [**Figure 1.11(a)**]. This effect was first discovered in 1846 (Faraday, 1855). Macaluso and Corbino (1898) had discovered that the magneto-optical activity associated with the alkali atoms exhibited resonant character near the resonant absorption line. This is known as the resonant magneto-optical rotation.

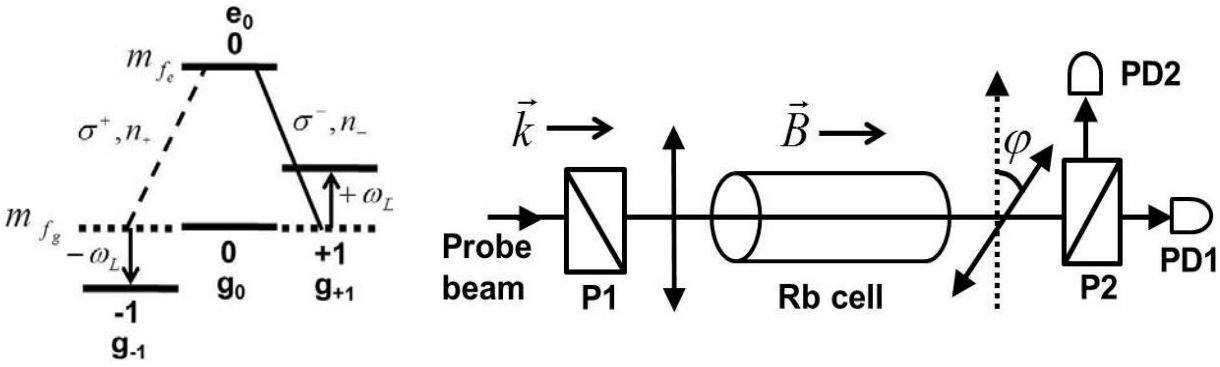

(a) (b)

Figure 1.11: (a) Shows the shifting of the Zeeman sublevels on the application of magnetic field (b) Illustrates the schematic of the Faraday effect.

The expression for the probe beam placed between a polarizer (P1) and an analyzer (P2) [**Figure 1.11(b)**] known as the forward scattered signal (the resonant light is scattered in the direction of the incident field) is given by (Gawlik, 1994; Budker *et al.*, 2002),

$$I_{FS}^{F} = \frac{1}{4}\int \underbrace{\Upsilon(\omega)\left(e^{-\alpha_+ \omega l/c} - e^{-\alpha_- \omega l/c}\right)^2 d\omega}_{\text{I}} + \int \underbrace{\Upsilon(\omega)\, 4e^{-\omega l/c(\alpha_+ + \alpha_-)} \sin^2 \frac{\omega}{c} l\left(n_+ - n_-\right) d\omega}_{\text{II}},$$

(1.40)

where, α_+ and α_- represents the absorption of the left and the right circularly polarized beam respectively, n_+ and n_- is the refractive indices associated with left and right circularly polarized beam and l is the length of the atomic cell. $\Upsilon(\omega)$ gives the spectral density of the incident light. The overall contributions to the I_{FS}^{F} signal due to the terms I and II are comparable. Atomic absorption and dispersion are given by terms I and II of (1.40). Anisotropy in the absorption and the dispersion exhibited by the probe beam of opposite circular polarization gives rise to the circular dichroism and the circular birefringence effect. While the dispersion anisotropy (n_+ and n_-) is proportional to the rotation of the plane of polarization of the incident probe beam, the absorption anisotropy is proportional to ellipticity (Gawlik, 1994; Budker *et al.*, 2002). The two contributions to the I_{FS}^{F} signal have different frequency dependencies. The dichroic effect (first term) is anitsymmetric with respect to laser detuning. Therefore tuning the laser to the center of the resonance reduces the first integral to zero, eliminating the dichroic effect.

In a two level atomic system, the Faraday effect is given by the resonant rotation (by an angle φ) of the plane of polarization of the incident beam in the presence of a longitudinal magnetic field due to a difference in the refractive indices (n_+ and n_-) associated with left and right (σ^+ and σ^-) circularly polarized beams respectively (Chen *et al.*, 1987; Gawlik, 1994; Patnaik and Agarwal, 2000), given by

$$\varphi = \frac{\pi l}{\lambda}\left(n_+ - n_-\right). \tag{1.41}$$

In the nonlinear regime, the macroscopic polarization discussed in **Section 1.3**, can be expanded in terms of susceptibility and electric field as (Chen *et al.*, 1987; Chen *et al.*, 1990; Holmes and Griffith, 1995; Budker *et al.*, 2002)

$$\vec{P} = \sum_{n=1}^{\infty} \chi^{(n)} \vec{E}^{(n)}. \tag{1.42}$$

While, first order susceptibility term $\chi^{(1)}$ is used to describe the linear Faraday effect, the nonlinear magneto-optical effects, where the interaction of light with the atomic medium results in the modification of its optical properties can be attributed to the $\chi^{(3)}$ process (Chen *et al.*, 1990; Holmes and Griffith, 1995; Budker *et al.*, 2002). Holmes and Griffith (1995) evaluated $\chi^{(3)}$ using the third order perturbation theory and shown that $\Delta m = \pm 2$ Zeeman coherence is responsible for NMOR. NMOR has been studied in level schemes such as Λ, V or X (Chen *et al.*, 1990; Ståhlberg *et al.*, 1990).

To carry out the NMOR measurements balanced polarimetry arrangement is used. The signals incident on both the photo diodes (PDs) is balanced off-resonance either by orienting the analyzer P2 at an angle of with respect to the polarizer P1 [**Figure 1.11 (b)**] or by means of a half wave plate (HWP) (**Figure 3.1**), placed right after the cell (Budker *et al.*, 2002). This kind of arrangement ensures that the measured differential signal does not depend upon the induced ellipticity. Therefore the rotation of the plane of polarization (φ) of the probe beam due to its interaction with the resonant medium is obtained by measuring the differential signal between the two PDs. The expression for φ is given by (Huard, 1997)

$$\varphi = \frac{I_1 - I_2}{2(I_1 + I_2)}, \tag{1.43}$$

where, I_1 and I_2 represents the light intensities incident on both the photodiodes.

1.6 Experimental details

1.6.1 Rubidium (Rb) atoms

Rb atoms has an atomic number Z=37 with the electronic configuration of [Kr] $5S^1$. It has a vapor pressure of the order of 10^{-7} Torr at a temperature of 20° C (Steck 2010). The energy level diagram of these atoms is shown in **Figure 1.12**. The splitting of the spectral lines due to the spin-orbit coupling gives rise to the fine structure as shown in **Figure 1.12**.

The two lines - D1 (transition $5S_{1/2} \rightarrow 5P_{1/2}$) and D2 line (transition $5S_{1/2} \rightarrow 5P_{3/2}$) resonates at a wavelength of 795 nm and 780 nm respectively. The hyperfine structure arises due to the interaction of the total angular momentum associated with an unpaired electron ($J = L + S$) with the nuclear spin (I) of the atoms, i.e. $F = J + I$ where denotes the hyperfine / total angular momentum quantum number.

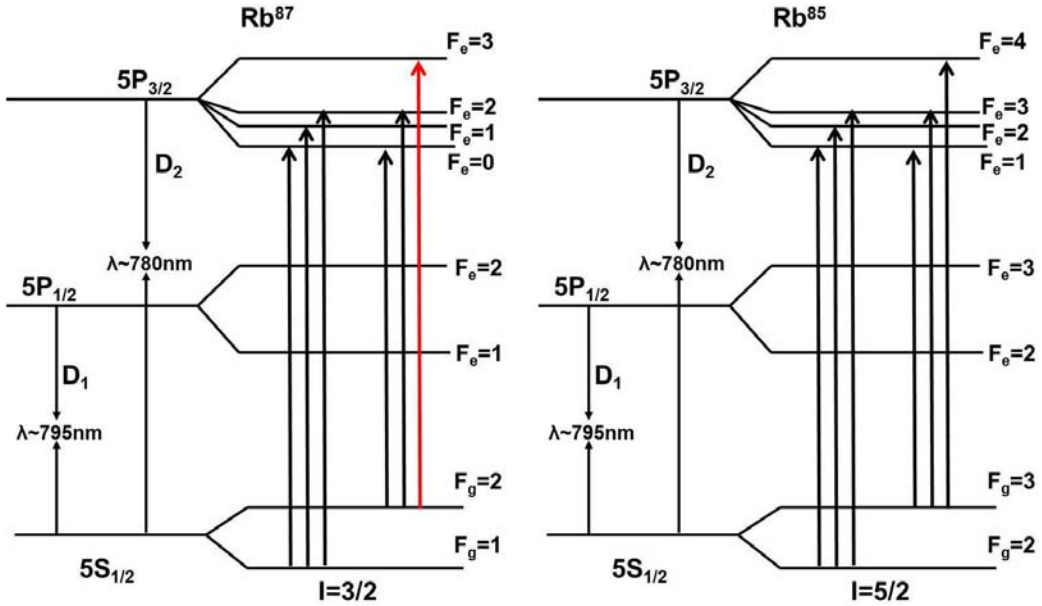

(a) (b)

Figure 1.12: Energy level diagram for (a) Rb^{87} and (b) Rb^{85}. The transition that has been studied experimentally is highlighted by red line.

Rb^{87} (~28%) and Rb^{85} (~72%) are the two naturally occurring isotopes of the Rb atoms with the nuclear spin of $I = 3/2$ & $5/2$ respectively. Each of the hyperfine level will have $2F+1$ magnetic Zeeman sublevels. The application of the magnetic field removes the degeneracy among these Zeeman sublevels. The allowed transition among the hyperfine and the magnetic Zeeman sublevels follow the selection rule $\Delta F = 0, \pm 1$ and $\Delta m = 0, \pm 1$ respectively. For all the field scan experiments, the ECDL has been locked to $Rb^{87}(F_g=2 \rightarrow F_e'=3)$ transition, highlighted by red line in **Figure 1.12**.

1.6.2 External cavity diode laser (ECDL)

Two external cavity diode lasers (ECDL); (1) Sacher Lasertechnik TEC 100 (Sacherlasertechnik, 2003) and (2) homebuilt laser unit loaned by Quantum optics lab at Raman Research Institute (RRI), Bangalore, India have been used for experimental purposes. The ECDL operates at a wavelength of 780 nm and the associated schematic is shown in **Figure 1.13**. On applying current through the laser diode, diverging beam with a width of few GHz is generated as a result of which the laser operates in the multimode. Since laser with single mode output is required where the width of the emission is of the order of few MHz, grating stabilized external cavity has been used as a wavelength tuning/selective element (Wieman and Hollberg, 1991; MacAdam *et al.*, 1992). The grating element diffracts the collimated beam at an angle θ which satisfies the following grating equation,

$$d\left(\sin i - \sin\theta\right) = m\lambda, \tag{1.44}$$

where, i is the angle of incidence, d the spacing between the grating lines and m an integer.

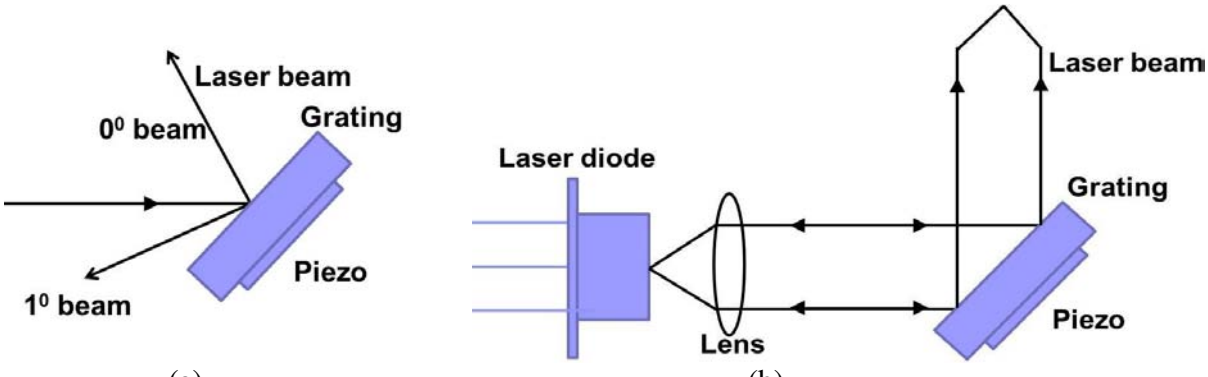

(a) (b)

Figure 1.13: Schematic of (a) Diffracted beams from the grating (b) ECDL

The grating is rotated such that the first order diffracted beam is optically fed back and the zeroth order diffracted beam forms the output of the laser diode. Maximum coupling between the first order and zeroth order diffracted beams amplifies the selective frequency that has been fed back into the laser diode causing the lasing action. Piezo element is used for finer adjustment.

1.6.3 Saturation absorption spectroscopy

A laser beam passing through Rb vapor cell gives rise to Doppler broadened profile which obeys the Maxwell-Boltzmann velocity distribution (**Figure 1.14**). Saturation absorption spectroscopy (SAS) is a technique that is used to eliminate strong Doppler background in-order to clearly resolve all the hyperfine peaks of the Rb atoms (Hänsch *et al.*, 1971; Schawlow, 1982). The experimental set up is shown in **Figure 1.15**.

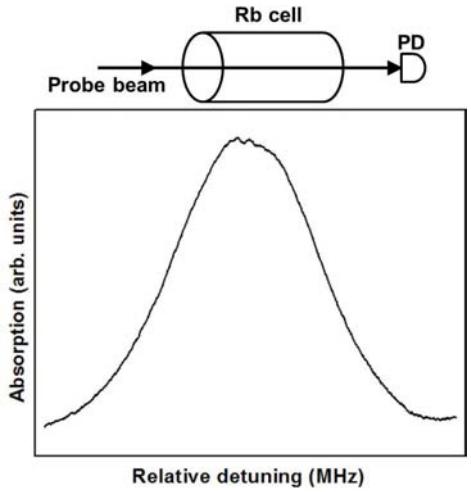

Figure 1.14: Photo-diode response of a laser beam passing through Rb vapor cell.

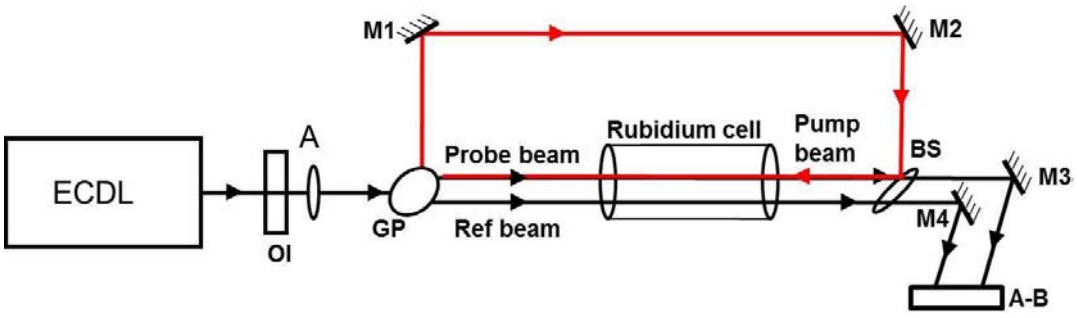

Figure 1.15: Experimental set-up used for saturation absorption spectroscopy, where ECDL: External Cavity Diode Laser, OI: Optical Isolator, A: Aperture, GP: Glass Plate M: Mirror, BS: Beam Splitter, A-B: Photodiode differential amplifier circuit.

As shown in **Figure 1.15**, a weak probe beam and a strong pump beam are maximally overlapped and counter-propagated through the Rb vapor cell. The pump beam is beam dumped and only the probe absorption is studied by photodiode A. The intense pump beam will saturate the atoms to the excited state creating holes in the ground state, resulting in a reduction in the probe absorption. This gives rise to dips known as the 'lamb dips' in a Doppler broadened background. In order to remove the Doppler background, the absorption of a reference beam is recorded by photodiode B (**Figure 1.15**). The A-B photodiode differential amplifier circuit shown in **Figure 1.16,** was constructed with the aid of Atomic and Optical Physics lab at Indian Institute of Science, Bangalore for the photodiode detection of Rb spectra. The differential amplifier circuit subtracts the signal from the two photodiodes giving Doppler free hyperfine Rb peaks (**Figure 1.17**).

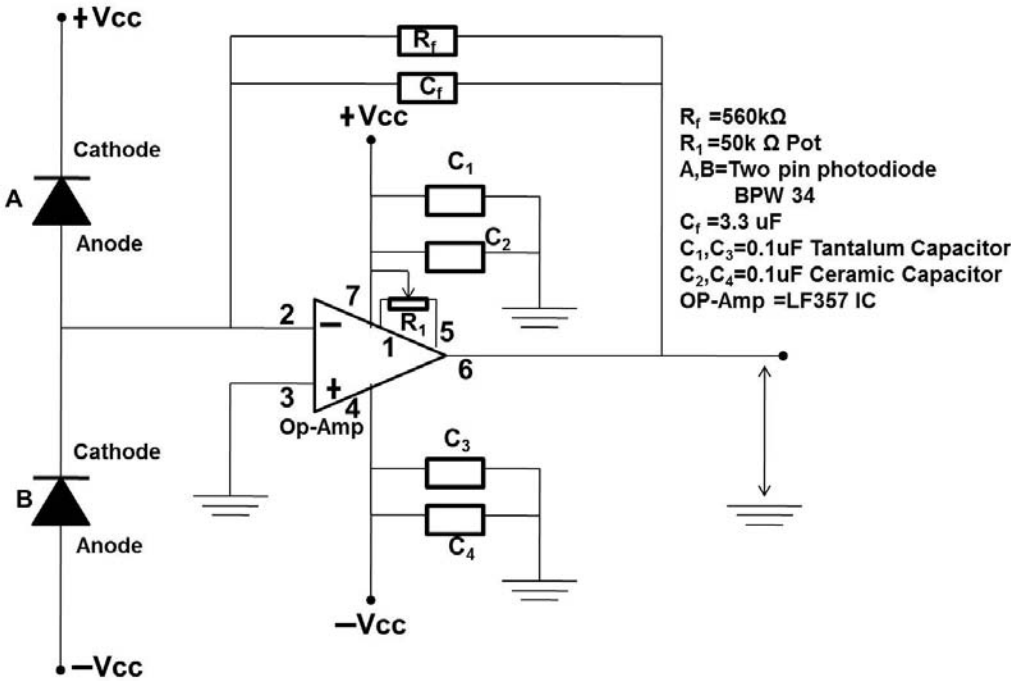

Figure 1.16: Illustrates the schematics of the A-B photodiode differential amplifier circuit

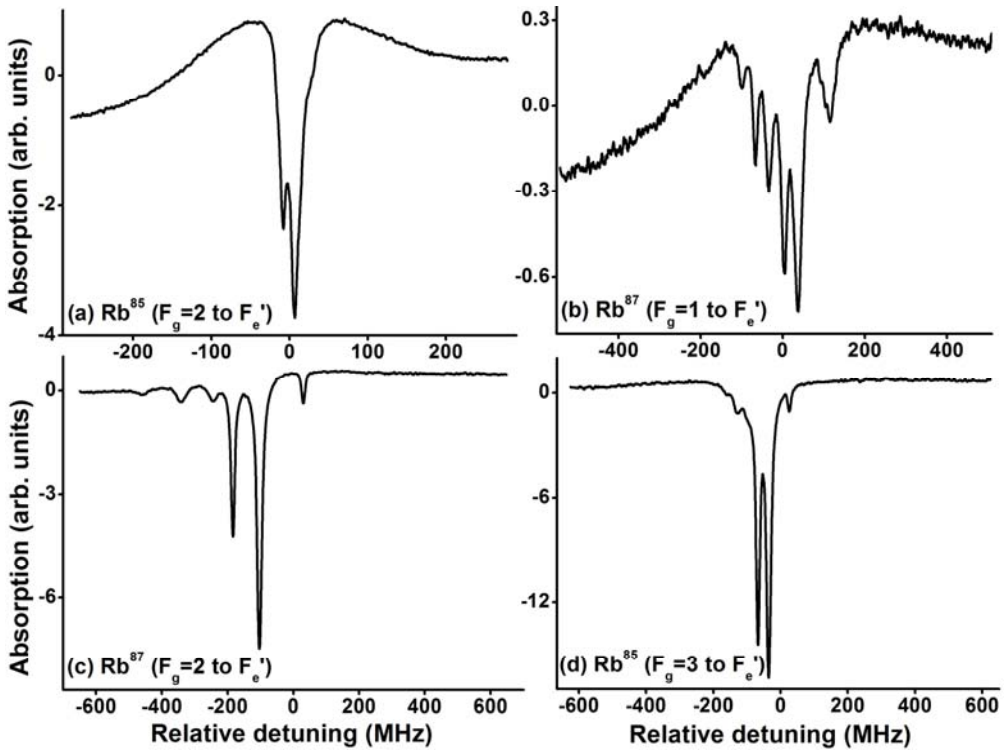

Figure 1.17: The Doppler free saturation absorption peaks for (a) $Rb^{85}(F_g=2\rightarrow F_e')$ (b) $Rb^{87}(F_g=1\rightarrow F_e')$ (c) $Rb^{87}(F_g=2\rightarrow F_e')$ and (d) $Rb^{85}(F_g=3\rightarrow F_e')$.

1.7 Laguerre Gaussian (LG) beam

In general, lasers generate modes known as the transverse modes denoted by TEM_{mn}, where *m* and *n* refers to the number of intensity minima in the direction of the electric field and magnetic field oscillations respectively (Rigrod, 1963). The Gaussian mode (TEM_{00}) is the simplest and desired mode produced by a laser source. The Laguerre Gaussian mode is represented by TEM_{lp}, where *p* denotes the radial mode index and *l* known as the azimuthal mode index represents the number of 2π phase cycles around the mode circumference (Allen *et al.*, 1992; Arlt and Dholakia, 2001). The beam profile of the TEM_{l0} mode is annulus (Rigrod, 1963). To obtain the Gaussian and the LG modes let us consider the wave equation

$$\nabla^2 E - \frac{1}{c^2}\frac{\partial^2 E}{\partial t^2} = 0, \qquad \textbf{(1.45)}$$

where E is the associated field amplitude. The trial solution for the field amplitude is of the form

$$E(x, y, z, t) = \varepsilon(x, y, z)e^{-i\omega t}. \tag{1.46}$$

Incorporating the trial solution in (1.45) we get,

$$\left(\nabla^2 + k^2\right)\varepsilon = 0. \tag{1.47}$$

k is the wave vector and the elliptic partial differential equation given by (1.47) is known as the Helmholtz equation. It is solved in the paraxial approximation (small angle approximation) where it is assumed that there is no component of the field along its axis $\sin\theta \approx \theta;\ \tan\theta \approx \theta\ \ \&\ \ \cos\theta \approx 1$ (Goodman, 1968). The Gaussian and the LG modes can be obtained as a solution to the Helmholtz equation in the Cartesian and cylindrical coordinate systems respectively. The field amplitudes for both the modes is given by (Marcuse, 1982; Allen *et al.*, 1996; Power *et al.*, 1995)

$$\begin{aligned} E_{m,n}^{HG}(x, y, z) &\propto \text{Hermite polynomial} \times \text{Gaussian envelope} \\ E_{l,p}^{LG}(r, \phi, z) &\propto \text{Laguerre polynomial} \times \text{Gaussian envelope} \times e^{il\phi}. \end{aligned} \tag{1.48}$$

The Hermite $\left(H_n(x)\right)$ and the Laguerre polynomial $\left(L_n(x)\right)$ are given by (Weber and Arfken, 2005)

$$\begin{aligned} H_n(x) &= (-1)^n e^{x^2} \frac{d^n}{dx^n} e^{-x^2}, \\ L_n(x) &= \frac{e^x}{n\,!} \frac{d^n}{dx^n}\left(x^n e^{-x}\right). \end{aligned} \tag{1.49}$$

On substituting (1.49) in (1.48) we have,

$$\begin{aligned} E_{m,n}^{HG}(x, y, z) = C_{m,n}^{HG}(x, y, z) \exp\left[-\frac{x^2 + y^2}{w(z)^2}\right] H_m\left(\frac{x\sqrt{2}}{w(z)}\right) H_n\left(\frac{y\sqrt{2}}{w(z)}\right) \\ \times \exp\left[ik\frac{x^2 + y^2}{2R}\right] \exp\left[i(m + n + 1)\tan^{-1}\left(\frac{z}{z_R}\right)\right] e^{ikz} - c.c, \end{aligned} \tag{1.50}$$

where, $C_{m,n}^{HG}(x,y,z)$ is normalizing constant. The Rayleigh length, z_R is defined as

$$z_R = \frac{\pi\, w_o^2}{\lambda}. \tag{1.51}$$

Here $w(z)$ represents the beam waist for a beam width of w_o and is given by (Allen *et al.*, 1996),

$$w(z) = w_o\sqrt{1+\left(z/z_R\right)^2} \approx w_o \text{ for } z << z_R. \tag{1.52}$$

The field amplitude with the LG beam can be given in terms of the field amplitude $\varepsilon_{klp}(\vec{R})$ and phase factor $\Theta_{klp}(\vec{R})$ as follows (Allen *et al.*, 1996; Power *et al.*, 1995),

$$E_{l,p}^{LG}(r,\phi,z) = \varepsilon_{klp}(\vec{R})\exp\left[i\Theta_{klp}(\vec{R})\right] - c.c, \tag{1.53}$$

where, *c.c* denotes the complex conjugate of the first term in the R.H.S of (1.53). The associated mode amplitude and phase factor is defined as (Allen *et al.*, 1996; Power *et al.*, 1995),

$$\begin{aligned}
\varepsilon_{klp}(\vec{R}) &= \frac{\varepsilon_{k00}}{\left(1+\frac{z^2}{z_R^2}\right)^{1/2}} L_p^{|l|}\left(\frac{2r^2}{w(z)^2}\right)\left(\frac{\sqrt{2}r}{w(z)}\right)^{|l|}\exp\left(\frac{r^2}{w(z)^2}\right) \\
\Theta_{klp}(\vec{R}) &= \frac{kr^2 z}{2\left(z^2+{z_R}^2\right)} + (2p+l+1)\tan^{-1}\left(\frac{z}{z_R}\right) + kz + l\phi,
\end{aligned} \tag{1.54}$$

On substituting (1.54) in (1.53), we have

$$\begin{aligned}
E_{l,p}^{LG}(r,\phi,z) = \frac{\varepsilon_{k00}}{\left(1+\frac{z^2}{z_R^2}\right)^{1/2}} L_p^{|l|}\left(\frac{2r^2}{w(z)^2}\right)\left(\frac{\sqrt{2}r}{w(z)}\right)^{|l|}\exp\left(\frac{r^2}{w(z)^2}\right)\exp\left(\frac{ikr^2 z}{2\left(z^2+{z_R}^2\right)}\right) \\
\times\exp\left[i(2p+l+1)\tan^{-1}\left(\frac{z}{z_R}\right)\right]\exp\left[ikz\right]\exp\left[il\phi\right] - c.c.
\end{aligned} \tag{1.55}$$

From (1.55) we can see that the LG beam has a non-vanishing azimuthal phase dependence resulting in a doughnut shaped intensity distribution (Friese *et al.*, 1996).

1.8 Generation of LG beam

The simplest LG beam can be represented as

$$E_1 = E(r, \varphi, z) = E_0 \exp\left[-ik_z z\right] \exp\left[il\phi\right]. \tag{1.56}$$

A plane wave propagating obliquely to the z axis is given by

$$E_2 = \exp\left[-ik_x x - ik_z z\right]. \tag{1.57}$$

The intensities associated with both the beams are,

$$\begin{aligned} I_1 &= E_1 E_1^* = E(r, \phi, z) E(r, \phi, z)^* = {E_0}^2, \\ I_2 &= E_2 {E_2}^* = \left\{e^{-ik_x x - ik_z z}\right\}\left\{e^{-ik_x x - ik_z z}\right\}^* = 1. \end{aligned} \tag{1.58}$$

Sum of the amplitude function is given by

$$I = I_1 + I_2 + 2\,\mathrm{Re}\left(\text{corelation function}\right). \tag{1.59}$$

The correlation function is given by $2\,\mathrm{Re}(I_1 I_2) = 2\,\mathrm{Re}\left\langle E_1 {E_2}^* \right\rangle$. Assuming that the recording device is placed at $z = 0$, we have,

$$I = I_1 + I_2 + 2E_0 \cos\left(l\phi - k_x x\right). \tag{1.60}$$

The Fourier transform of the interference pattern of a plane wave with a LG beam gives the transmittance function denoted by $T\left(r, \phi\right) = \exp\left[i\delta H\left(r, \phi\right)\right]$. Here δ is the amplitude of the phase modulation. $H\left(r, \phi\right)$ is given by (He *et al.*, 1995; Arlt *et al.*, 1998)

$$H\left(r, \phi\right) = \frac{1}{2\pi} \mathrm{mod}\left(l\phi - \frac{2\pi}{\Lambda}\cos\phi, 2\pi\right), \tag{1.61}$$

where, Λ is the fringe spacing and $\mathrm{mod}(a, b) = a - b\,\mathrm{int}(a / b)$

(1.61) was generated for the desired |*l*| value $\left(LG_{p=0}^{l}\right)$ [**Figure 1.18 (a)**] (He *et al.*, 1995; Arlt *et al.*, 1998) and the resulting pattern was printed and a negative (6 mm × 6 mm) was produced with a high resolution black and white photograph. This pattern is known as the computer generated hologram (CGH) given in **Figure 1.18 (a)**. When a Gaussian beam passes through this CGH, it acts as a diffraction grating and LG beams with $l=+1$ and $l=-1$ are produced on either side of the Gaussian beam as shown in **Figure 1.18 (b)**.

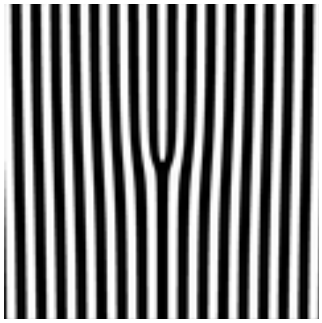

(a)

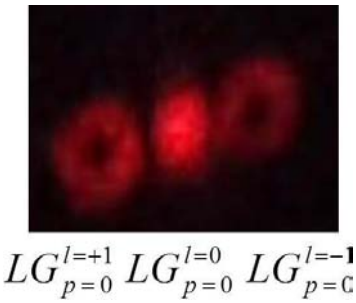

(b)

Figure 1.18: (a) CGH to generate LG beam with |*l*|=1 (b) Picture of the generated LG beam.

CHAPTER 2

Hanle Electromagnetically Induced Transparency and Absorption Resonances with a Laguerre Gaussian beam

2.1 Introduction

In this chapter we computationally and experimentally investigate the influence of LG beam profile on the linewidth of the Hanle EIA/EIT resonances. It is seen that the LG field brings about a significant narrowing in the line shape of the Hanle resonance and ground-state Zeeman coherence in comparison to a Gaussian beam. We have shown that this narrowing arises due to the non-zero azimuthal mode index of the LG field which induces long lived Zeeman coherences.

The influence of the LG beam on the Zeeman coherence was confirmed with two-beam Hanle measurements where the Hanle profile was measured with a Gaussian beam in the presence of the LG beam.

In further support of our conclusions, the Hanle EIA resonance was measured with a ring-shaped beam which is essentially a doughnut shaped beam with zero OAM and we have demonstrated that it is indeed the OAM associated with the LG beam which plays a crucial role in influencing the lifetime of Zeeman coherences.

2.2 Theoretical model

The field amplitude E_{LG} associated with the LG mode is defined in (1.55) of **Section 1.7**. Ignoring the z dependence in (1.55), in the region z << Rayleigh length 'z_R' (Allen *et al.*, 1996), E_{LG} reduces to

$$E_{LG} = E_{LG}^{o}\left(\frac{r}{w_o}\right)^{|l|}\exp\left(-\frac{r^2}{w_o^{\,2}}\right)\exp\left(il\phi\right) - c.c, \qquad \textbf{(2.1)}$$

where, $\exp\left(-il\phi\right)$ is the phase factor and its coefficient represents the reduced mode amplitude of the electric field. The beam width is given by w_o.

To study the effect of the LG field on the Hanle line shape, the transition $J_g = 1 \rightarrow J_e = 0$ (**Figure 2.1**) was chosen, where J_g and J_e represents the total angular momentum quantum number of the ground and excited states respectively. The ground and excited state sublevels for the atomic system are described by g_i and e_i respectively. This system produces a well-known Hanle EIT (Renzoni *et al.*, 1997). We consider a σ-polarized probe beam $\left(\sigma^{+} + \sigma^{-}\right)/2$ which accesses transitions satisfying the selection rule $\Delta m_j = \pm 1$.

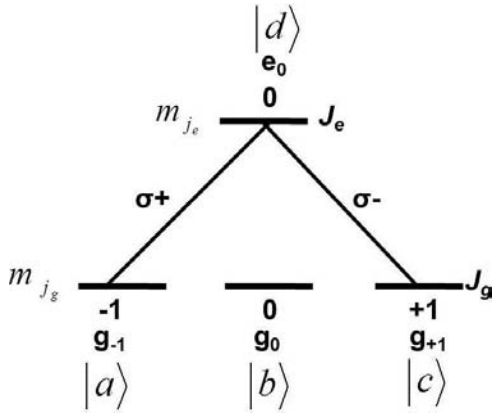

Figure 2.1: Atomic level configuration for the transition $J_g = 1 \rightarrow J_e = 0$.

The ground and excited state sublevels can be expressed in column vectors

$$|a\rangle = \begin{pmatrix}1\\0\\0\\0\end{pmatrix};\quad |b\rangle = \begin{pmatrix}0\\1\\0\\0\end{pmatrix};\quad |c\rangle = \begin{pmatrix}0\\0\\1\\0\end{pmatrix};\quad |d\rangle = \begin{pmatrix}0\\0\\0\\1\end{pmatrix}$$

The total Hamiltonian H of the system is given by the sum of the unperturbed Hamiltonian H_o, the atom-field interaction Hamiltonian H_I and the magnetic interaction energy H_B,

$$H = H_o + H_I + H_B \tag{2.2}$$

$$H_o = \sum_i \hbar\omega_{g_i} |g_i\rangle\langle g_i| + \sum_i \hbar\omega_{e_i} |e_i\rangle\langle e_i| \tag{2.3}$$

$$H_B = \sum_{i\neq 0} \omega_L \left\{ m_{g_i} |g_i\rangle\langle g_i| + m_{e_i} |e_i\rangle\langle e_i| \right\} \tag{2.4}$$

$$H_o = \hbar\begin{pmatrix} \omega_a & 0 & 0 & 0 \\ 0 & \omega_b & 0 & 0 \\ 0 & 0 & \omega_c & 0 \\ 0 & 0 & 0 & \omega_d \end{pmatrix};\quad H_B = \begin{pmatrix} -\omega_L & 0 & 0 & 0 \\ 0 & 0 & 0 & 0 \\ 0 & 0 & +\omega_L & 0 \\ 0 & 0 & 0 & 0 \end{pmatrix}$$

$$H_I = \sum_{\substack{i,j \\ i\neq j}} |i\rangle\langle j| \left\{ \left(d_{ij}E\right)_{\sigma+} + \left(d_{ij}E\right)_{\sigma-} \right\} + h.c, \tag{2.5}$$

where, *h.c* is the Hermitian conjugate of the first term in (2.5). As discussed in **Section 1.5.3**, the expression for the Larmor frequency ω_L is given by (1.39).

The magnetic field direction was chosen perpendicular to both the optical field propagation and polarization directions. The quantization axis was chosen along the direction of magnetic field. The electric field vector associated with the probe beam propagating along the *z*-direction and polarized in the *x*-direction is given by

$$\vec{E} = E_o \cos\left(\omega_{pr} t\right)\, \hat{e}_x, \tag{2.6}$$

where, ω_{pr} is the frequency associated with the incident probe beam. For a Gaussian beam, E_o is taken as a constant and for a LG beam, E_o is replaced by E_{LG} (2.1). According to Wigner-Eckart theorem, the dipole matrix element, d_{ij} can be expressed as the product of the reduced matrix element and the Clebsch-Gordan (CG) coefficient (Bransden and Joachain, 2004)

$$d_{ij} = e \left\langle \alpha_e J_e \right\| r \left\| \alpha_g J_g \right\rangle \left\langle J_e \; m_e ; \; 1 \; q \right| \; J_g - m_g \Big\rangle . \tag{2.7}$$

The CG coefficients is related to the 3-*j* symbol by the following relation

$$\left\langle J_e \; m_e ; \; 1 \; q \right| \; J_g \; m_g \; \Big\rangle = (-1)^{J_e - 1 + m_g} \sqrt{2J_g + 1} \begin{pmatrix} J_e & 1 & J_g \\ m_e & q & -m_g \end{pmatrix} . \tag{2.8}$$

The term in the parenthesis represents the 3-*j* symbol of rank 1. On substituting (2.8) in (2.7), we get,

$$d_{ij} = e \left\langle \alpha_e J_e \right\| r \left\| \alpha_g J_g \right\rangle \; (-1)^{J_e - 1 + m_g} \sqrt{2J_g + 1} \; \left(3j \right)_{eg} , \tag{2.9}$$

where, the 3-*j* symbol can be represented by simpler notation, $\begin{pmatrix} J_e & 1 & J_g \\ m_e & q & -m_g \end{pmatrix} = \left(3j \right)_{eg}$.

The matrix elements, $d_{\pm 1}$ defined as $d_{\pm 1} = e \left\langle e_0 \right| r \left| g_{\pm 1} \right\rangle$ can be expressed as (Sobelman, 1992)

$$\left\langle \alpha \; J \; m \left| d_{+1} \right| \alpha' \; J' \; m' \right\rangle \; \propto \left\langle \alpha_e J_e \right\| d \left\| \alpha_g J_g \right\rangle , \text{ for } \begin{cases} J = J_e , m = 0 \; ; J' = J_g , \; m' = \mp 1 \\ \alpha = \alpha_e ; \alpha' = \alpha_g \end{cases} ,$$

(2.10a)

$$\left\langle \alpha \; J \; m \left| d_{-1} \right| \alpha' \; J' \; m' \right\rangle \; \propto \left\langle \alpha_g J_g \right\| d \left\| \alpha_e J_e \right\rangle , \text{ for } \begin{cases} J = J_g , m = \pm 1 \; ; J' = J_e , \; m' = 0 \\ \alpha = \alpha_g ; \alpha' = \alpha_e \end{cases} .$$

(2.10b)

By invoking the relation between reduced matrix elements with different ordering of states, it can be shown that (Sobelman, 1992)

$$\left\langle \alpha_e J_e \right\| d \left\| \alpha_g J_g \right\rangle \; = (-1)^{J_e - J_g} \left\langle \alpha_g J_g \right\| d \left\| \alpha_e J_e \right\rangle^* .$$

Hence for the atomic system $J_g=1 \rightarrow J_e=0$, $d_{+1}=-d_{-1}$

The Rabi frequencies associated with the Gaussian mode is taken as

$$\Omega_o = \frac{d_{ij}E_o}{\hbar}, \tag{2.11}$$

And the Rabi frequency associated with the LG mode is taken as

$$\Omega_{LG} = \frac{d_{ij}E_{LG}}{\hbar} = \Omega_{LG}^{o}\left(\frac{r}{w_o}\right)^{|l|}\exp\left(-\frac{r^2}{w_o{}^2}\right)\exp\left(-il\phi\right), \tag{2.12}$$

where, $\Omega_{LG}^{o} = \frac{d_{ij}E_{LG}^{o}}{\hbar}$

The atom field interaction Hamiltonian for the atomic system $J_g=1 \rightarrow J_e=0$ is given by

$$H_I = \hbar\left(|d\rangle\langle a| + |a\rangle\langle d| - |d\rangle\langle c| - |c\rangle\langle d| \right) \Omega\cos\omega_{pr}t$$

$$H_I = \frac{\hbar}{2}\begin{pmatrix} 0 & 0 & 0 & \Omega\left(e^{-i\omega_{pr}t}+e^{+i\omega_{pr}t}\right) \\ 0 & 0 & 0 & 0 \\ 0 & 0 & 0 & -\Omega\left(e^{-i\omega_{pr}t}+e^{+i\omega_{pr}t}\right) \\ \Omega\left(e^{-i\omega_{pr}t}+e^{+i\omega_{pr}t}\right) & 0 & -\Omega\left(e^{-i\omega_{pr}t}+e^{+i\omega_{pr}t}\right) & 0 \end{pmatrix}. \tag{2.13}$$

The density matrix ρ is given by

$$\rho = \begin{pmatrix} \rho_{aa} & \rho_{ab} & \rho_{ac} & \rho_{ad} \\ \rho_{ba} & \rho_{bb} & \rho_{bc} & \rho_{bd} \\ \rho_{ca} & \rho_{cb} & \rho_{cc} & \rho_{cd} \\ \rho_{da} & \rho_{db} & \rho_{dc} & \rho_{dd} \end{pmatrix} = \begin{pmatrix} \rho_{g-1g-1} & \rho_{g-1g0} & \rho_{g-1g+1} & \rho_{g-1e0} \\ \rho_{g0g-1} & \rho_{g0g0} & \rho_{g0g+1} & \rho_{g0e0} \\ \rho_{g+1g-1} & \rho_{g+1g0} & \rho_{g+1g+1} & \rho_{g+1e0} \\ \rho_{e0g-1} & \rho_{e0g0} & \rho_{e0g+1} & \rho_{e0e0} \end{pmatrix}.$$

As discussed in **Section 1.3**, the oscillatory terms in the atom interaction Hamiltonian can be removed by making the following slow variable transformations

$$\begin{aligned}
&\tilde{\rho}_{g-1e0} = \rho_{g-1e0} e^{+i\omega_{pr}t}; \tilde{\rho}_{g-1e0}{}^{*} = \tilde{\rho}_{e0g-1};\\
&\tilde{\rho}_{g+1e0} = \rho_{g+1e0} e^{+i\omega_{pr}t}; \tilde{\rho}_{g+1e0}{}^{*} = \tilde{\rho}_{e0g+1};\\
&\tilde{\rho}_{g-1g0} = \rho_{g-1g0} e^{+i\omega_{pr}t}; \tilde{\rho}_{g+1g0} = \rho_{g+1g0} e^{-i\omega_{pr}t}\\
&\tilde{\rho}_{g0e0} = \rho_{g0e0}; \tilde{\rho}_{g-1g+1} = \rho_{g-1g+1};\\
&\tilde{\rho}_{g-1g-1} = \rho_{g-1g-1}; \tilde{\rho}_{g+1g+1} = \rho_{g+1g+1}; \tilde{\rho}_{g0g0} = \rho_{g0g0}; \tilde{\rho}_{e0e0} = \rho_{e0e0}.
\end{aligned} \tag{2.14}$$

Incorporating (2.14) in (2.13),

$$H_I = \frac{\hbar}{2}\begin{pmatrix} 0 & 0 & 0 & \Omega\left(e^{-2i\omega_{pr}t}+1\right) \\ 0 & 0 & 0 & 0 \\ 0 & 0 & 0 & -\Omega\left(e^{-2i\omega_{pr}t}+1\right) \\ \Omega\left(1+e^{+2i\omega_{pr}t}\right) & 0 & -\Omega\left(1+e^{+2i\omega_{pr}t}\right) & 0 \end{pmatrix}. \tag{2.15}$$

The exponential terms, $e^{\pm 2i\omega_{pr}t}$ are basically off-resonant terms rotating with such a large frequency that its effect can be neglected. Hence these rapidly oscillating terms can be removed by invoking the rotating wave approximation (RWA) (Loudon, 1983). The total Hamiltonian of the system after making RWA

$$\tilde{H} = \frac{\hbar}{2}\begin{pmatrix} \omega_a - \omega_L & 0 & 0 & \Omega \\ 0 & \omega_b & 0 & 0 \\ 0 & 0 & \omega_c + \omega_L & -\Omega \\ \Omega & 0 & -\Omega & \omega_d \end{pmatrix}. \tag{2.16}$$

The time evolution of ρ is given by the Liouville equation (Scully and Zubairy, 1997)

$$\frac{d\tilde{\rho}}{dt} = \frac{i}{\hbar}\left[\tilde{\rho}, \tilde{H}\right] - \frac{1}{2}\left\{\tilde{R}, \rho\right\} + \Lambda_\Gamma + \Lambda_\gamma \tag{2.17}$$

The first and the second term on the right hand side of (2.17) represent the commutation and anti-commutation operations respectively. $\tilde{R}$ is the relaxation operator comprising of the relaxation terms Γ and γ. Where, Γ represents the spontaneous decay rate of the excited state and the decoherence rate γ (also known as transit relaxation rate or transit effect) is given by the time the atoms stay in the width of the laser beam (Renzoni and Arimondo, 1998; Patnaik *et al.*, 2007). Λ_Γ and Λ_γ denotes the re-population matrix of the ground state due to the relaxation terms Γ and γ respectively.

$$\tilde{R} = \begin{pmatrix} \gamma & 0 & 0 & 0 \\ 0 & \gamma & 0 & 0 \\ 0 & 0 & \gamma & 0 \\ 0 & 0 & 0 & \gamma+\Gamma \end{pmatrix}. \qquad \textbf{(2.18)}$$

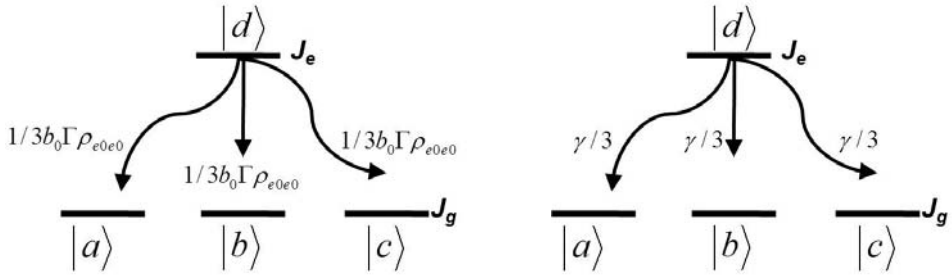

Figure 2.2: Atomic level configuration for the transition $J_g = 1 \rightarrow J_e = 0$, highlighting the re-population of the ground states due to (i) Γ and (ii) γ.

The repopulation matrices are given by

$$\Lambda_\Gamma = \begin{pmatrix} 1/3b_0\Gamma\rho_{e0e0} & 0 & 0 & 0 \\ 0 & 1/3b_0\Gamma\rho_{e0e0} & 0 & 0 \\ 0 & 0 & 1/3b_0\Gamma\rho_{e0e0} & 0 \\ 0 & 0 & 0 & 0 \end{pmatrix}; \Lambda_\gamma = \begin{pmatrix} \gamma/3 & 0 & 0 & 0 \\ 0 & \gamma/3 & 0 & 0 \\ 0 & 0 & \gamma/3 & 0 \\ 0 & 0 & 0 & 0 \end{pmatrix}, \qquad \textbf{(2.19)}$$

where, b_0, the branching ratio component of the transition controls the transfer of population channel.

We obtain 16 coupled first-order differential equations called as the optical Bloch equations (OBE) for the atomic system $J_g=1 \rightarrow J_e=0$ due to the LG beam.

$$\left.\begin{aligned}
\dot{\tilde{\rho}}_{g-1g-1} &= \frac{i\,\Omega_{LG}}{2}\left\{\tilde{\rho}_{e0g-1}-\tilde{\rho}_{g-1e0}\right\}-\gamma\tilde{\rho}_{g-1g-1}+1/3b_0\Gamma\tilde{\rho}_{e0e0}+\gamma/3\\
\dot{\tilde{\rho}}_{g0g0} &= -\gamma\tilde{\rho}_{g0g0}+1/3b_0\Gamma\tilde{\rho}_{e0e0}+\gamma/3\\
\dot{\tilde{\rho}}_{g+1g+1} &= \frac{i\,\Omega_{LG}}{2}\left\{\tilde{\rho}_{g+1e0}-\tilde{\rho}_{e0g+1}\right\}-\gamma\tilde{\rho}_{g+1g+1}+1/3b_0\Gamma\tilde{\rho}_{e0e0}+\gamma/3\\
\dot{\tilde{\rho}}_{e0e0} &= \frac{i\,\Omega_{LG}}{2}\left\{\tilde{\rho}_{g-1e0}+\tilde{\rho}_{e0g+1}-\tilde{\rho}_{g+1e0}-\tilde{\rho}_{e0g-1}\right\}-\left(\gamma+\Gamma\right)\tilde{\rho}_{e0e0}
\end{aligned}\right\} \quad \textbf{(2.20a)}$$

$$\left.\begin{aligned}
\dot{\tilde{\rho}}_{g-1e0} &= i\left\{\left(\omega_L-\Delta_{pr}\right)\tilde{\rho}_{g-1e0}+\frac{\Omega_{LG}}{2}\left(\tilde{\rho}_{e0e0}+\tilde{\rho}_{g-1g+1}-\tilde{\rho}_{g-1g-1}\right)\right\}-\left(\gamma+\frac{\Gamma}{2}\right)\tilde{\rho}_{g-1e0}\\
\dot{\tilde{\rho}}_{g0e0} &= i\left\{1/2\Omega_{LG}\left(\tilde{\rho}_{g0g+1}-\tilde{\rho}_{g0g-1}\right)-\Delta_{pr}\tilde{\rho}_{g0e0}\right\}-\left(\gamma+\Gamma/2\right)\tilde{\rho}_{g0e0}\\
\dot{\tilde{\rho}}_{g+1e0} &= i\left\{\frac{\Omega_{LG}}{2}\left(\tilde{\rho}_{g+1g+1}-\tilde{\rho}_{g+1g-1}-\tilde{\rho}_{e0e0}\right)-\left(\omega_L-\Delta_{pr}\right)\tilde{\rho}_{g+1e0}\right\}-\left(\gamma+\frac{\Gamma}{2}\right)\tilde{\rho}_{g+1e0}
\end{aligned}\right\} \quad \textbf{(2.20b)}$$

$$\left.\begin{aligned}
\dot{\tilde{\rho}}_{g-1g0} &= i\left\{\ \omega_L\tilde{\rho}_{g-1g0}+1/2\Omega_{LG}\tilde{\rho}_{e0g0}\ \right\}-\gamma\tilde{\rho}_{g-1g0}\\
\dot{\tilde{\rho}}_{g0g+1} &= i\left\{\ \omega_L\tilde{\rho}_{g0g+1}+1/2\Omega_{LG}\tilde{\rho}_{g0e0}\ \right\}-\gamma\tilde{\rho}_{g0g+1}\\
\dot{\tilde{\rho}}_{g-1g+1} &= i\left\{\ 2\omega_L\tilde{\rho}_{g-1g+1}+1/2\Omega_{LG}\left(\tilde{\rho}_{g-1e0}+\tilde{\rho}_{e0g+1}\right)\ \right\}-\gamma\tilde{\rho}_{g-1g+1}
\end{aligned}\right\}. \quad \textbf{(2.20c)}$$

(2.20a), (2.20b) and (2.20c) represent OBE for the associated atomic population, optical coherences and Zeeman coherences respectively. These OBE are numerically solved (Rochester (2008); Malakyan *et al.*, 2004) under steady-state conditions by setting the right hand side of (2.20) to zero. The steady state probe absorption, α for the atomic system $J_g=1 \rightarrow J_e=0$ comes out to be (Boyd, 2003)

$$\alpha = \frac{2\sqrt{2}\pi\nu_o N}{\hbar c\Omega}\left|d_{ij}\right|^2\left(\frac{1}{\sqrt{3}}\mathrm{Im}\left[\rho_{e_0g_{-1}}\right]+\frac{1}{\sqrt{3}}\mathrm{Im}\left[\rho_{e_0g_{+1}}\right]\right)$$

$$\alpha = \frac{2\sqrt{2}\pi\nu_o N}{\hbar c\Omega}\left|d_{ij}\right|^2\left\{(3j)_{0-1}\,\mathrm{Im}\left[\rho_{e_0 g_{-1}}\right]+(3j)_{0+1}\,\mathrm{Im}\left[\rho_{e_0 g_{+1}}\right]\right\},$$

where, ν_o is the frequency difference between the ground and the excited states in the absence of the magnetic field and N is the density of atoms.

Since, $(3j)_{eg} = (3j)_{0-1} = (3j)_{0+1} = \frac{1}{\sqrt{3}}$, α can be re-written as

$$\alpha = \frac{2\sqrt{2}\pi\nu_o N}{\hbar c\Omega}\left|d_{ij}\right|^2\left\{(3j)_{0-1}\,\mathrm{Im}\left[\rho_{e_0 g_{-1}}\right]+(3j)_{0+1}\,\mathrm{Im}\left[\rho_{e_0 g_{+1}}\right]\right\},$$

on generalizing the steady-state probe absorption, we have,

$$\alpha = \sum_{\substack{i,j \\ i\neq j}} \frac{2\sqrt{2}\pi\nu_o N}{\hbar c\Omega}\left|d_{ij}\right|^2 (3j)_{eg}\,\mathrm{Im}[\rho_{e_i g_j}]. \qquad \textbf{(2.21)}$$

For a Gaussian beam, (2.21) is used to compute the absorption with the Rabi frequency $\Omega(=\Omega_o)$ treated as a constant.

To compute the probe absorption for the LG beam, Ω in (2.21) is replaced by Ω_{LG} (with Ω_{LG}^o treated as a constant) and a double integration carried out over parameters r and ϕ (ignoring the z dependence as in (2.1)),

$$\alpha = \sum_{\substack{i,j \\ i\neq j}} \frac{2\sqrt{2}\pi\nu_o N}{\hbar c\Omega}\left|d_{ij}\right|^2 (3j)_{eg}\,\mathrm{Im}[\rho_{e_i g_j}]$$

$$\alpha = \int_{r=0}^{w_o}\int_{\phi=0}^{2\pi}\sum_{\substack{i,j \\ i\neq j}} \frac{2\sqrt{2}\pi\nu_o N}{3\hbar c\Omega_{LG}^o\left(\frac{r}{w_o}\right)^{|l|} e^{\left(-\frac{r^2}{w_o{}^2}\right)} e^{il\phi}}\left|d_{ij}\right|^2 (3j)_{eg}\,\mathrm{Im}[\rho_{e_i g_j}]\,r\,dr\,d\varphi. \qquad \textbf{(2.22)}$$

2.3 Computational results

The calculated absorption of the incident optical field as a function of Larmor frequency (the Hanle profile) for Gaussian and LG beams is shown in **Figure 2.3**. The azimuthal mode index associated with the LG beam is taken as $|l| = 1$ with $\Gamma/\gamma = 20, \Omega_o/\Gamma = 1, \Omega_{LG}^o/\Gamma = 1,$ $\Delta_{pr} = 0,\ b_0 = 1$ and $w(z) = w_o = 3$mm.

It can be seen from **Figure 2.3** that the Hanle EIT profile due to the LG beam is significantly narrower than the one that is obtained with the Gaussian beam. The computed Hanle profile linewidths for Gaussian and LG beams are 0.363 MHz and 0.131 MHz respectively. The percentage narrowing observed in linewidth defined as $\left(\frac{L.W_G - L.W_{L.G}}{L.W_G}\%\right)$ was found to be ≈ 64%.

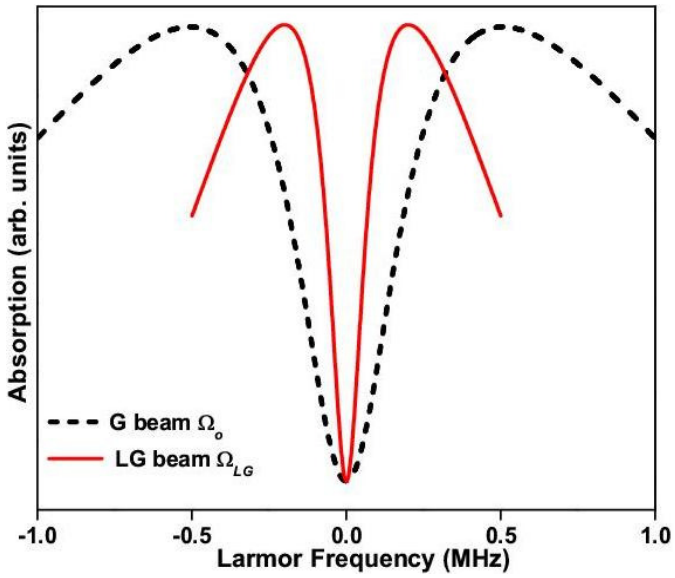

Figure 2.3: Calculated Hanle resonance for $J_g = 1 \rightarrow J_e = 0$ with G and LG field using $\Gamma/\gamma = 20, \Omega_o/\Gamma = 1,\ \Omega_{LG}^o/\Gamma = 1,\ \Delta_{pr} = 0,\ b_0 = 1$ and $w(z) = w_o = 3$mm for $|l| = 1$.

The ground state Zeeman coherence, ρ_{g-1g+1} – responsible for the Hanle EIT resonance (McLeant *et al.,* 1985) – computed by integrating over the parameters r and ϕ also exhibits a similar narrowing as shown in **Figure 2.4**.

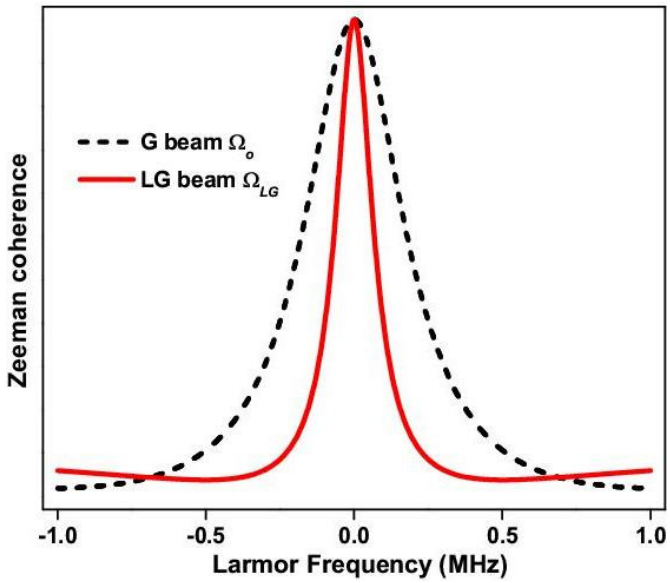

Figure 2.4: Normalized Ground state Zeeman coherence created by Gaussian and LG fields. Parameters are same as those used in **Figure 2.3**. See text for details

The source of the narrowing in the computation originates in the presence of the spatially dependent Rabi frequency (2.12) in the interaction Hamiltonian (2.4) and in the Liouville equation (2.17). To understand the origin of this narrowing, we recomputed the probe absorption and Zeeman coherence with $\Omega_{LG} \approx \Omega_{LG}^{o} e^{-il\varphi}$, ignoring the radial dependence. It is seen from **Figure 2.5(a)** that the narrowing is absent. Alternatively if the phase factor is ignored, with $\Omega_{LG} \approx \Omega_{LG}^{o} \left(r / w_o\right)^{|l|} \exp\left(-r^2 / w_o^{\,2}\right) \exp\left(-il\phi\right)$, the same narrowing is observed in the Hanle profile [**Figure 2.5(b)**] and the Zeeman coherence. This suggests that the azimuthal mode index (l) associated with the LG beam which features in Ω_{LG} brings about the observed narrowing.

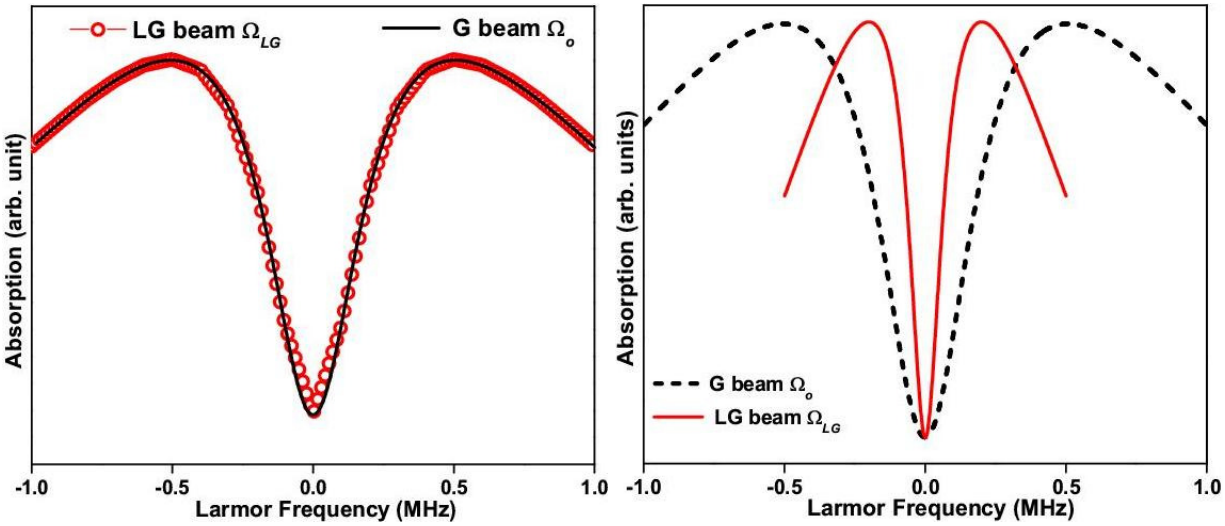

(a) (b)

Figure 2.5: Probe absorption for $J_g = 1 \rightarrow J_e = 0$ due to Gaussian and LG beams. In (a) the radial dependence of Ω_{LG} has been ignored and in (b) the phase factor in Ω_{LG} has been ignored. Other parameters are same as those used in **Figure 2.3**. See text for details.

The Hanle signal linewidth is determined by the relaxation rate of ground or excited state Zeeman coherences (Renzoni *et al.*, 2001). Therefore a narrow Hanle signal suggests that an optical field with non-zero orbital angular momentum ($l\hbar$) promotes long-lived Zeeman coherences.

Further support for this possibility is found when the Hanle profile or transit effect limited resonance with the LG field was computed for different azimuthal mode indices $|l|$= 1, 2 and 3 (**Figure 2.6**). Kotlyar *et al.* (2006) have shown that the LG beam waist increases with increase in l. Hence, values of 3 mm, 4 mm and 5 mm were chosen as the beam waist for the LG field with azimuthal mode index $|l|$=1, 2 and 3 to represent this feature.

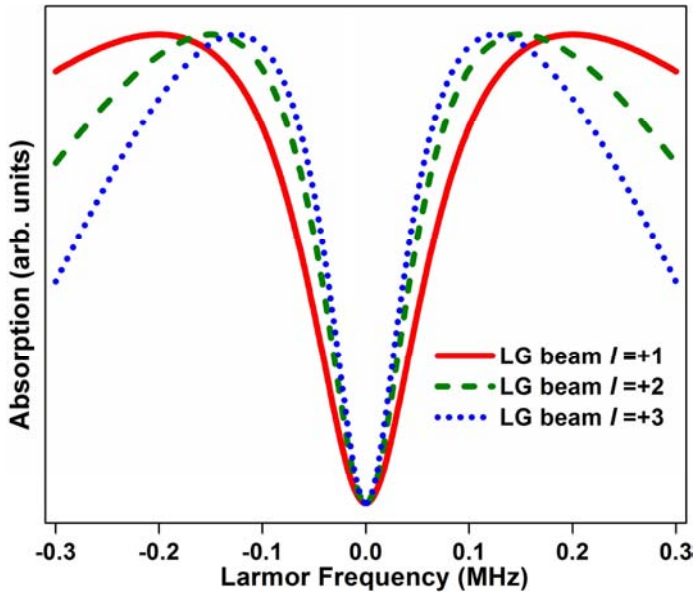

Figure 2.6: Probe absorption with LG field for azimuthal mode indices, $|l|$= 1, 2 and 3 with $w_o = 3$ mm, 4 mm and 5 mm respectively. Plotting style and other parameters are same as those used in **Figure 2.3**.

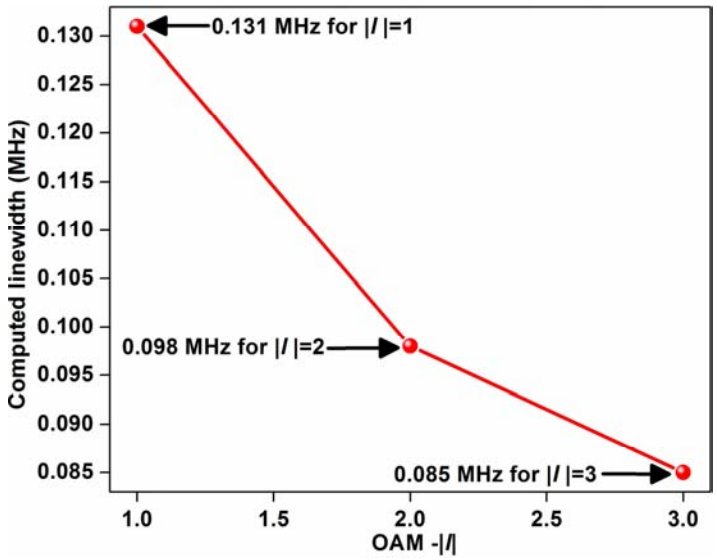

Figure 2.7: Linewidth of the computed Hanle EIT profile for LG field as a function of OAM associated with it.

The EIT width due to LG beam with $|l|$= 1, 2 and 3 is shown in the **Figure 2.7**. The extent of narrowing between the computed linewidths due to $|l|$=2 and 3 is lesser than that for $|l|$=1 and 2 (**Figure 2.7**). A similar observation is made in the measured Hanle EIA profile, which will be discussed in the next section.

2.4 Experimental details and results

An experimental study of the Hanle profile was carried out with Gaussian and LG fields to verify the computational results that have been discussed in the previous section. Hanle measurements were obtained with Rb vapor with an ECDL locked to the $F_g = 2 \rightarrow F_e' = 3$ transition of Rb^{87}. This transition gives rise to an EIA and has been studied by several groups (Dancheva *et al.*, 2000; Renzoni *et al.*, 2001; Dimitrijević *et al.*, 2008). The LG beam was created using a computer generated hologram (CGH) (He *et al.*, 1995; Arlt *et al.*, 1998).

The beam with azimuthal mode index $|l| = 1$ was used as the probe beam. The transmission of the probe beam was measured as a function of magnetic field scanned perpendicular to the direction of the probe beam along the *x*-axis. The probe beam was polarized along the *y*-axis (**Figure 2.8**). Rubidium (Rb) vapor cell with a natural mixture of the Rb isotopes (Rb^{87}~28% and Rb^{85}~ 72%) was placed between a pair of Helmholtz coils to null the fields in the other two directions to ~ 0.3 mG. The magnetic field measurements and the field scan calibrations were carried out by using a flux gate magnetometer. Measurements were also made with a Gaussian beam of the same intensity.

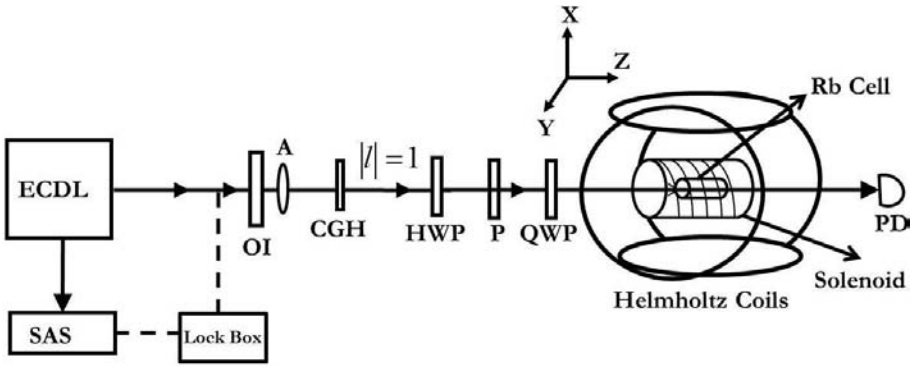

Figure 2.8: Experimental set-up used for measuring the Hanle profile with a LG beam, where ECDL: External Cavity Diode Laser, SAS: Saturation Absorption Spectroscopy set-up, OI: Optical Isolator, A: Aperture, P: Polarizer, CGH: Computer Generated Hologram, PD: Photo Detector, HWP: Half Wave Plate, QWP: quarter wave plate.

The Hanle profile obtained with Gaussian and LG beams is shown in **Figure 2.9**. The LG profile is distinctly narrower than the Gaussian beam profile confirming our computational results. The measured linewidths of the Hanle EIA profile for Gaussian and LG beams are 0.343 Gauss and 0.161 Gauss respectively. The percentage of narrowing observed in this experiment was found to be ≈ 53% (comparable to the computation value of ≈ 64%).

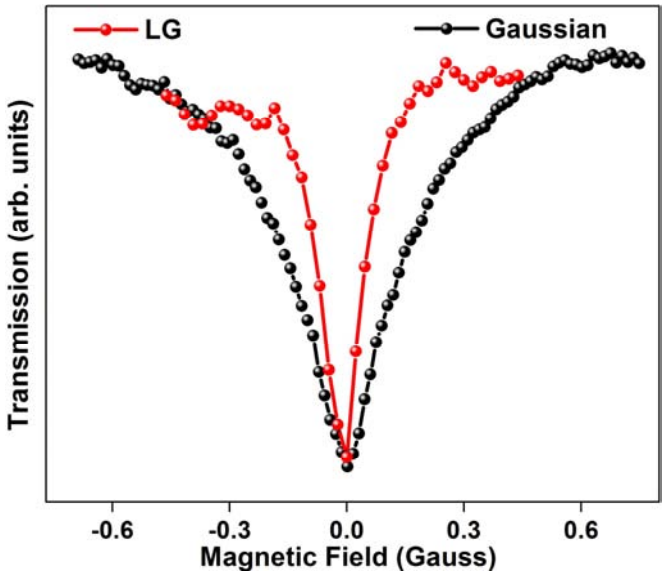

Figure 2.9: Measured Hanle EIA profiles for Gaussian and LG beams locked to the $F_g=2 \rightarrow F_e'=3$ transition of Rb^{87}. Both the beams were maintained at the same intensity.

Hanle profiles obtained for different intensities of Gaussian and LG probe fields are shown in **Figure 2.10**. The combination of a half-wave plate and the polarizer placed right before the cell was used to vary the intensity of the beams from 849μW/cm^2 to 2888μW/cm^2. The linewidth of the measured Hanle EIA profile due to the Gaussian and LG beams as a function of their intensity is shown in **Figure 2.11(a)**.

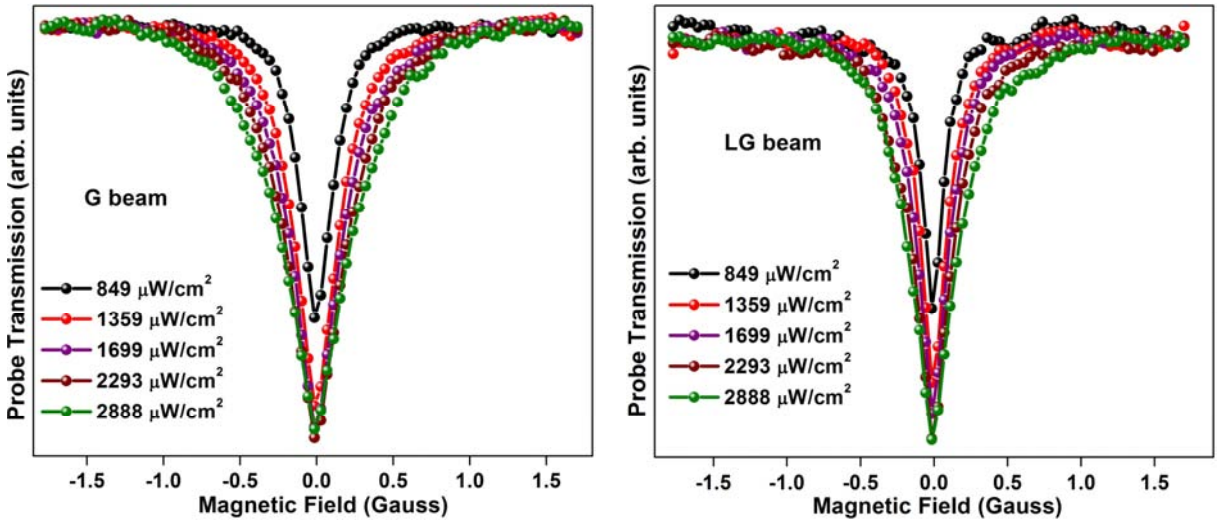

(a) (b)

Figure 2.10: Measured Hanle EIA profiles by locking the laser to the transition $Rb^{87}(F_g=2 \rightarrow F_e'=3)$ for different intensities in the presence of circularly polarized (a) Gaussian and (b) LG beam.

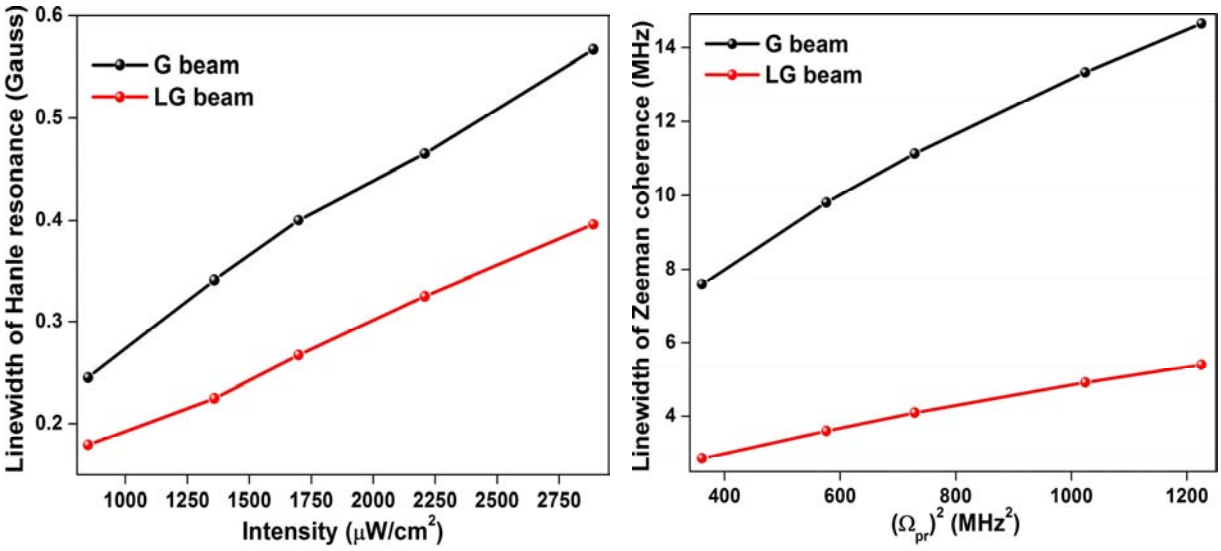

(a) (b)

Figure 2.11: The study of (a) the linewidth of the measured Hanle EIA profile as a function of intensity due to circularly polarized Gaussian and LG beam (b) the linewidth of the computed Zeeman coherence as a function of the square of the Rabi frequency.

It can be seen that the width of the measured Hanle EIA profile due to the LG field is narrower in comparison to a Gaussian beam at all values of intensity, the extent of narrowing induced by the LG field increasing with increase in intensity [**Figure 2.11 (a)**]. A similar behavior is observed when the linewidth of the real part of ground state Zeeman coherences $(\Delta m = \pm 2)$ due to Gaussian and LG beams are plotted as a function of square of the Rabi frequency corresponding to the intensity values that have been used in the experiment [**Figure 2.11 (b)**].

The behavior of the normalized Zeeman coherence and ground state population as a function of the Rabi frequency (**Figure 2.12**) determines the nonlinear response of the atomic medium (Pustelny, 2007). The low Rabi frequency behavior ($\Omega_{pr} \leq 0.02$ MHz) of the normalized Zeeman coherence and ground state population is less nonlinear for LG beam when compared to the Gaussian beam for the atomic system $J_g = 1 \rightarrow J_e = 0$ (shown in the inset in **Figures 2.12(a)** and **(b)** respectively).

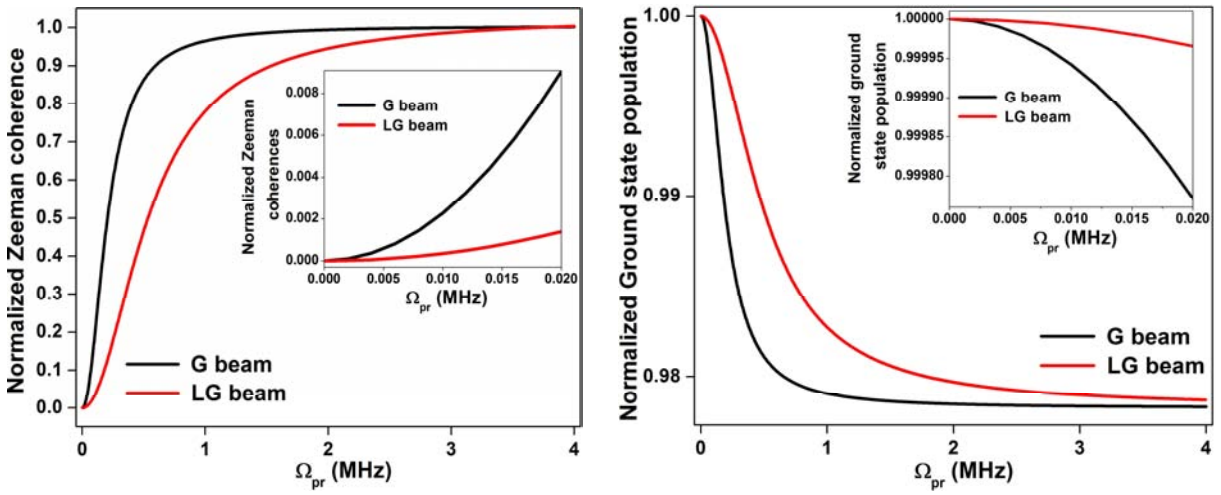

(a) (b)

Figure 2.12: The study of (a) Normalized ground state Zeeman coherence and (b) Normalized ground state population as a function of the probe Rabi frequency due to both Gaussian and LG beams. The plot for very low Rabi frequency is shown in the inset.

To verify the computational result (**Figure 2.7**), the Hanle EIA resonance due to the circularly polarized LG beam with $|l|$ = 1, 2 and 3 was measured [**Figure 2.13 (a)**] and the line width of the measured Hanle EIA profile for LG field was plotted as a function of OAM associated with it as shown in **Figure 2.13 (b)**. The EIA linewidth due to the LG beam is mentioned in the **Figure 2.13(b)**. As observed in the computation, the extent of narrowing between the measured linewidths due to $|l|$=2 and 3 is lesser than that for $|l|$=1 and 2.

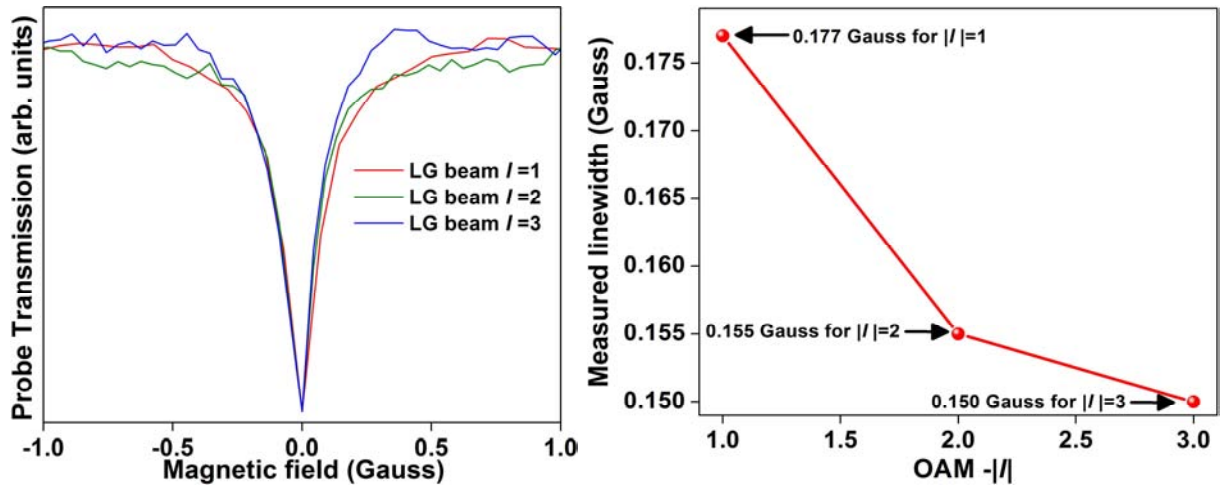

(a) (b)

Figure 2.13: (a) Measured Hanle EIA profile due to LG beam with $|l|$= 1, 2 and 3 (b) Linewidth of the measured Hanle EIA profile for LG field as a function of OAM associated with it.

The influence of the LG beam on the Zeeman coherence was confirmed with a two-beam Hanle measurement. The experimental set-up used is shown in **Figure 2.14**. The Hanle profile was measured with a Gaussian probe beam in the presence of a LG beam ($|l|= 1$). The circularly polarized probe and the coupling beams were co-propagated through the Rb vapor cell. The Gaussian beam was maintained at a fixed intensity of 1132 $\mu W/cm^2$. The LG beam was blocked after it passed through the Rb cell.

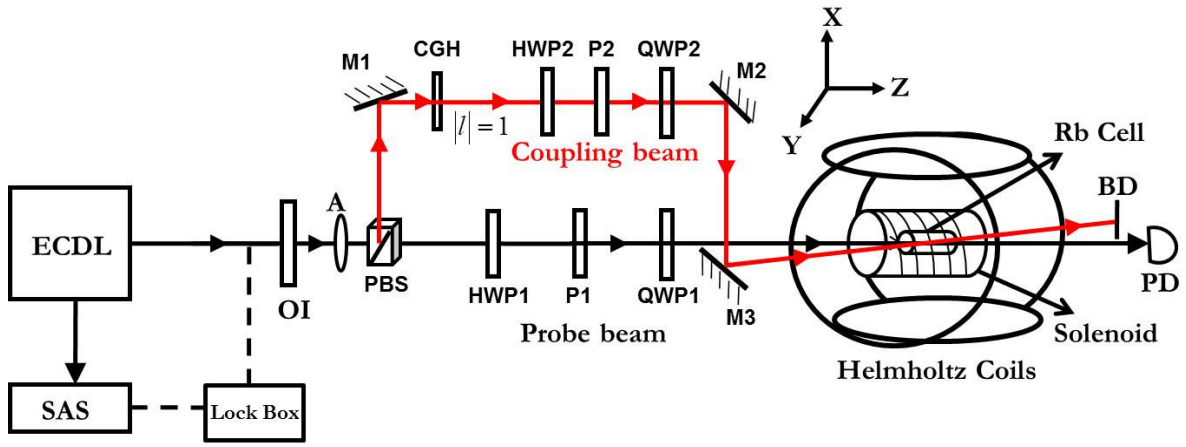

Figure 2.14: Experimental set-up used for the two-beam Hanle measurement. The key is the same as mentioned in **Figure 2.8**.

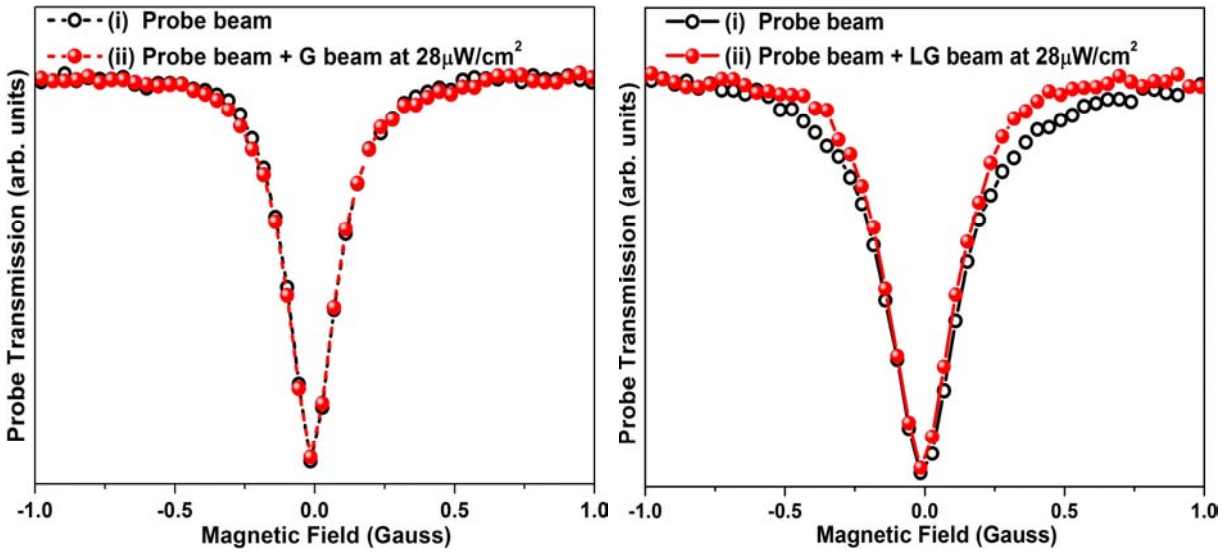

Figure 2.15: Measured Hanle EIA profile for Gaussian beam (1132 $\mu W/cm^2$) locked to the $F_g =2 \rightarrow F_e' =3$ transition of Rb^{87} with and without a coupling beam. The coupling beam is (a) Gaussian and (b) Laguerre Gaussian. Introduction of the LG beam lowers the linewidth of the Gaussian EIA Hanle profile from 0.313 Gauss to 0.262 Gauss.

From **Figure 2.15(b)**, it can be seen that the LG beam, (intensity of ~28 μW/cm^2), induces a noticeable narrowing of about 51 mG in the linewidth of the Hanle profile of the probe beam. No narrowing was observed when the LG beam is replaced with a Gaussian beam (l =0) [**Figure 2.15(a)**]. The observed narrowing suggests that the presence of the LG beam enhances the lifetime of the Zeeman coherences probed by the Gaussian beam in further support of our computational analysis.

To further confirm that the observed narrowing is associated with spatial profile of the LG field, a comparative study was carried out with a ring-shaped (RS) beam which is essentially a doughnut shaped beam but with zero OAM. RS beam was generated by using a circular mask (Hamid *et al.*, 2006). The experimental set-up given in **Figure 2.8** was used to measure the Hanle EIA resonances with a circularly polarized Gaussian, LG and RS beams (**Figure 2.16**). The beams were maintained at the same intensity.

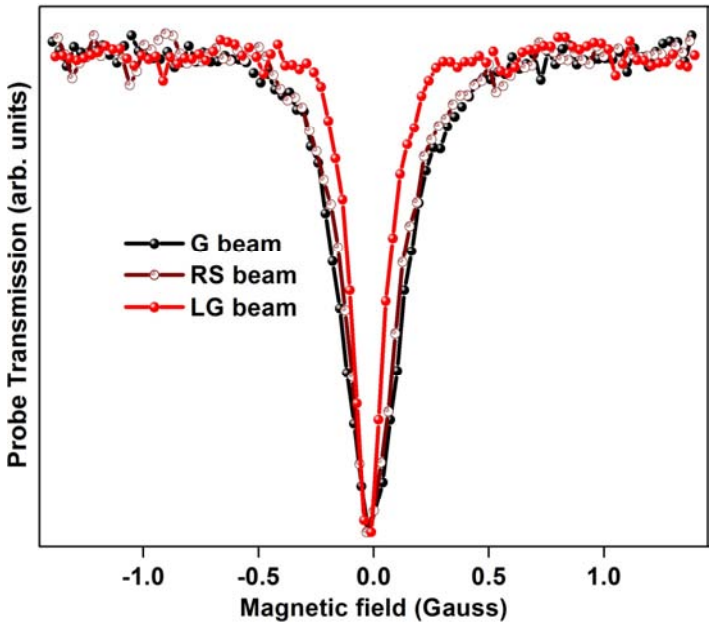

Figure 2.16: Measured Hanle EIA profiles for circularly polarized Gaussian, LG and ring-shaped beam locked to $F_g=2\rightarrow F_e'$ transition of Rb^{87}.

The measured linewidths were found to be 0.283 Gauss, 0.251 Gauss and 0.150 Gauss for the Gaussian, ring-shaped and LG beams respectively. It is clear that the resonances obtained with a Gaussian and ring-shaped beams have comparable widths while the LG beam produces a

distinctly narrower resonance. Since a ring-shaped beam with no OAM behaves similar to a Gaussian beam, it is clear that the OAM of the LG field plays a crucial role in influencing the Zeeman coherence lifetime.

Interesting inferences in support of our results could be made by comparing independent degenerate four-wave mixing experiments performed with a Gaussian beam by Lezama *et al.* (2000) and with a LG beam by Barreiro and Tabosa (2003).

Degenerate four-wave mixing (DFWM) is a phase sensitive non-linear process where the interaction depends upon the relative phases of all the beams and it yields Doppler free spectra (Lam and Abrams, 1982). Lezama *et al.* (2000), Barreiro and Tabosa, (2003) measured the DFWM spectra in a sample of cold atoms. In this case, backward FWM configuration was used where the counter-propagating forward (F) and the backward (B) beams (pump beams) with parallel linear polarization were maintained at the same frequency. The probe (P) beam making a small angle with respect to the forward beam was linearly polarized orthogonal to the pump beams. When the three beams ($\boldsymbol{F} \,//\, \boldsymbol{B} \perp \boldsymbol{P}$) interact with the non-linear medium, a phase conjugate (C) beam is generated due to the induced coherence grating between the pair of Zeeman sublevels in the ground and the excited states (Lezama *et al.*, 2000; Barreiro and Tabosa, 2003). All other experimental conditions being the same, the sub-natural FWM spectral linewidth obtained when Gaussian beam was used as the probe beam was found to be approximately 296 KHz[*] higher than the 200 KHz linewidth obtained with a LG beam used as the incident probe beam (Barreiro and Tabosa, 2003). Since the four-wave mixing spectrum originates from a long lived Zeeman ground state coherence (Barreiro and Tabosa, 2003), the use of a LG beam is found to enhance the Zeeman coherence lifetime in agreement with our results.

Further support is obtained when experiments on the topological study of stored optical vortices are considered. The storage time of the optical vortex state is limited by the life time of ground state coherences (Phillips *et al.*, 2001; Dutton and Ruostekoski, 2004). It was shown by Pugatch *et al.* (2007) that the LG mode (optical vortex) is topologically stable and could be stored in hot atomic vapor for 110 μs without diffusion. In comparison, the corresponding

[*] Linewidth from (Lezama *et al.*, 2000) was estimated by digitizing the reported data.

storage time for a Gaussian beam with a uniform phase and a dark center (zero OAM) was found to be only 10 μs. This confirms our conclusions that a non-zero azimuthal mode index is crucial to producing long-lived ground state coherences and hence enhanced storage times.

LG field induced narrowing of EIT/EIA profiles may have several important applications such as atomic clocks with higher precision, increased storage times/steeper dispersion in stopped light/slow light experiments. A brief insight into some of these applications is given in the third chapter.

2.5 Conclusions

In conclusion, the influence of a LG beam on the linewidth of electromagnetically induced Hanle EIT/EIA profiles has been studied. LG beam profile was seen to bring about a significant narrowing in the line shape of the Hanle resonance and ground state Zeeman coherence in comparison to a Gaussian beam. We have shown by computation and experiment that the azimuthal mode index of the LG field induces long-lived Zeeman coherences resulting in a significant narrowing of the Hanle EIT/EIA resonance.

A two-beam Hanle measurement, where the Hanle profile of the Gaussian beam was studied under the influence of the LG beam also confirms the observed behavior.

In further support of our conclusions, a comparative study of the Hanle EIA measurements were carried out with a ring-shaped beam which is essentially a doughnut shaped beam with zero OAM. This shows that the OAM associated with the LG beam which plays a crucial role in influencing the lifetime of the Zeeman coherences.

CHAPTER 3

Nonlinear magneto-optical rotation with a Laguerre Gaussian beam

3.1 Introduction

In the previous chapter we had studied the effect of the LG beam profile on the linewidth of the Hanle EIT/EIA resonances. It was shown that the azimuthal mode index associated with the LG beam brings about a significant narrowing in the line shape of the Hanle resonance in comparison to a Gaussian beam. In this chapter, we have investigated the role played by the LG field in coherent processes which do not depend on the transit relaxation time.

To study the dependence of the LG field induced narrowing on the polarization of the incident beam, a comparison was made between the transit effect limited polarization rotation signal in the Faraday (nonlinear Faraday signal) and the Voigt (nonlinear Voigt signal) geometry by locking the ECDL to the closed transition Rb^{87} $F_g=2\rightarrow F_e'=3$.

As mentioned in chapter 2, we were also interested in exploring other implications of the LG field influence. Therefore a Lambda system (described in **Section 1.5.1**) was taken and a detailed computational analysis was carried out to study EIT and reduced group velocity in the presence of the LG field.

3.2 Nonlinear magneto-optical rotation

3.2.1 Experimental details and results

NMOR measurements were carried out with Gaussian and LG fields using the experimental set-up as given in **Figure 3.1**. The probe beam was passed through a cylindrical paraffin coated Rb vapor cell (dimension: 8cm in diameter and 5cm long) with the ECDL locked to the $F_g=2\rightarrow F_e'$

=3 transition of Rb^{87}. The paraffin coated cell was placed inside a three layered Mu metal shield (Co-Netic alloy) to null the magnetic field in the transverse directions and the magnetic field was scanned along the direction of propagation of the beam (Faraday geometry) with the help of the solenoid (**Figure 3.1**). The balanced polarimetry arrangement [**Figure 1.11 (b)**] is used to carry out the NMOR measurements (**Section 1.5.4**). The rotation of the plane of polarization of the probe beam due to its interaction with the resonant medium is obtained by measuring the differential signal between the two photodiodes. A lock in amplifier was used to amplify the differential signal between the two PDs and the NMOR measurements were recorded on a cathode ray oscilloscope.

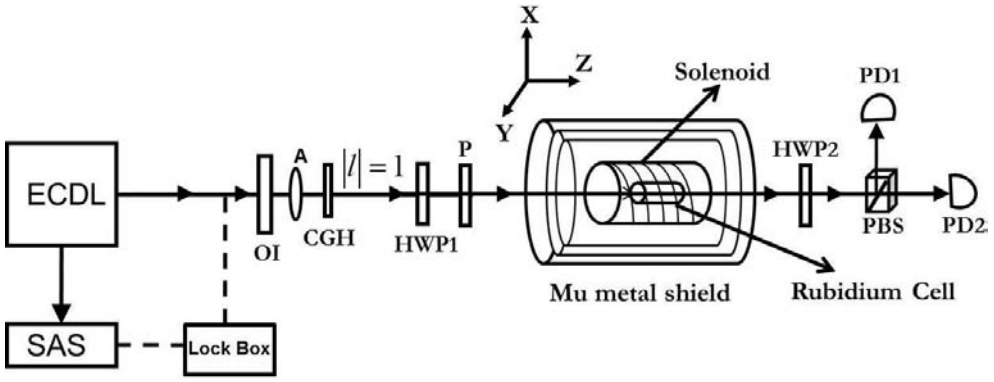

Figure 3.1: Experimental set-up used for measuring the NMOR signal with a LG beam, where PBS is a polarizing beam splitter. Balanced polarimetry arrangement is shown. Rest of the key is the same as used in **Figure 2.8**.

The two types of NMOR obtained with this experimental set-up are given in **Figure 3.2**. The linewidth of the wider resonance (NMOR-I) is limited by the transit effect (**Figure 3.2**). The relaxation time in this case is given by the time of flights of the atoms between the optical pumping and probing (the time the atom stays in the width of the laser beam).

The narrow resonance – NMOR-II (inset in **Figure 3.2**) is brought about by the creation and evolution of atomic polarization. Atomic polarization discussed in **Section 1.5.3**, refers to the polarization of the atoms due to optical pumping, precessing at a Larmor frequency of ω_L in the presence of the magnetic field. The linewidth in this case is determined by atomic depolarization rate, given by the time between the optical pumping and probing of the atoms after collisions with the cell walls and returning to the beam (Budker *et al.*, 1998, Budker *et al.*, 2002).

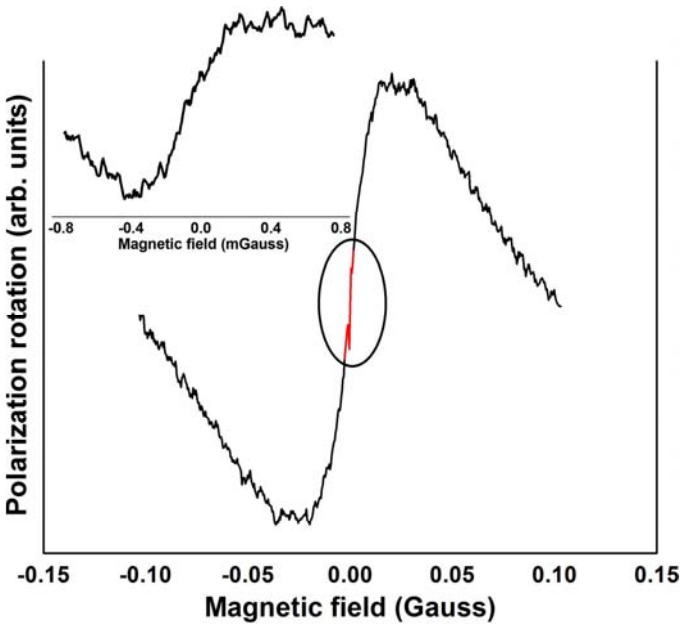

Figure 3.2: NMOR-I (due to the transit effect) - wider resonance measured for LG beam, locked to the $F_g = 2 \rightarrow F_e' = 3$ transition of Rb^{87}. The measured NMOR-II signal due to the coherence effect- narrow resonance (encircled in the plot) is shown in the inset.

The time evolution of the polarized alkali atoms in the presence of the magnetic field is limited by (a) the spin exchange collision rate and (which will be discussed in detail in the next section) (b) the collisions of these atoms with the walls of the cell (Budker *et al.*, 1998, Budker *et al.*, 2000). Atoms are completely depolarized when colliding with the walls of an ordinary uncoated vapor cell. On the other hand, a paraffin coated (anti-relaxation) cell (Alexandrov *et al.*, 1996) enables the atoms to undergo many thousand collisions with its wall before depolarizing them. The spin destruction probability is significantly reduced by the paraffin coating when atoms collide with its surface as it contains no free electron spin. Moreover, it yields low adsorption energy in comparison to the bare glass surface thereby reducing the time spent by an adsorbed alkali atoms in its surface (Seltzer *et al.*, 2010). Therefore paraffin coated cell increases decoherence time by preserving the atomic polarization on collisions with the cell walls, thus bringing about a narrower resonance. The smallest such observed linewidth for NMOR-II has been reported by Budker *et al.* (1998) corresponding to 1 μG.

It can be seen from **Figure 3.3** that NMOR-I due to the LG beam profile is distinctly narrower than the one obtained with the Gaussian beam. The measured linewidths of the NMOR-

I profile for Gaussian and LG beams with OAM, $|l|$ = 1, 2 and 3 are 0.056 G, 0.033 G, 0.030 G and 0.027 G respectively (**Figure 3.3**). NMOR-I and NMOR-II measurements were carried out at the Atomic and Optical Physics lab at Indian Institute of Science, Bangalore.

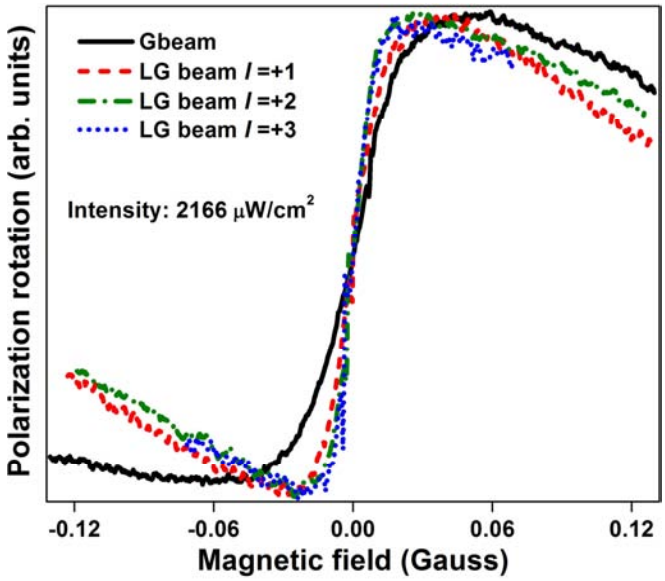

Figure 3.3: Measured NMOR-I for Gaussian and LG fields with $|l|$ = 1, 2 and 3 locked to the F_g =2→F_e' =3 transition of Rb^{87}.

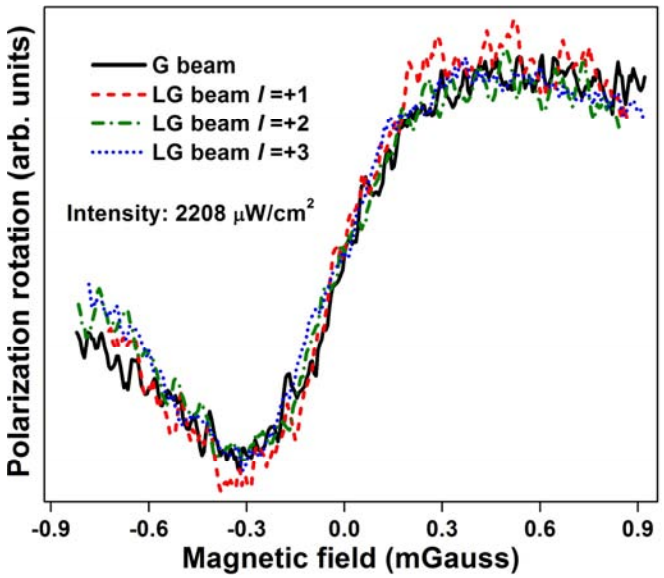

Figure 3.4: Measured NMOR-II resonance for Gaussian and LG fields with $|l|$ = 1, 2 and 3 locked to the F_g =2→F_e' =3 transition of Rb^{87}.

The width of NMOR-II for the Gaussian and LG beam profiles with OAM of $|l|$= 1, 2 and 3 are 0.327 mG, 0.339 mG, 0.359 mG ad 0.389 mG respectively (**Figure 3.4**). The linewidth of the

NMOR-II that has been observed in the experiment (**Figure 3.4**) was found to have higher linewidths (of the order of 10^{-2} G) compared to the observations made by the Budker *et al.* (1998). This could be attributed to the presence of residual magnetic field in the order of milli-Gauss in the Mu metal shield.

There is no significant change in the linewidths of NMOR-II between the Gaussian and LG beam profiles (**Figure 3.4**). Since the spin exchange collisions is the principal relaxation mechanism for the atomic polarization in paraffin coated cell, it can be concluded that the narrow resonance is not influenced by the spatial profile of the LG beam.

3.2.2 Computational results

To verify the experimental results that have been discussed previously, a comparison has been made between the contribution to the relaxation matrix $\left[\tilde{R}(\tilde{\rho})\right]$, due to both transit effect and the coherence effect (3.1). $\tilde{R}(\tilde{\rho})$ comprises of the relaxation terms Γ and γ. Where, Γ represents the spontaneous decay rate of the excited state and the decoherence rate γ, is given by either (Malakyan *et al.*, 2004),

(a) The time the atoms stay in the width of the laser beam (Renzoni and Arimondo, 1998; Patnaik *et al.*, 2007) – NMOR-I or

(b) Time between the optical pumping and probing of the atoms after collisions with the cell walls and returning to the beam; the effective lifetime in this case is equal to the time of the atomic round trip (Pustelny, 2007) – NMOR-II.

The Liouville equation given by (2.17) in **Section 2.2** can be re-written after incorporating the relaxation mechanism due to the transit effect and the spin exchange collision.

$$\frac{d\tilde{\rho}}{dt} = \frac{i}{\hbar}\left[\tilde{\rho}, \tilde{H}\right] + \tilde{R}(\tilde{\rho})_{\mathrm{TE}} + \tilde{R}(\tilde{\rho})_{\mathrm{SE}} + \Lambda(\tilde{\rho}), \tag{3.1}$$

where, $\tilde{R}(\tilde{\rho})_{\mathrm{TE}}$ is the relaxation operator due to the transit effect. $\tilde{H}$ represents the total Hamiltonian of the system after making the RWA and is given by (2.16). $\Lambda(\tilde{\rho})$ denotes the re-

population matrix of the ground state due to the relaxation terms Γ and the transit relaxation time (2.19).

The third term in the RHS of (3.1) represents the collisional relaxation rate, i.e. the spin exchange relaxation rate (Harper, 1972; Corney, 1977). In the spin exchange relaxation process, the spin orientations of the colliding atoms flip but their total angular momentum is conserved and therefore the overall orientation of the colliding atoms must be preserved. The force responsible for this process is electrostatic in nature (Harper, 1972; Corney, 1977). The relaxation mechanism between two colliding atoms can be expressed as (Harper, 1972)

$$\mathrm{A}(\uparrow)+\mathrm{B}(\downarrow)\rightarrow \mathrm{A}(\downarrow)+\mathrm{B}(\uparrow). \tag{3.2}$$

The difference arising between the singlet and the triplet potential (3.4) can be attributed to the origin of the spin exchange interaction. The interaction potential as a function of the interatomic distance is given by (Harper, 1972)

$$V(r)=V_0(r)+\vec{S}_A.\vec{S}_B V_1(r), \tag{3.3}$$

where, $\vec{S}_A$ and $\vec{S}_B$ represents the electronic spin operators of A and B respectively and S_A+S_B is conserved. $V_0(r)$ and $V_1(r)$ are the interatomic potential due to the spin independent and spin dependent part respectively. The singlet and the triplet potentials are given by (Harper, 1972)

$$\left.\begin{aligned} V_s(r)&=V_0(r)-3/4V_1(r)\\ V_t(r)&=V_0(r)+1/4V_1(r)\end{aligned}\right\}. \tag{3.4}$$

Let us consider species of atoms A with density matrix ρ_A and number density N_A colliding with another species of atoms B with the corresponding density matrix ρ_B and number density N_B. The rate of change of density matrix ρ_A, is given by (Ressler *et al.*, 1969; Harper, 1972; Harper and Tam, 1977)

$$\tilde{R}(\tilde{\rho})_{\mathrm{SE}}=\frac{d}{dt}\rho_A=\underbrace{\frac{1}{\tau_{\mathrm{SE}}}\left(\rho_A^e-\rho_A\right)}_{\mathrm{I}}+\underbrace{\frac{2iK}{\tau_{\mathrm{SE}}}\left[\ \vec{S}_A\cdot\left\langle\vec{S}_B\right\rangle,\rho_A\ \right]}_{\mathrm{II}}. \tag{3.5}$$

K gives the shift parameter which depends upon the singlet and the triplet potentials. $1/\tau_{\mathrm{SE}}$ represents the spin exchange relaxation rate and by standard result from the kinetic theory, it is given by (Ressler *et al.*, 1969; Harper, 1972; Corney, 1977)

$$\gamma_{\mathrm{SE}} = N_B \sigma_{\mathrm{SE}}\ v_{\mathrm{rel}}, \tag{3.6}$$

where, v_{rel} is the average relative velocity. σ_{SE} is the effective spin exchange or mean depolarization cross section and for Rb atoms it is found to be $\cong 10^{-14}\,\mathrm{cm}^2$. (Ressler *et al.*, 1969; Harper, 1972; Corney, 1977).

The term II of (3.5) can be neglected by taking into consideration the dominant effect of the spin exchange collision (Ressler *et al.*, 1969; Harper, 1972; Harper and Tam, 1977). The term I of (3.5) indicates that ρ_A relaxes to ρ_A^e at the rate $1/\tau_{\mathrm{SE}}$ immediately after having undergone spin exchange collision with atoms of species *B*. The density matrix ρ_A and ρ_A^e can be written as (Harper, 1972; Harper and Tam, 1977)

$$\rho_A = \zeta_A + \vec{A}_A \cdot \vec{S}_A \tag{3.7}$$

$$\rho_A^e = \zeta_A \left(1 + 4\left\langle \vec{S}_B \right\rangle \cdot \vec{S}_A\right) \tag{3.8}$$

where, ζ_A and $\vec{A}_A$ are operators which affect only the nuclear spin of *A*.

On substituting the expression for ρ_A and ρ_A^e in (3.5) and neglecting the term II as discussed previously, we have

$$\tilde{R}(\tilde{\rho})_{\mathrm{SE}} = \frac{d}{dt}\rho_A = \frac{1}{\tau_{\mathrm{SE}}}\left[\ \zeta_A\left(1 + 4\left\langle \vec{S}_B \right\rangle \cdot \vec{S}_A\right) - \left(\zeta_A + \vec{A}_A \cdot \vec{S}_A\right)\ \right] \tag{3.9}$$

On simplifying, the mechanism of the spin exchange collisions reduces as

$$\tilde{R}(\tilde{\rho})_{\mathrm{SE}} = \tilde{R}_{\mathrm{SE}} = \frac{1}{\tau_{\mathrm{SE}}}\left(4\zeta_A \left\langle \vec{S}_B \right\rangle - \vec{A}_A\right) \cdot \vec{S}_A \tag{3.10}$$

Incorporating (3.10) in (3.1), the Liouville equation gets modified as

$$\frac{d\tilde{\rho}}{dt}=\frac{i}{\hbar}\left[\tilde{\rho},\tilde{H}\left(r,\phi\right)\right]+\tilde{R}\left(\tilde{\rho}\right)_{\mathrm{TE}}+\left\{\frac{1}{\tau_{\mathrm{SE}}}\left(4\zeta_A\left\langle\vec{S}_B\right\rangle-\vec{A}_A\right)\cdot\vec{S}_A\right\}+\Lambda\left(\tilde{\rho}\right) \qquad \textbf{(3.11)}$$

As mentioned in the previous chapter, the azimuthal mode index of the LG field results in a spatially dependent Rabi frequency, Ω_{LG} given by (2.12). This in turn renders the total Hamiltonian of the system spatially dependent $\left[\tilde{H}=\tilde{H}\left(r,\phi\right)\right]$.

It can be seen from (3.7) and (3.8) that the density matrix element involved in the spin exchange mechanisms is independent of spatial coordinates. Therefore the spatially dependent Hamiltonian $\tilde{H}\left(r,\phi\right)$ can be decoupled from these density matrix elements and consequently, Ω_{LG} has no effect on spin exchange mechanism. As a result of which the OAM '*l*' associated with LG beam has no influence on the NMOR-II resonance. On the other hand, in the case of the transit effect [second term of (3.11)], the density matrix is dependent on spatial coordinates (due to the nature of the transit relaxation) and therefore on '*l*' in the presence of a LG field. This accounts for the observed narrowing induced by the LG field in the transit effect limited NMOR profile.

Therefore, it can be inferred that, unlike NMOR-I, the induced atomic coherence in the case of NMOR-II resonance persists even if the atom leaves the laser beam. These results support our conclusion that the transit effect limited Hanle and NMOR resonances are strongly influenced by the OAM associated with the LG field.

The transit effect limited NMOR was computed for the atomic transition $J_g=1\rightarrow J_e=0$ (**Figure 2.1**) due to the Gaussian and LG modes as shown in **Figure 3.5**. The azimuthal mode index associated with the LG beam is taken as $|l|=1$, 2 and 3 with $\Gamma/\gamma=1000$, $\Delta_{pr}=0, b_0=1$, Ω_o/Γ, $\Omega_{LG}^o/\Gamma=1$, and $w(z)=w_o=3\mathrm{mm}, 4\mathrm{mm}$ and 5mm for $|l|=1$, 2 and 3 respectively.

The computed linewidths for transit effect limited NMOR due to the Gaussian and LG beams with $|l|$ = 1, 2 and 3 were found to be 0.031 MHz, 0.011 MHz, 0.007 MHz and 0.005 MHz respectively (**Figure 3.5**).

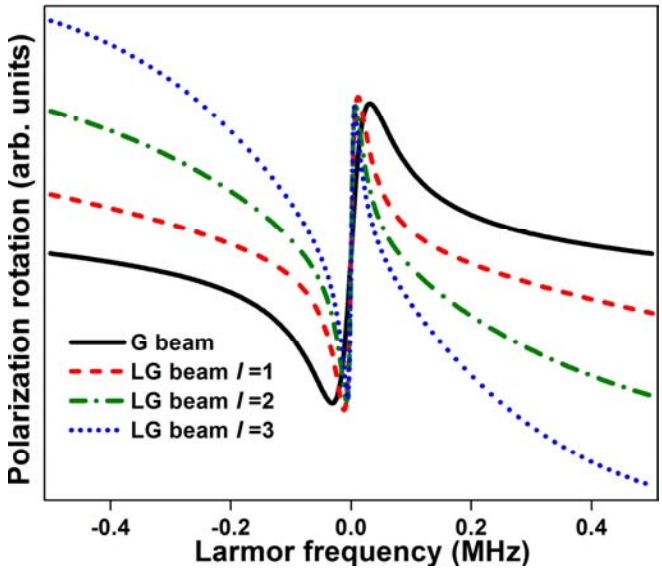

Figure 3.5: Measured NMOR-II for Gaussian and LG fields with $|l|$=1, 2 and 3 locked to the F_g =2→F_e'=3 transition of Rb^{87}, using $\Gamma/\gamma = 1000$, $\Delta_{pr} = 0$, $\Omega_o/\Gamma = 1$, $\Omega_{LG}^{o}/\Gamma = 1$, $b_0 = 1$ and $w(z) = w_o = 3\text{mm}, 4\text{mm}$ and 5mm for $|l|$ =1, 2 and 3 respectively.

It can be seen that the NMOR-I profile with LG beam is significantly narrower than the one that is obtained due to the Gaussian beam, consistent with the experimental results discussed in the previous section. The computed linewidth of the LG NMOR-I profile was plotted as a function of the OAM associated with it (**Figure 3.6**). As observed in the Hanle resonances [**Figure 2.7 and 2.13**], the extent of narrowing between the measured linewidths due to $|l|$=2 and 3 is lesser than that for $|l|$=1 and 2.

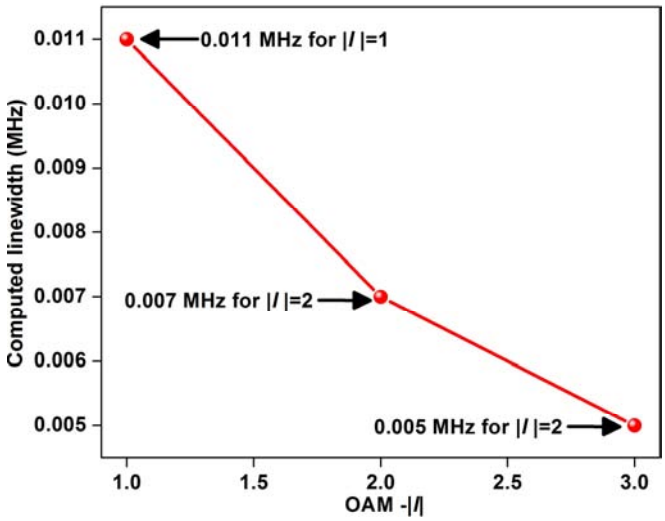

Figure 3.6: Linewidth of the computed transit effect limited NMOR profile for LG field as a function of OAM $|l|$ associated with it.

3.3 Nonlinear Faraday and Voigt signals

3.3.1 Experimental details and results

To verify if the narrowing induced by the LG field could be polarization dependent the polarization rotation signal due to the Gaussian and LG fields was studied in the Faraday geometry (nonlinear Faraday signal) and the Voigt geometry (nonlinear Voigt signal). The schematic of the experimental set-up that was used is shown in **Figure 3.7**.

In the nonlinear Faraday or NMOR measurements, the probe beam is sigma (σ) polarized (the polarization oriented at an angle of 90° with respect to the magnetic field $\vec{B}$) as shown in **Figure 3.7(a)**. The interaction of the probe beam with the resonant medium results in the rotation of the plane of polarization of the σ (σ^+ and σ^-) polarized beam which can be measured by using the balanced polarimetry arrangement (**Section 1.5.4**).

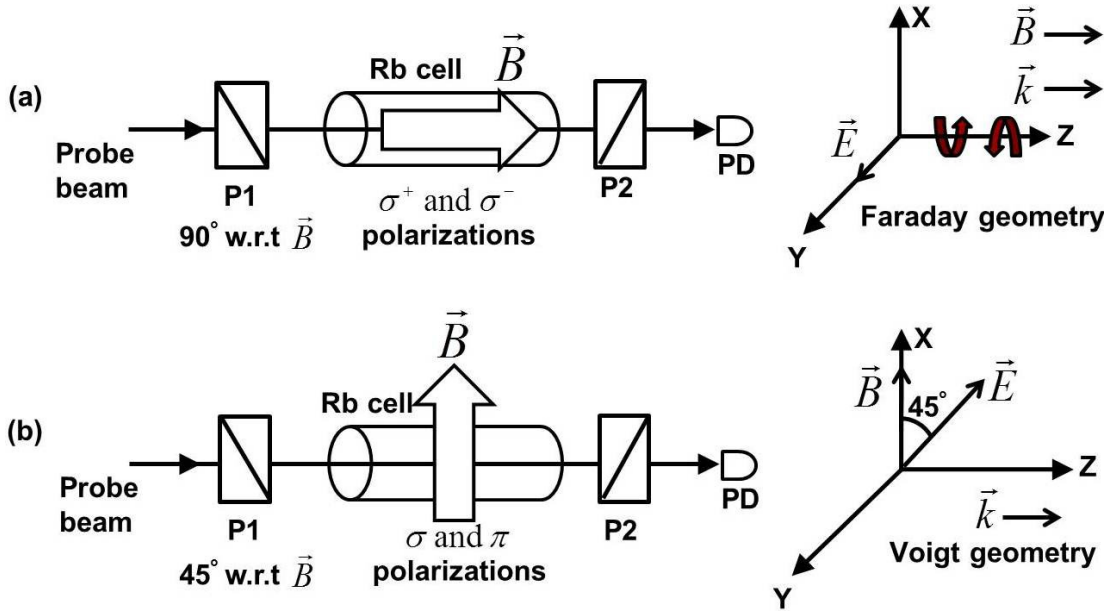

Figure 3.7: Illustrates the schematic of the experimental set-up to measure the polarization rotation signal in (a) Faraday geometry and (b) Voigt geometry.

In the nonlinear Voigt signal measurement, the polarizer P1 in **Figure 3.7 (b)** is oriented at an angle of 45° with respect to the magnetic field which is scanned perpendicular to the direction of the propagation of the beam (Drake *et al.*, 1988). Hence in this geometry, the probe beam comprises of σ and π polarizations and to enable the detection of the rotation in their plane of

polarization (σ and π), the polarizer P2 is aligned crossed with respect to P1 [**Figure 3.7 (b)**].

In case of the Faraday rotation, only $\Delta m = \pm 2$ coherences are created as the sigma polarized light drives the optical transition with selection rules $\Delta m = \pm 1$ (Drake *et al.*, 1988) (**Figure 3.8**). On the other hand, in the Voigt rotation, since both the σ (selection rule $\Delta m = \pm 1$) and π (selection rule $\Delta m = 0$) polarizations are involved, this results in the creation of $\Delta m = \pm 1$ and $\Delta m = \pm 2$ (Drake *et al.*, 1988; Nishina and Lax, 1969) (**Figure 3.8**). As mentioned in chapter 1 (1.41), the Faraday rotation is proportional to the difference in the refractive indices associated with the left and the right circularly polarized beams respectively and the Voigt effect is proportional to the difference in the absorption of light polarized along and perpendicular to the direction of magnetic field (Nienhuis and Schuller, 1998; Schuller *et al.*, 1991). The generalized expressions for the Faraday (φ_F) and the Voigt rotation (φ_V) is given by

$$\varphi_F \propto \left\{ D_{\sigma^+} - D_{\sigma^-} \right\} \tag{3.12}$$

$$\varphi_V \propto \left\{ A_\pi - \left(A_{\sigma^+} + A_{\sigma^-} \right) \right\}, \tag{3.13}$$

where, A and D represents the absorption and dispersion for the particular polarization component respectively.

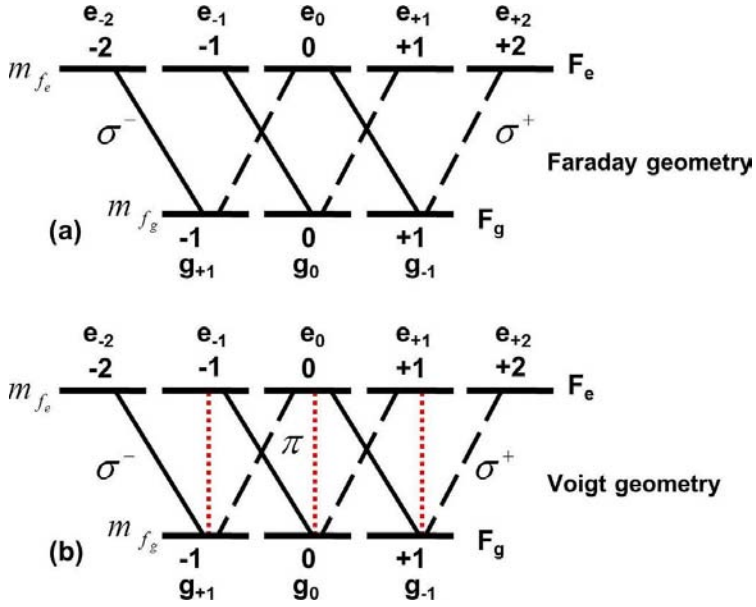

Figure 3.8: Illustrates the atomic level configuration $J_g = 1 \rightarrow J_e = 2$ and the allowed transitions for (a) Faraday geometry and (b) Voigt geometry.

The nonlinear Faraday and the Voigt rotation measurements were carried out to verify if the narrowing induced by the LG beam profile could be polarization dependent. Rb vapor cell was used and the ECDL was locked to the closed transition Rb^{87} $F_g=2\rightarrow F_e'=3$. The measured nonlinear Faraday and the Voigt signal due to Gaussian and LG beam (with OAM, $|l|=1$) maintained at an intensity of 1186 $\mu W/cm^2$ is shown in **Figure 3.9** and **3.10**.

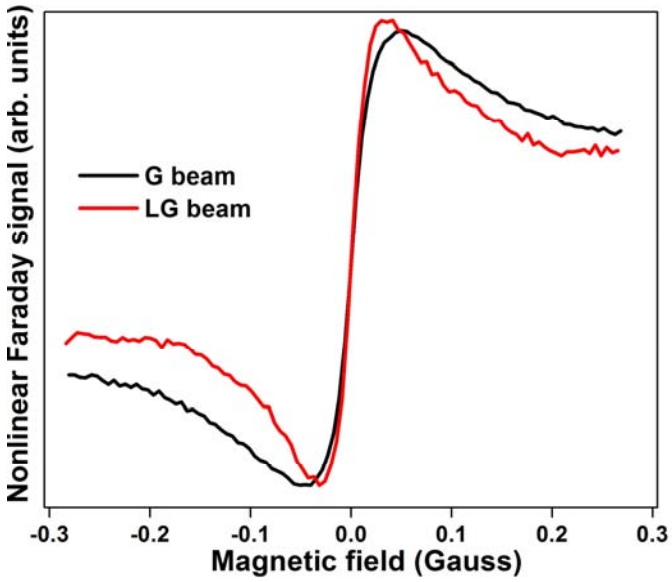

Figure 3.9: Measured nonlinear Faraday signal due to the Gaussian and LG fields (with OAM, $|l|=1$) locked to the $F_g=2\rightarrow F_e'=3$ transition of Rb^{87}.

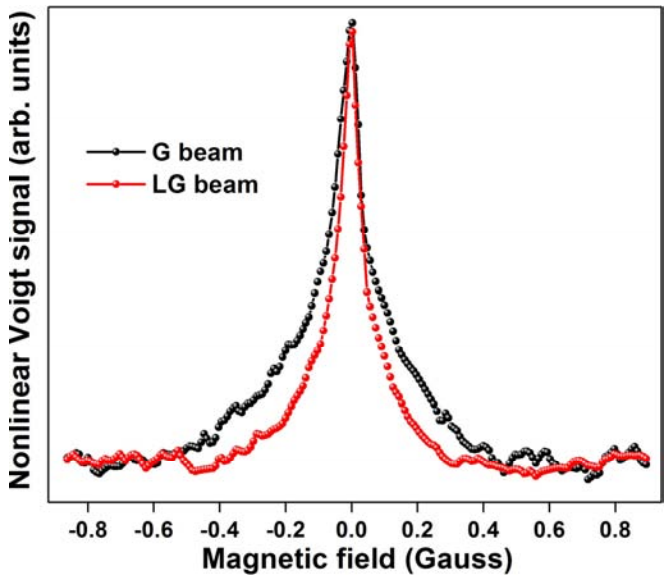

Figure 3.10: Measured nonlinear Voigt signal due to the Gaussian and LG fields (with OAM, $|l|=1$) locked to the $F_g=2\rightarrow F_e'=3$ transition of Rb^{87}.

The nonlinear Faraday signal due to LG beam is significantly narrower than the one obtained with the Gaussian beam with line-widths of 0.057 G and 0.037 G for Gaussian and LG fields respectively (**Figure 3.9**). The percentage of narrowing in the line-width of the nonlinear Faraday signal was found to be 35%.

The linewidth of the measured nonlinear Voigt signal due to the Gaussian and LG fields (with OAM, $|l|=1$) were found to be 0.200 G and 0.112 G respectively (**Figure 3.10**). Again, it can be seen that LG field brings about a significant narrowing in the nonlinear Voigt signal in comparison to the Gaussian beam. The percentage of narrowing in this case was found to be 45%.

3.3.2 Computational results and discussions

To explain the observed behavior reported in the previous section, the nonlinear Faraday and Voigt signal has been computed for a simple two level atomic system $J_g=1 \rightarrow J_e=0$ (**Figure 2.1**) for Gaussian and LG beams. The expressions for the Faraday and Voigt rotation for this atomic system is given by (Nienhuis and Schuller, 1998; Schuller *et al.*, 1991; Malakyan *et al.*, 2004)

$$\varphi_F = \frac{\pi \nu_o}{3\Omega c}\left\langle \alpha_e J_e \right\| d \left\| \alpha_g J_g \right\rangle^2 \left\{ \mathrm{Re}[\rho_{e_0 g_{-1}}] - \mathrm{Re}[\rho_{e_0 g_{+1}}] \right\} \tag{3.14}$$

$$\varphi_V = \frac{\pi \nu_o}{3\Omega c}\left\langle \alpha_e J_e \right\| d \left\| \alpha_g J_g \right\rangle^2 \left\{ \mathrm{Im}[\rho_{e_0 g_0}] - \left(\mathrm{Im}[\rho_{e_0 g_{-1}}] + \mathrm{Im}[\rho_{e_0 g_{+1}}] \right) \right\}, \tag{3.15}$$

where, the angled bracket represents the reduced matrix element defined in (2.7), ν_o is the frequency difference between the ground and the excited states in the absence of the magnetic field and Ω denotes the Rabi frequency and for the Gaussian and LG mode it is defined in (2.11) and (2.12) respectively.

In the computational analysis, the OAM associated with the LG field is taken as $|l|=1$, using $w_o = 3\mathrm{mm}$, $\Gamma/\gamma = 400$, $\Delta_{pr} = 0$, $\Omega^o_{LG}/\Gamma = 0.05$, $\Omega_o/\Gamma = 0.05$ and $b_0 = 1$. The computed nonlinear Faraday and Voigt signals are shown in **Figure 3.11**. The LG beam profile brings about a significant narrowing in the computed nonlinear Faraday and Voigt rotation signal (**Figure 3.11**), the narrowing found to be more prominent in the latter case (by 11%), consistent with the

experimental results (by 9%) that have been observed in the previous section. The percentage of narrowing in the linewidth of the polarization rotation signal induced by the LG beam with respect to the Gaussian beam in the Faraday and Voigt geometry for the atomic system $J_g=1 \rightarrow J_e=0$ has been summarized in **Table 3.1**.

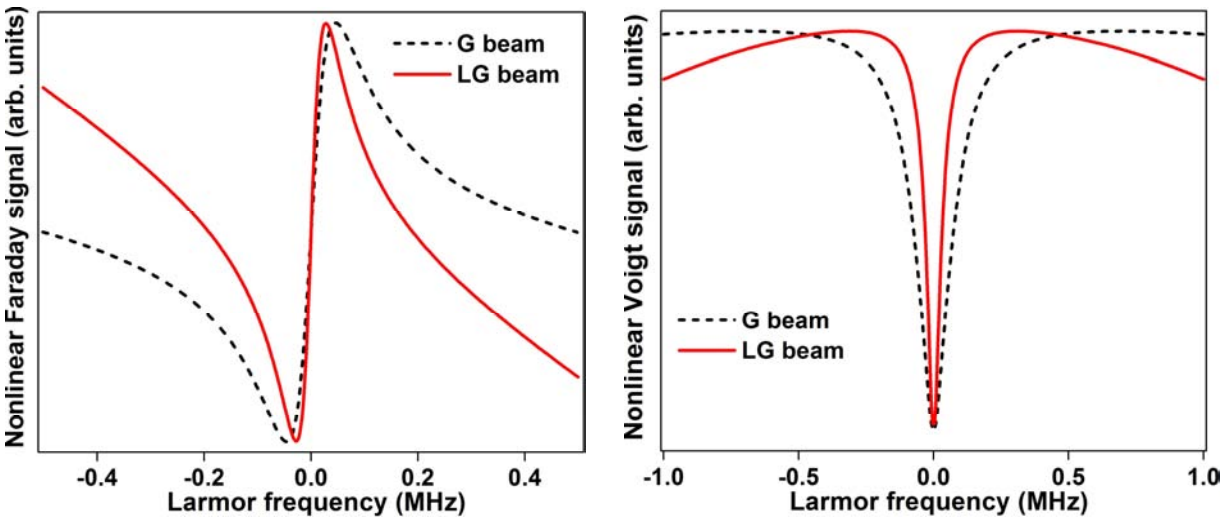

(a) (b)

Figure 3.11: Computed polarization rotation signal for (a) Faraday and (b) Voigt geometry due to Gaussian and LG field for the transition $J_g=1 \rightarrow J_e=0$, using $\Delta_{pr}=0$, $b_0=1$ $\Gamma/\gamma=400$, $\Omega_o/\Gamma=0.05$, $\Omega_{LG}^{o}/\Gamma=0.05$ and $w(z)=w_o=3\text{mm}$ for $|l|=1$.

Table 3.1: Gives the linewidth of the polarization rotation signal for different configurations due to the Gaussian and the LG beams to illustrate the percentage of narrowing in each case for the atomic system $J_g=1 \rightarrow J_e=0$.

Configuration	Linewidth		Percentage of narrowing
	G beam	LG beam	
Measured Nonlinear Faraday signal	0.057 Gauss	0.037 Gauss	35%
Measured Nonlinear Voigt signal	0.200 Gauss	0.112 Gauss	44%
Computed Nonlinear Faraday signal	0.046 MHz	0.025 MHz	46%
Computed Nonlinear Voigt signal	0.155 MHz	0.066 MHz	57%

To probe this behavior further, nonlinear Faraday and Voigt signals were analyzed for the atomic transition $J_g = 1 \rightarrow J_e = 2$ (**Figure 3.8**) as it represents an EIA system (Lezama *et al.*, 1999; Renzoni *et al.*, 2001). The repopulation matrix Λ_Γ for this atomic system is rewritten such that the individual contributions to the transfer of coherence (TOC) (**Section 1.5.2**) channel from the excited state coherences can be separated out in the computation (Ram *et al.*, 2009). The repopulation matrix can be expressed as 8×8 matrix of the form

$$\Lambda_\Gamma = \begin{pmatrix} A & B \\ C & D \end{pmatrix}. \tag{3.16}$$

Here A is a 3×3 matrix for the transitions $J_g = 1 \rightarrow J_e = 2$, where the diagonal terms and the off-diagonal terms comprises of the excited state population and the excited state coherences respectively.

The other sub matrices $B(3\times5)$, $C\ (5\times3)$ and $D\ (5\times5)$ are null matrices. The multiplicative constants b_0 (diagonal terms), b_1 and b_2 (off-diagonal terms), featuring in the matrix A are the branching ratio components of a transition. The transition is closed when all these constants are equal to 1. While b_0 controls the transfer of population channel, b_1 and b_2 controls the TOC channel with $\Delta m = \pm1$ and ±2 respectively.

The matrix A is given by

$$A = \begin{pmatrix} \Lambda(+1,+1) & \Lambda(+1,0) & \Lambda(+1,-1) \\ \Lambda(0,+1) & \Lambda(0,0) & \Lambda(0,-1) \\ \Lambda(-1,+1) & \Lambda(-1,0) & \Lambda(-1,-1) \end{pmatrix}. \tag{3.17}$$

Examples of diagonal and off-diagonal terms are illustrated below

$$\Lambda(+1,+1) = b_0\Gamma\sum_{n=0}^{2}\left\{\mathrm{CG}^{J_e m_{e_n}}_{J_g m_{g_{n-1}},\, J_g m_{g1}}\right\}^2 \rho_{e_n e_n} \tag{3.18a}$$

$$\Lambda(+1,0) = b_1\Gamma\sum_{n=-1}^{1}\left\{\mathrm{CG}^{J_e m_{e_{n+1}}}_{J_g m_{g_n},\, J_g m_{g1}}\right\}\left\{\mathrm{CG}^{J_e m_{e_n}}_{J_g m_{g_n},\, J_g m_{g0}}\right\} \rho_{e_{n+1} e_n} \tag{3.18b}$$

$$\Lambda(+1,-1) = b_2\Gamma\sum_{n=-2}^{0}\left\{\mathrm{CG}^{J_e m_{e_{n+1}}}_{J_g m_{g_n},\, J_g m_{g1}}\right\}\left\{\mathrm{CG}^{J_e m_{e_{n-1}}}_{J_g m_{g_n},\, J_g m_{g-1}}\right\} \rho_{e_{n+1} e_n} \tag{3.18c}$$

In the computation, the branching ratio components b_0 and b_2 are set as 1 and b_1 is turned 'on' or 'off' by removing the TOC contribution from $\Delta m = \pm 1$ coherences so as to illustrate the difference between the nonlinear Faraday and Voigt rotation. The computed nonlinear Faraday and Voigt signal for the atomic system $J_g = 1 \rightarrow J_e = 2$ using $\Delta_{pr} = 0, \Gamma/\gamma = 20000, \; b_0 = b_2 = 1,$ $\Omega_o/\Gamma = 0.1, \; \Omega_{LG}^o/\Gamma = 0.1$ and $w(z) = w_o = 3\text{mm}$ for $|l|=1$. The percentage of narrowing in the linewidth of the polarization rotation signal induced by the LG beam with respect to the Gaussian beam in the Faraday and Voigt geometry for the atomic system $J_g = 1 \rightarrow J_e = 2$ has been summarized in **Table 3.2**.

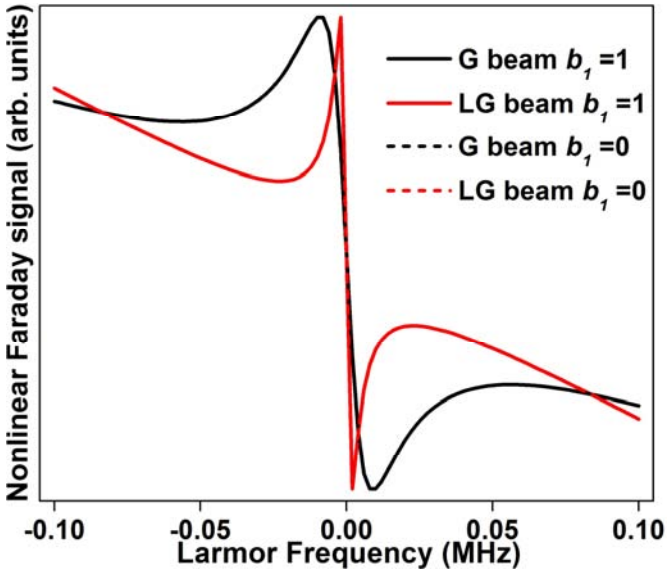

Figure 3.12: Computed polarization rotation signal for Faraday geometry due to Gaussian and LG field for the transition J_g=1→J_e=2 in the presence and in the absence of TOC with $\Delta m = \pm 1$ coherences by turning 'on' or 'off' b_1, using, $\Delta_{pr} = 0, \Gamma/\gamma = 20000,$ $b_0 = b_2 = 1, \; \Omega_o/\Gamma = 0.1, \; \Omega_{LG}^o/\Gamma = 0.1$ and $w(z) = w_o = 3\text{mm}$ for $|l|=1$.

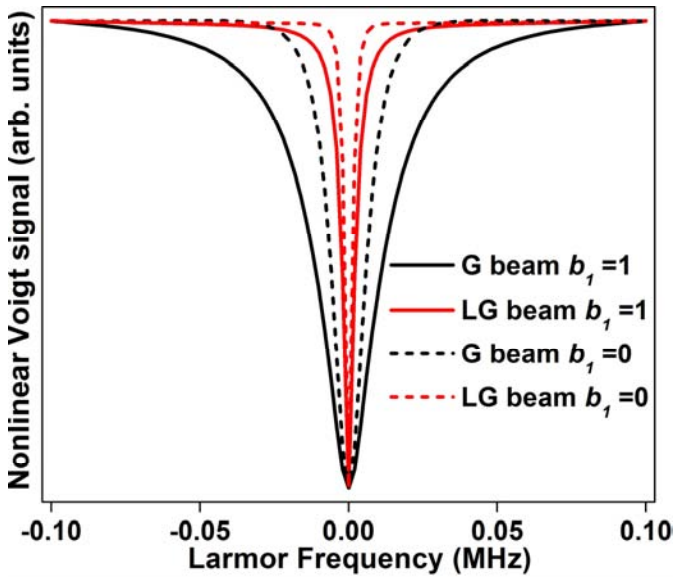

Figure 3.13: Computed polarization rotation signal for Voigt geometry due to Gaussian and LG field for the transition J_g=1→J_e=2. Other parameters are the same as used in **Figure 3.12**.

The presence or the absence of the contributions from $\Delta m = \pm 1$ coherences does not seem to have any influence on the line shape of the computed nonlinear Faraday signal under the influence of both the fields (**Figure 3.12**). As expected, there is a significant narrowing in the nonlinear Faraday signal induced by the LG field in comparison to the Gaussian field, with the percentage of narrowing found to be 75%. On the other hand, the branching ratio component, b_1 which controls the TOC channel with $\Delta m = \pm 1$ coherence, is found to influence the linewidth of the nonlinear Voigt signal, i.e. there is a reduction in its linewidth when b_1 is turned 'off' (**Figure 3.13**). The linewidth of the polarization signals that has been obtained for both the geometries in the presence and in the absence of TOC channel with $\Delta m = \pm 1$ coherences is summarized in **Table 3.2**. It can be seen that when b_1 is set as 1 (0), the percentage of narrowing in the nonlinear Voigt signal induced by the LG beam is found to be 83% (78%). As observed previously in the experiment and in the computation that was carried out for a J_g=1→J_e=0 atomic system (**Table 3.1**), in this case also the narrowing induced by the LG field with respect to the Gaussian beam is found to be more for the Voigt geometry (by 8%) in comparison to the Faraday geometry (**Table 3.2**).

Table 3.2: Gives the linewidth of the polarization rotation signal for different configurations due to the Gaussian and the LG beams in the absence of TOC channel with $\Delta m = \pm 1$ coherences for the atomic system J_g=1→J_e=2.

Configuration	b_1	Linewidth		Percentage of narrowing
		G beam (KHz)	LG beam (KHz)	
Computed Nonlinear Faraday signal	1	8.86	2.22	75%
	0	8.86	2.22	75%
Computed Nonlinear Voigt signal	1	26.79	4.56	83%
	0	11.65	2.58	78%

When the contributions due to the π coherence is removed in the computation (by setting b_1 to zero), the nonlinear Voigt signal is found to have almost similar linewidth as that of the nonlinear Faraday signal (**Table 3.2**).

Table 3.3: Comparison between the computed nonlinear Voigt signal that has been obtained for the atomic system J_g=1→J_e=2 due to the Gaussian and LG beam profile by turning 'on' or 'off' b_1

Configuration	Beam profile	Linewidth(KHz)		Percentage of narrowing
		$b_1 = 1$	$b_1 = 0$	
Computed Nonlinear Voigt signal	G beam	26.79	11.65	56%
	LG beam	4.56	2.58	43%

In **Table 3.3**, a comparison has been made between the computed nonlinear Voigt signal due to the Gaussian and LG beam profile by turning 'on' or 'off' b_1. The percentage of narrowing when b_1 is set from 1 to 0 comes out to be 56% and 43% for Gaussian and LG beam respectively (**Table 3.3**).

This implies that the influence of the LG field depends on the nature of the Zeeman coherences created (near-neighbor with $\Delta m = \pm 1$ coherence or next-near-neighbor with $\Delta m = \pm 2$ coherences in this case). This could account for the difference in extent of narrowing observed for nonlinear Faraday and Voigt rotation signals subject to Gaussian and LG fields. Thus it is seen that the influence of the LG field on the Zeeman coherence lifetime is polarization dependent.

3.4 Computational study of EIT using LG beam

As discussed in chapter 1 [**Section (1.5.1)**], EIT is a phenomenon in which the atomic medium is rendered transparent for a resonant probe field in the presence of another pump beam resonant with a common higher or lower energy level (Fleischhauer *et al.*, 2005). This process is generally associated with steep dispersion, brought about by enhancing the nonlinear susceptibility of the medium (Harris *et al.*, 1990). To explore other implications of the LG field influence, a Lambda system was taken (**Figure 1.3**) and a detailed computational analysis was carried out to study EIT and reduced group velocity in the presence of the LG field.

The probe beam with Rabi frequency Ω_{pr} and the coupling beam with Rabi frequency Ω_{pu} couples the ground states $|b\rangle$ and $|c\rangle$ respectively to the common excited energy level $|a\rangle$. The detuning in the probe and the coupling beams are given by Δ_{pr} and Δ_{pu} respectively. The frequency associated with the probe and the pump beam is given by ω_{pr} and ω_{pu}.

The unperturbed Hamiltonian H_o and the atom-field interaction Hamiltonian H_I for this lambda system is given by

$$H_o = \hbar \begin{pmatrix} \omega_a & 0 & 0 \\ 0 & \omega_b & 0 \\ 0 & 0 & \omega_c \end{pmatrix} \qquad \textbf{(3.19)}$$

$$H_I = \hbar \left\{ \left(|b\rangle\langle a| + |a\rangle\langle b| \right) \Omega_{pr} \cos \omega_{pr} t + \left(|c\rangle\langle a| + |a\rangle\langle c| \right) \Omega_{pu} \cos \omega_{pu} \right\}. \qquad \textbf{(3.20)}$$

Following the discussion in the previous chapter (**Section 2.2**), the total Hamiltonian of the system after making the RWA and slow variable transformation turns out to be

$$\tilde{H} = \frac{\hbar}{2}\begin{pmatrix} \omega_a & \Omega_{pr} & \Omega_{pu} \\ \Omega_{pr} & \omega_b & 0 \\ \Omega_{pu} & 0 & \omega_c \end{pmatrix}. \qquad \textbf{(3.21)}$$

The relation between the probe/coupling beam detuning and their frequencies for this lambda system is given by

$$\omega_{ab} - \omega_{pr} = -\Delta_{pr} \Rightarrow \omega_{ba} + \omega_{pr} = \Delta_{pr} \qquad \textbf{(3.22)}$$

$$\omega_{ac} - \omega_{pu} = -\Delta_{pu} \Rightarrow \omega_{ca} + \omega_{pu} = \Delta_{pu} \qquad \textbf{(3.23)}$$

where, $\omega_{ac} = \omega_a - \omega_c$ and $\omega_{ab} = \omega_a - \omega_b$.

The OBE (defined in **Section 2.2**) obtained for the lambda system is given by

$$\left.\begin{aligned} \dot{\tilde{\rho}}_{aa} &= \frac{i}{2}\left\{ \Omega_{pr}\left(\tilde{\rho}_{ab} - \tilde{\rho}_{ba}\right) + \Omega_{pu}\left(\tilde{\rho}_{ac} - \tilde{\rho}_{ca}\right) \right\} - \left(\gamma + \Gamma\right)\tilde{\rho}_{aa} \\ \dot{\tilde{\rho}}_{bb} &= \frac{i\Omega_{pr}}{2}\left(\tilde{\rho}_{ba} - \tilde{\rho}_{ab}\right) - \gamma\tilde{\rho}_{bb} + 1/2\,\Gamma\tilde{\rho}_{aa} + \gamma/2 \\ \dot{\tilde{\rho}}_{cc} &= \frac{i\Omega_{pu}}{2}\left(\tilde{\rho}_{ca} - \tilde{\rho}_{ac}\right) - \gamma\tilde{\rho}_{cc} + 1/2\,\Gamma\tilde{\rho}_{aa} + \gamma/2 \end{aligned}\right\} \text{Atomic populations } \textbf{(3.24a)}$$

$$\left.\begin{aligned} \dot{\tilde{\rho}}_{ab} &= i\left\{ \frac{\Omega_{pr}}{2}\left(\tilde{\rho}_{aa} - \tilde{\rho}_{bb}\right) - \frac{\Omega_{pu}}{2}\tilde{\rho}_{cb} + \Delta_{pr}\tilde{\rho}_{ab} \right\} - \left(\gamma + \frac{\Gamma}{2}\right)\tilde{\rho}_{ab} \\ \dot{\tilde{\rho}}_{ac} &= i\left\{ \frac{\Omega_{pu}}{2}\left(\tilde{\rho}_{aa} - \tilde{\rho}_{cc}\right) - \frac{\Omega_{pr}}{2}\tilde{\rho}_{bc} + \Delta_{pu}\tilde{\rho}_{ac} \right\} - \left(\gamma + \frac{\Gamma}{2}\right)\tilde{\rho}_{ac} \end{aligned}\right\} \text{Optical coherences}$$

(3.24b)

$$\dot{\tilde{\rho}}_{bc} = i\left(\frac{\Omega_{pu}}{2}\tilde{\rho}_{ba} - \frac{\Omega_{pr}}{2}\tilde{\rho}_{ac} + \left(\Delta_{pu} - \Delta_{pr}\right)\tilde{\rho}_{bc}\right) - \gamma\tilde{\rho}_{bc} \Big\} \text{ Zeeman coherences} \qquad \textbf{(3.24c)}$$

The 9 OBE (3×3) obtained for the Lambda system are numerically solved under the steady state conditions by setting the right hand side of (3.24) to 0 (Rochester, 2008). For the computation, the Gaussian beam is taken as the probe beam and the corresponding Rabi frequency, Ω_{pr} is given by (2.11). The absorptive and dispersive profile (Imaginary and real part of susceptibility) of the Gaussian beam is studied under the influence of LG beam, which is taken as the coupling beam with the Rabi frequency, Ω_{pu} modeled by (2.12). To make a comparative study, LG beam is replaced by Gaussian beam as the coupling beam.

The computed probe absorption and dispersion profile as a function of probe detuning are given in **Figures 3.14** and **3.15** respectively. The azimuthal mode index associated with the LG beam is taken as $|l|=1$ with $\Gamma/\gamma=1000$, $\Omega_{pu}/\Gamma=0.4$, $\Omega_{pr}/\Gamma=0.04$, $\Omega_{pu}/\Omega_{pr}=10$, $\Delta_{pu}=0$, $b_0=1$ and $w(z)\approx w_o=3\text{mm}$.

The linewidth of the probe absorption with Gaussian and LG beam used as the coupling beams are 0.164 MHz and 0.025 MHz respectively (**Figure 3.14**). It can be seen that the width of the transparency window (probe absorption profile) with LG beam used as the coupling beam is significantly narrower than the case when LG beam is replaced with a Gaussian beam.

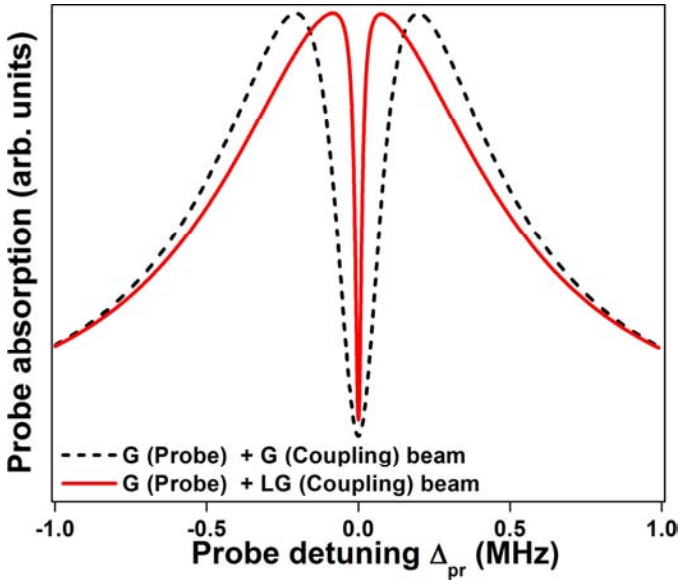

Figure 3.14: Computed probe absorption for the lambda system with $|l|=1, \Gamma/\gamma=1000$, $\Omega_{pu}/\Gamma=0.4$, $\Omega_{pr}/\Gamma=0.04$, $\Omega_{pu}/\Omega_{pr}=10$, $\Delta_{pu}=0$, $b_0=1$ and $w_o=3\text{mm}$.

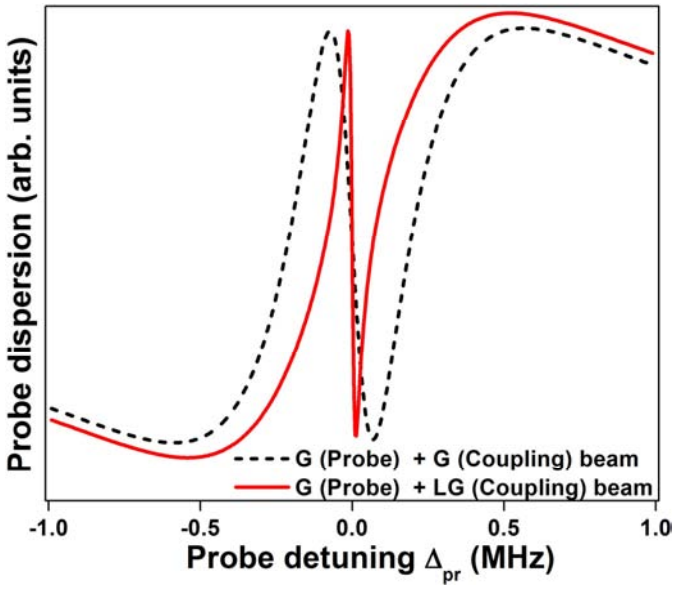

Figure 3.15: Computed probe dispersion for the lambda system. Parameters are the same as those used in **Figure 3.14**.

In the computational analysis with the lambda system, it was found that LG beam brings about a steeper dispersive profile when used as the coupling beam with a linewidth of 0.011 MHz, in comparison to the Gaussian beam (linewidth in this case was found to be 0.064 MHz) (**Figure 3.15**).

As discussed previously, in the EIT process, the region of steep dispersive profile is accompanied by small absorption (Harris *et al.*, 1990; Fleischhauer *et al.*, 2005). Consequently this results in different effects like reduced group velocity (due to the slowing of light), longitudinal pulse compression and storage of light (Harris *et al.*, 1990; Harris *et al.*, 1992; Fleischhauer *et al.*, 2005). Since LG beam brings about a steeper dispersive EIT profile than the Gaussian beam (**Figure 3.15**), it was of interest to make a comparative study between the group velocity due to the Gaussian and LG beam.

Group velocity, v_{gr} is defined as (Lighthill, 1965)

$$v_{gr} = \frac{d\omega_{pr}}{dk_{pr}}, \qquad \textbf{(3.25)}$$

where, the frequency of the probe beam, ω_{pr} is given in terms of the speed of light c, the wave number associated with the probe beam, k_{pr} and the refractive index n_R.

$$\omega_{pr} = \frac{ck_{pr}}{n_R} \tag{3.26}$$

$$v_{gr} = \frac{d}{dk_{pr}}\left(\frac{ck_{pr}}{n_R}\right) = \frac{c}{n_R} + \frac{d}{dk_{pr}}\left(\frac{1}{n_R}\right)ck_{pr} \tag{3.27}$$

$$\Rightarrow \frac{c}{n_R} - \frac{ck_{pr}}{n_R^{\,2}}\frac{dn_R}{dk_{pr}} \tag{3.28}$$

$$\because \quad \frac{dn_R}{dk_{pr}} = \frac{dn_R}{d\omega_{pr}} \times \frac{d\omega_{pr}}{dk_{pr}} = v_{gr}\frac{dn_R}{d\omega_{pr}}. \tag{3.29}$$

On substituting (3.29) in (3.28) we have,

$$v_{gr} = \frac{c}{n_R} - \frac{v_{gr}}{n_R^{\,2}}\frac{dn_R}{d\omega_{pr}}ck_{pr} \Rightarrow v_{gr}\left(1 + \frac{ck_{pr}}{n_R^{\,2}}\frac{dn_R}{d\omega_{pr}}\right) = \frac{c}{n_R} \tag{3.30}$$

$$v_{gr} = \frac{c/n_R}{\left(1 + \frac{ck_{pr}}{n_R^{\,2}}\frac{dn_R}{d\omega_{pr}}\right)} \approx \frac{c/n_R}{\frac{ck_{pr}}{n_R^{\,2}}\frac{dn_R}{d\omega_{pr}}} \approx \frac{c}{\omega_{pr}}\frac{1}{\left(\frac{dn_R}{d\omega_{pr}}\right)}$$

$$v_{gr} \approx \frac{c}{\omega_{pr}}\frac{1}{\left(\frac{d\,\mathrm{Re}(\chi)}{d\omega_{pr}}\right)}. \tag{3.31}$$

Let $\left(v_{gr}\right)_G$ and $\left(v_{gr}\right)_{LG}$ be the group velocity due to Gaussian and LG beam respectively as the coupling beam. The ratio of the group velocities are given by

$$\left(v_{gr}\right)_G / \left(v_{gr}\right)_{LG} = \frac{\left(\frac{d\,\mathrm{Re}(\chi)}{d\omega_{pr}}\right)_{LG}}{\left(\frac{d\,\mathrm{Re}(\chi)}{d\omega_{pr}}\right)_{G}} \tag{3.32}$$

From (3.22) $d\omega_{pr} \propto d\Delta_{pr}$,

$$\Rightarrow \left(v_{gr}\right)_G / \left(v_{gr}\right)_{LG} = \frac{\left(\frac{d\,\mathrm{Re}(\chi)}{d\Delta_{pr}}\right)_{LG}}{\left(\frac{d\,\mathrm{Re}(\chi)}{d\Delta_{pr}}\right)_{G}} = \frac{\mathrm{slope}\left(\mathrm{Re}(\chi)\right)_{LG}}{\mathrm{slope}\left(\mathrm{Re}(\chi)\right)_{G}}. \tag{3.33}$$

Summarizing,

$$\Rightarrow \left(v_{gr}\right)_G / \left(v_{gr}\right)_{LG} = \frac{\text{slope of the dispersive profile due to LG beam}}{\text{slope of the dispersive profile due to Gaussian beam}}. \tag{3.34}$$

The slopes of the dispersive profiles due to Gaussian and LG beams were calculated from **Figure 3.15** and the ratio of the respective group velocities were found to be

$$\Rightarrow \left(v_{gr}\right)_G / \left(v_{gr}\right)_{LG} \approx \frac{83}{14} = 6 \tag{3.35}$$

$$\Rightarrow \left(v_{gr}\right)_{LG} \approx \frac{1}{6}\left(v_{gr}\right)_G. \tag{3.36}$$

Thus it can be seen from (3.36) that the LG beam brings about a reduction in the group velocity approximately by a factor of 6 for the given lambda system with the parameters that have been mentioned in the computational analysis.

The reduced group velocity results in slowing down of light pulse inside the atomic medium (Harris and Hau,1999), followed by large group delays and spatial compression in the pulse propagation from kilometer to sub millimeter scale range inside the atomic medium (Hau *et al.*, 1999). The slow group velocity thus enables the stopping and storing of a light pulse, where in the information contained in a long pulse can be compressed to a very small spatial volume (Hau

et al., 1999; Fleischhauer and Lukin, 2000; Liu *et al.*, 2001). Also, the reduced group velocity of the light pulse increases the interaction time in the nonlinear atomic medium, in-turn enhancing the efficiency of the nonlinear process (Harris and Hau, 1999; Lukin *et al.*, 2000; Lukin and Imamoglu, 2001). All these find several potential applications in optical information storage, quantum information processing and laser cooling (Lukin *et al.*, 2000; Fleischhauer and Lukin, 2002; Harris, 2000).

Since the LG beam profile reduces the group velocity of the light pulse in comparison to a Gaussian beam, we may expect an enhancement in the storage time, time delay, the spatial compression and the efficiency of atomic coherence induced nonlinear optical process by replacing the Gaussian beam with the LG field. It would of considerable interest to attempt such experiments in future.

3.5. Conclusions

NMOR-I and the NMOR-II have been measured under the influence of the LG beam. Narrowing is observed in the line shape of the NMOR-I due to LG beam in comparison to a Gaussian beam. The spatial profile of the LG field is found to have no influence on the NMOR-II resonance where the linewidth is determined by spin exchange collisions. Therefore no significant change was found in the linewidths of the NMOR-II between the Gaussian and LG beam.

A comparison was made between the nonlinear Faraday and Voigt rotation signals for the transition $Rb^{87}(F_g=2\rightarrow F_e'=3)$ due to the Gaussian and LG beam. The extent of narrowing in the line shape of the polarization rotation signal induced by the LG beam was found to be more in the case of the Voigt geometry. It was shown that the influence of the LG field depends on the nature of the Zeeman coherences created (near-neighbor with $\Delta m = \pm 1$ coherence or next-near-neighbor with $\Delta m = \pm 2$ coherences in this case). This could possibly explain the difference in the percentage of narrowing induced by the LG beam with respect to the Gaussian beam between the nonlinear Faraday and Voigt rotation signal. Hence it can be concluded that the influence of the LG beam could be polarization dependent.

Computational analysis was carried out in a lambda system to study EIT and slow light in the presence of the LG field. It was found that the LG field induces a steeper dispersive EIT profile, bringing about a marginal reduction in the computed group velocity in comparison to the Gaussian beam. This may find applications in storing, stopping of light and atomic coherence enhanced nonlinear optical process.

CHAPTER 4

Ellipticity dependent polarization rotation studies with a Laguerre Gaussian beam

4.1 Introduction

It has been shown in the previous chapter that the extent of narrowing induced by the LG field in the line shape of the magneto-optical rotation was found to be more in the Voigt geometry in comparison to the Faraday geometry, implying that the influence of the LG beam is polarization dependent.

The production, detection and manipulation of higher order coherences is an area of emerging interest as they play a crucial role in enhancing the optical nonlinearities (Ledbetter *et al.*, 2008), as a result of which they find several applications like EIT (Harris, 1997), atomic magnetometry (Budker *et al.*, 2000; Yashchuk *et al.*, 2003; Hovde *et al.*, 2010), quantum gates (Turchette *et al.*, 1995) and photonic switches (Harris and Yamamoto, 1998). Therefore, it was of interest to investigate the influence of the LG beam on higher order Zeeman coherences which will be discussed in this chapter. We compare the ellipticity dependent NMOR, obtained as a function of detuning using a Gaussian and LG beam as the probe optical field. This study enables us to determine the influence of the LG beam on higher order Zeeman coherences (with $\Delta m \geq \pm 2$) by extracting their contribution from the measured data.

4.2 Ellipticity dependent NMOR due to LG beam

4.2.1 Extraction of the HOC

As discussed in chapter 1 (**Section 1.5.4**), in the weak field approximation, the origin of NMOR

can be attributed to the nonlinear terms in the electromagnetic fields obtained by perturbative expansion of the electric susceptibility (Chen *et al.*, 1987; Chen *et al.*, 1990; Holmes and Griffith, 1995; Budker *et al.*, 2002). Using such an approximation, the origin of NMOR can be attributed to the formation of ground state coherences with $\Delta m = \pm 2$ by a two-photon process and thus can be described by Λ, V or X schemes (Chen *et al.*, 1990; Holmes and Griffith, 1995; Ståhlberg *et al.*, 1990). The interaction of the medium with elliptically polarized light renders it dichroic and birefringent, which results in the rotation of the elliptical polarization (**Section 1.5.4**).

It has been shown by Giraud-cotton *et al.* (1985) that in the absence of the magnetic field, the nonlinear susceptibility χ_l and χ_r (due to the left and the right circularly polarized light components) will be the same for linearly polarized light, as a result of which no magneto-optical activity will occur. But the presence of the elliptically polarized beam gives rise to a magnetic field independent term which results in an effect proportional to the difference in the intensity of the left and the right circularly polarized component (Giraud-Cotton *et al.*, 1985). This difference in the light intensity results in different light shifts of the magnetic Zeeman sublevels. In other words, the degeneracy of the magnetic Zeeman sublevels are lifted due to the ac Stark effect even in the absence of the magnetic field because of the interaction of the light with non-resonant atomic transitions (**Figure 4.1**). The resulting polarization rotation signal is known as the self-rotation signal and it was found to occur when there was large detuning in the laser beam frequency (Giraud-Cotton *et al.*, 1985; Rochester *et al.*, 2001; Novikova *et al.*, 2001; Novikova, 2003a).

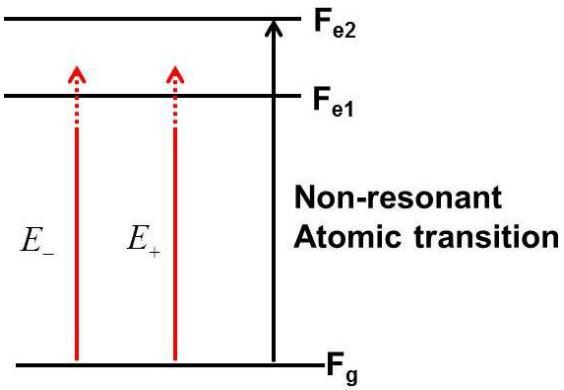

Figure 4.1: Energy level diagram to illustrate the self-rotation process.

It has been shown that the ac-Stark shift of the Zeeman sublevels is inversely proportional to the detuning from the corresponding non-resonant atomic hyperfine transition (Novikova *et al.*, 2000). Self-rotation φ_{SR} is given by (Novikova, 2003a)

$$\varphi_{SR} = 1/2\left(\varphi_{+} - \varphi_{-}\right) = g\varepsilon L, \tag{4.1}$$

where, g is the self-rotation coefficient, ε the ellipticity of the incident beam and L the length of the cell.

When the laser is detuned across the Doppler profile of a hyperfine structure transition, the contribution to the overall rotation of the elliptically polarized beam comes from the polarization rotation signal in the presence of the magnetic field and the self-rotation of elliptically polarized beam. Since self-rotation does not depend on the magnetic field, its effect can be eliminated by subtracting the self-rotation signal from the polarization rotation measurement in the presence of the magnetic field. The resulting difference comprises of the polarization rotation of a linearly polarized beam (nonlinear Faraday effect) and the rotation due to elliptically polarized beam.

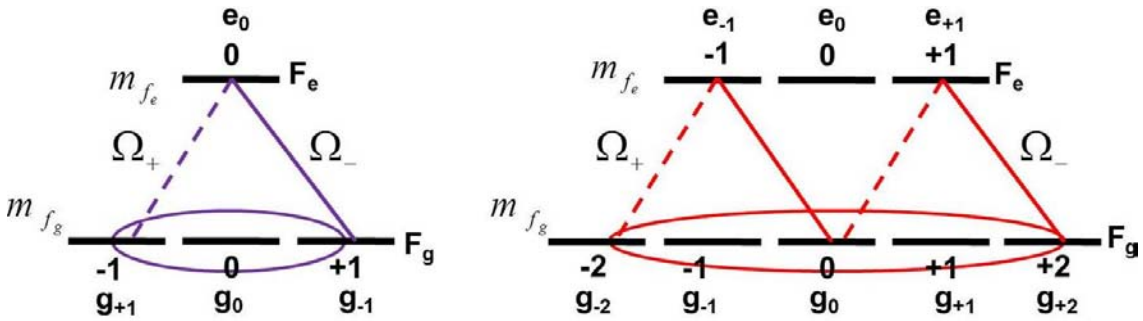

Figure 4.2: (a) Lambda (Λ) scheme and (b) *M* scheme.

Matsko *et al.* (2003) had used the transitions $F_g = 1 \rightarrow F_e' = 0$ and $F_g = 2 \rightarrow F_e' = 1$ to represent the Λ and *M* scheme highlighted in **Figure 4.2(a)** and **Figure 4.2 (b)** respectively. As shown in **Figure 4.2 (b)**, multi-photon processes are responsible for creating the ground-state higher order coherence (HOC) in a *M* scheme. Matsko *et al.* (2003) had showed that for the Λ scheme the rotation does not depend on the light ellipticity (4.2). On the other hand, for the *M* scheme, they

had shown that HOC with $\Delta m = \pm 4$ is responsible for creating a new type of polarization rotation which depends on both the light ellipticity and the applied magnetic field (Matsko *et al.*, 2003; Novikova, 2003a). The expression for the polarization rotation for a Λ scheme and *M* scheme is given by (Matsko *et al.*, 2003; Novikova, 2003a)

$$\varphi_{\Lambda} = \frac{2\omega_L}{\gamma} \ln\left(\frac{\mathrm{I}_{in}}{\mathrm{I}_{out}}\right) \tag{4.2}$$

$$\varphi_{M+\Lambda} = \frac{\omega_L}{\gamma}\left[1+2\frac{2+q^2}{\left(2-q^2\right)^2}\right]\ln\left(\frac{\mathrm{I}_{in}}{\mathrm{I}_{out}}\right), \tag{4.3}$$

where, ω_L denotes the Larmor frequency, γ gives the decoherence rate and q represents the ellipticity parameter. I_{in} and I_{out} are the intensities of the beam at the entrance and the exit of the vapor cell respectively.

$$\frac{\varphi_{M+\Lambda}}{\varphi_{\Lambda}} = \frac{1}{2}\left[1+2\frac{2+q^2}{\left(2-q^2\right)^2}\right]. \tag{4.4}$$

Matsko *et al.* (2003) had attributed the ellipticity dependent NMOR to the *M* scheme induced coherence. Since the HOC with $\Delta m = \pm 4$ becomes significant only for elliptically polarized beam, the influence of the LG beam profile on the HOC has been investigated by carrying out the ellipticity dependent polarization rotation measurements.

4.2.2 Experimental Details and discussions

The experimental set-up that was used to measure the polarization rotation signal is show in **Figure 4.3**. The LG beam (with OAM |*l*|= 1 and 3) was created using a CGH (He *et al.*, 1995). The probe beam was polarized along the *x*-axis and passed through Rb vapor cell with a natural mixture of the Rb isotopes (**Figure 4.3**). A solenoid was used to apply a longitudinal magnetic field (B_z) along the direction of propagation of the probe beam (Faraday geometry). A pair of Helmholtz coils was used to null the fields in the other two directions to ~ 0.3 mG. A QWP placed before the Rb vapor cell is used to control the ellipticity of the incident beam. Using the

balanced polarimetry arrangement [discussed in **Section 1.5.4** (**Figure 1.11 (b)**)], the rotation of the plane of polarization of the incident probe beam is obtained by measuring the differential signal between the two photodiodes.

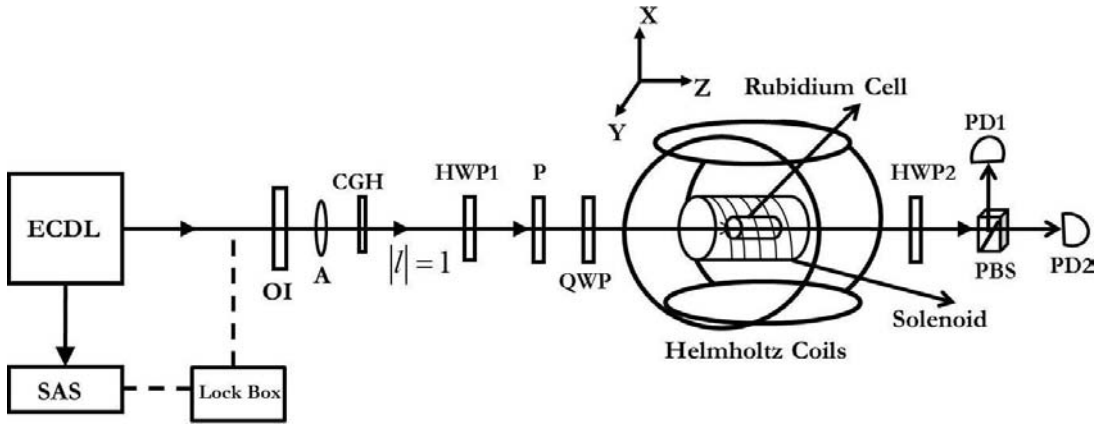

Figure 4.3: Experimental set-up used for measuring the NMOR with a LG beam of azimuthal mode index, $|l|$.

The ECDL was detuned across the transitions Rb^{85} ($F_g = 3 \rightarrow F_e'$), Rb^{85}($F_g = 2 \rightarrow F_e'$), Rb^{87}($F_g = 1 \rightarrow F_e'$), Rb^{87}($F_g = 2 \rightarrow F_e'$) (**Figure 4.11**). The polarization rotation measurements were carried out with the Gaussian and LG beam (OAM, $|l| = 1$ and 3) for ellipticity $\varepsilon = 0^\circ, 4^\circ, 10^\circ, 15^\circ, 20^\circ, 26^\circ, 35^\circ$ in the presence of a longitudinal magnetic field of 0.35 Gauss (**Figures 4.4, 4.6** and **4.7** respectively).

The sub-Doppler features that have been observed (highlighted by a star in **Figures 4.4, 4.5, 4.6, 4.8 and 4.10**) arise due to retro-reflections of the laser beam inside the atomic cell. Such features have also been reported by Matsko *et al.* (2003). These authors point out that the retro-reflected beam interacts with the atoms inside the cell and causes redistribution of atomic population similar to the one that is observed in the case of the Doppler-free saturation spectroscopy. Retro-reflections are quite difficult to remove and are present irrespective of the type of cell used. A similar observation has also been by Novikova (2003a). The sub-Doppler peak observed corresponds to the most intense 'Lamb-dips' observed in saturation spectroscopy (usually due to a cross-over resonance). 'Lamb-dips' appear at specific locations of an otherwise unchanged Doppler-broadened spectrum. The width of the polarization rotation signal is

comparable to the Doppler-broadened spectrum. Therefore, although the polarization rotation information is lost at the site of the sub-Doppler peak, it is safe to assume the rest of the signal is unaffected. Moreover these features do not change much between a Gaussian and a LG beam. In this study we focus on the evolution of the broad polarization rotation signal.

With increase in ellipticity the polarization rotation signals of the $Rb^{85}(F_g=2\rightarrow F_e')$ and $Rb^{87}(F_g=1\rightarrow F_e')$ transitions obtained with the LG beam (OAM, $|l|$ = 1 and 3) diminishes and flips from a downward peak to an asymmetric upward peak for $\varepsilon \geq 26^{\circ}$ and $\varepsilon \geq 35^{\circ}$ respectively (**Figures 4.4** and **4.6**). With the Gaussian beam, a similar trend is observed but the flipping appears to be incomplete (**Figure 4.5**) in the measured ellipticity range. A comparison between the measured polarization rotation signal for Gaussian and LG beam with $|l|$ =1 and 3 for $\varepsilon = 35^{\circ}$ is shown in **Figure 4.5(a)** and **(b)** respectively to illustrate this behavior. The flipping in the measured polarization rotation signal induced by the LG beam with $|l|$ =1 and 3 at $\varepsilon = 35^{\circ}$ appears to be more pronounced in the former case (**Figure 4.5**).

The ellipticity dependence is weaker for the transition $Rb^{87}(F_g=2\rightarrow F_e')$ in the presence of both Gaussian and LG beams and no change in curvature is observed (**Figure 4.7**). Similar behavior have been observed for the measured polarization rotation signal for the transitions $Rb^{85}(F_g=3\rightarrow F_e')$ (not shown).

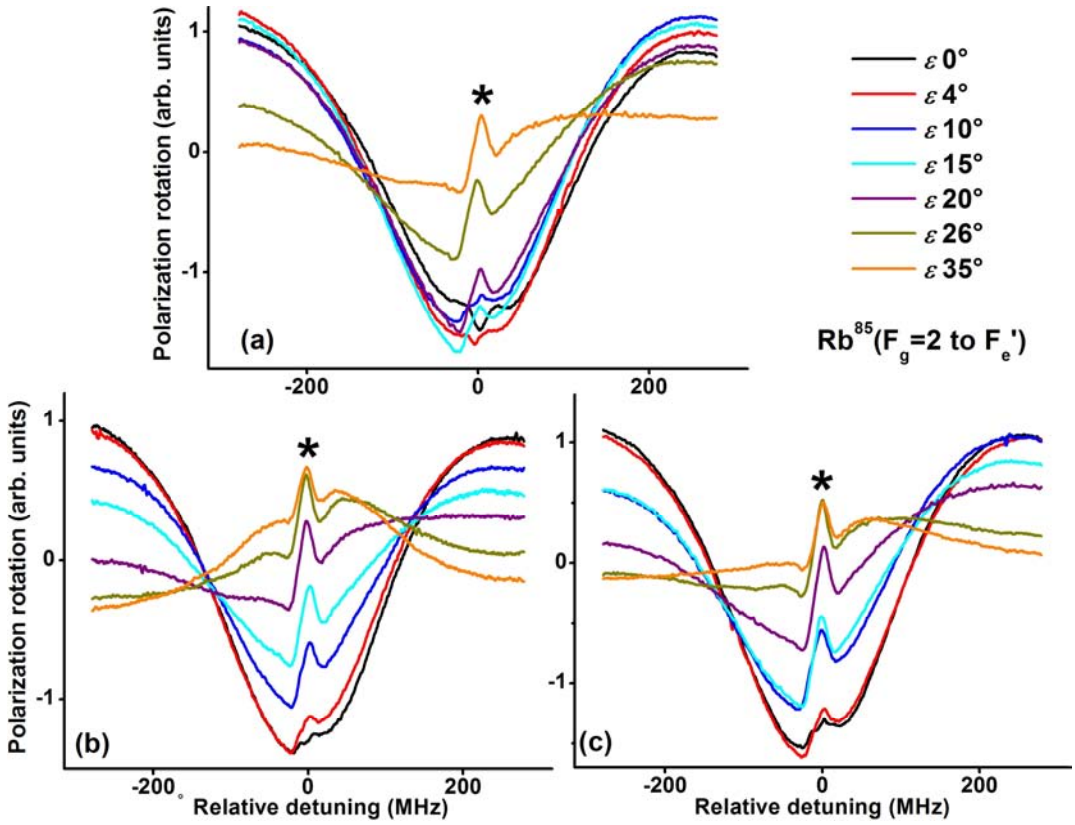

Figure 4.4: Measured polarization rotation signal for (a) Gaussian beam, (b) LG beam $|l| = 1$ and (c) $|l| = 3$ respectively for ellipticity $\varepsilon = 0^{\circ}, 4^{\circ}, 10^{\circ}, 15^{\circ}, 20^{\circ}, 26^{\circ}, 35^{\circ}$ when the laser is detuned across the transition $Rb^{85}(F_g=2 \rightarrow F_e')$. Internal sub-Doppler features are observed in the measured polarization rotation signal (highlighted by the star). Refer to text for details.

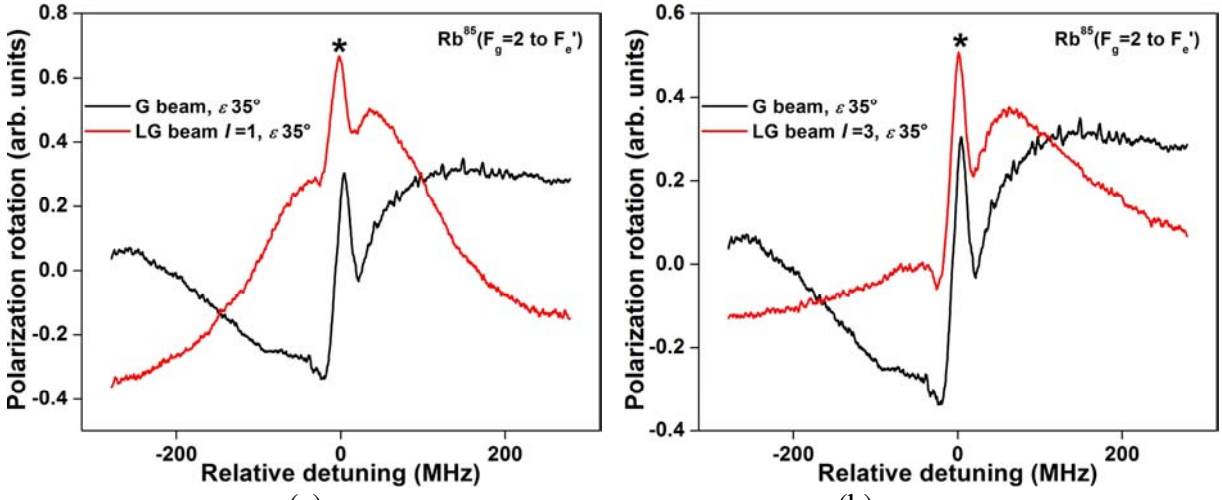

Figure 4.5: A comparison between the measured polarization rotation signal for (a) Gaussian and LG beam with $|l| = 1$ for $\varepsilon = 35^{\circ}$ and (b) Gaussian and LG beam with $|l| = 3$ for $\varepsilon = 35^{\circ}$ is shown.

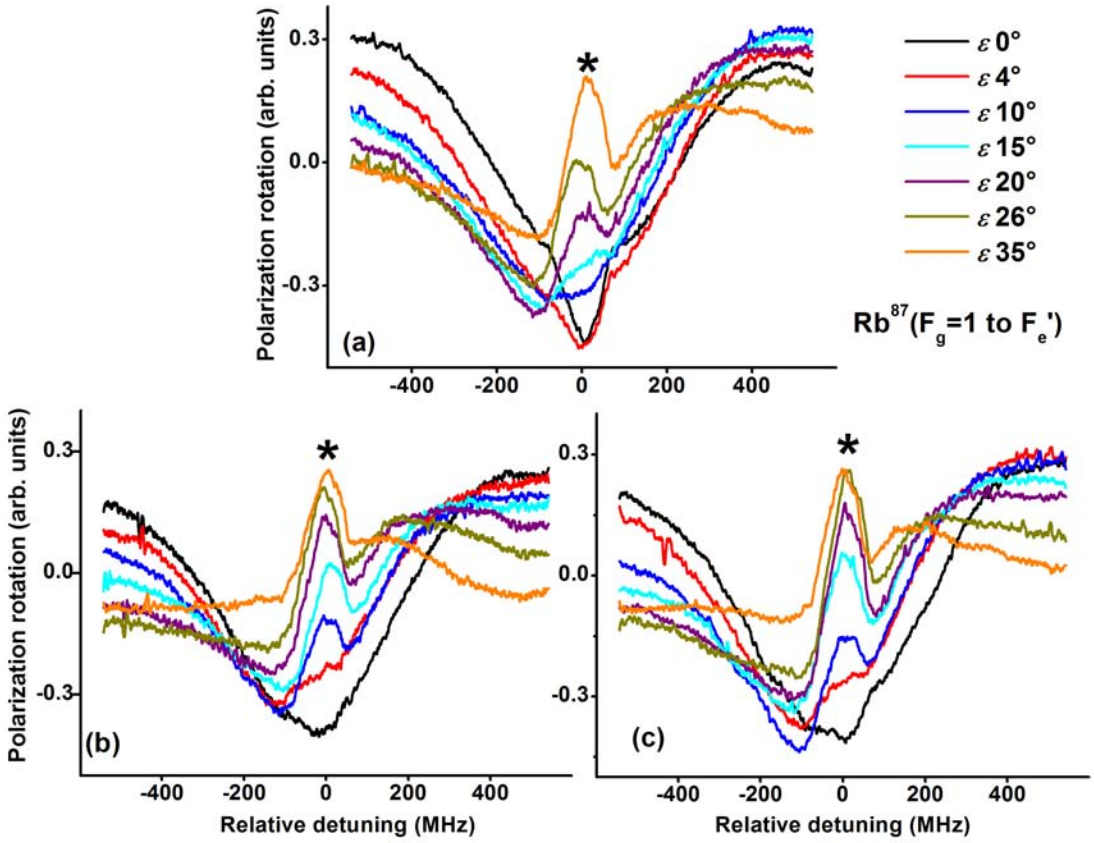

Figure 4.6: Measured polarization rotation signal for (a) Gaussian beam, (b) LG beam $|l| = 1$ and (c) $|l| = 3$ for ellipticity $\varepsilon = 0^{\circ}, 4^{\circ}, 10^{\circ}, 15^{\circ}, 20^{\circ}, 26^{\circ}, 35^{\circ}$ when the laser is detuned across the transition $Rb^{87}(F_g=1 \rightarrow F_e')$.

The LG beam is found to flip the curvature of the polarization rotation signal at a lower value of ellipticity in comparison to the Gaussian beam for the transitions $Rb^{85}(F_g=2 \rightarrow F_e')$ and $Rb^{87}(F_g=1 \rightarrow F_e')$. In order to further explore this behavior, the contributions to the higher order Zeeman coherences were extracted from the measured data.

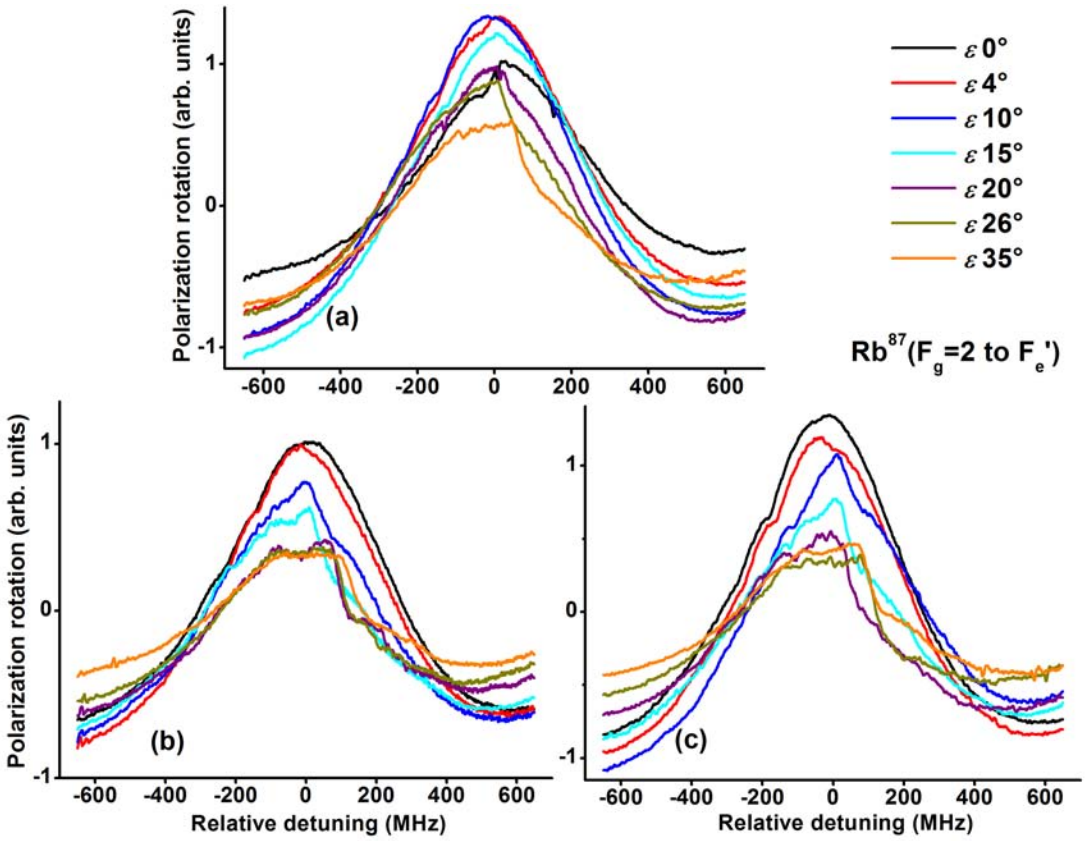

Figure 4.7: Measured polarization rotation signal for (a) Gaussian beam, (b) LG beam $|l|$ =1 and (c) $|l|$ =3 for ellipticity $\varepsilon = 0^{\circ}, 4^{\circ}, 10^{\circ}, 15^{\circ}, 20^{\circ}, 26^{\circ}, 35^{\circ}$ when the laser is detuned across the transition $Rb^{87}(F_g=2 \rightarrow F_e')$. A similar behavior is obtained for the transition $Rb^{85}(F_g=3 \rightarrow F_e')$ (not shown in this thesis).

To enable the extraction, the following measurements were carried out with the Gaussian and LG beams (OAM, $|l|$ = 1 and 3) maintained at the same intensity for the cases

(i) The polarization rotation signal of a linearly polarized beam ($\varepsilon = 0^{\circ}$) at B_z = 0.35 G,

(ii) The self-rotation signal of the elliptically polarized beam (ellipticity ε) in the absence of the magnetic field.

(iii) The rotation of plane of polarization of the elliptically polarized beam (ellipticity ε) at B_z = 0.35 G.

As discussed in the introduction, by removing the effect of polarization rotation due to linearly polarized beam and self-rotation of elliptically polarized beam from the polarization

rotation of elliptically polarized beam, one can extract the contributions to the HOC, i.e., by subtracting (i) and (ii) from (iii) [Novikova, (2003b)].

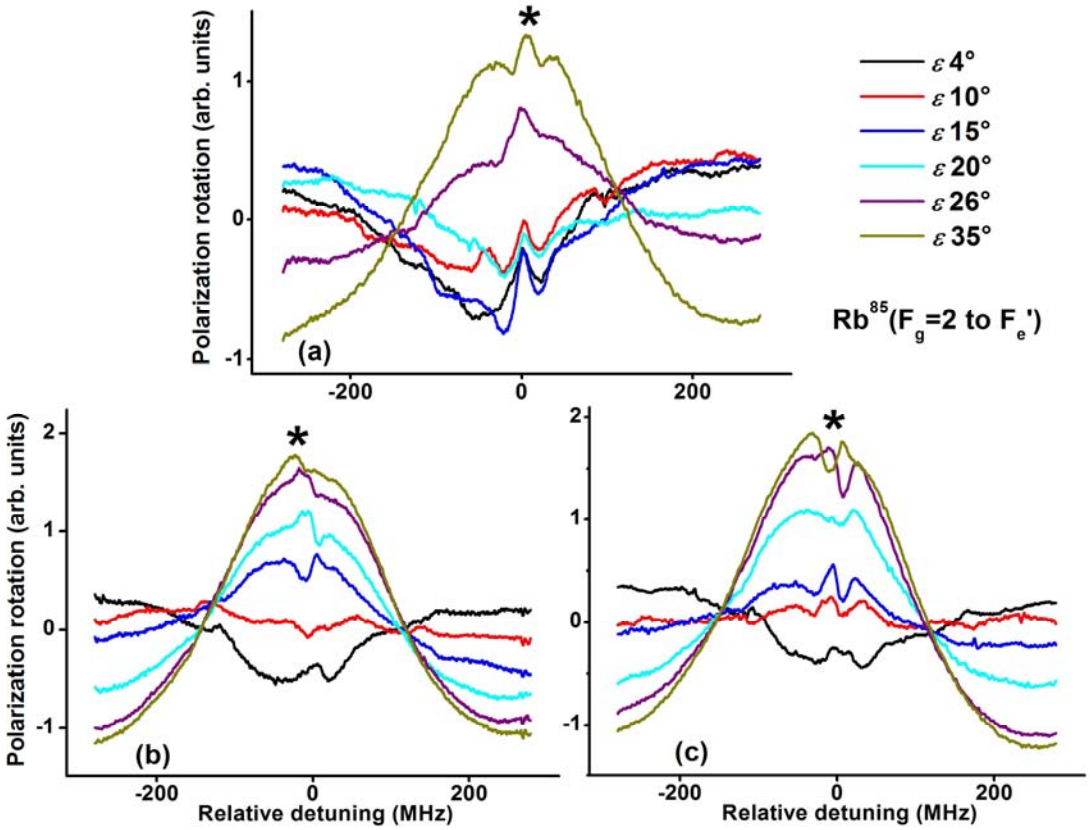

Figure 4.8: Contributions to the higher order coherences for (a) Gaussian beam, (b) LG beam $|l|$ =1 and (c) $|l|$ =3 for ellipticity ε = 4°, 10°, 15°, 20°, 26°, 35° when the laser is detuned across the transition $Rb^{85}(F_g=2\rightarrow F_e')$.

The contributions to the HOC due to Gaussian and LG beam (OAM, $|l|$ =1 and 3) for ellipticity ε = 4°, 10°, 15°, 20°, 26°, 35° for the transitions $Rb^{85}(F_g=2\rightarrow F_e')$, $Rb^{87}(F_g=2\rightarrow F_e')$ and Rb^{87} $(F_g=1\rightarrow F_e')$ as shown in **Figures 4.8, 4.9** and **4.10** respectively. With increase in ellipticity, the extracted HOC of the $Rb^{85}(F_g=2\rightarrow F_e')$ and $Rb^{87}(F_g=1\rightarrow F_e')$ transitions obtained with the LG beam (OAM, $|l|$ = 1 and 3) increases and flips from a downward peak to an upward peak for $\varepsilon \geq 15°$ and $\varepsilon \geq 35°$ respectively (**Figures 4.8** and **4.10**). This behavior is similar to the one observed for the polarization rotation signal (**Figures 4.4** and **4.6**). With the Gaussian beam a similar trend is observed for the transition $Rb^{85}(F_g=2\rightarrow F_e')$, but the flipping is found to occur at

higher ellipticity, $\varepsilon \geq 26^{\circ}$ [**Figure 4.8(a)**]. For the transition $Rb^{87}(F_g=1 \rightarrow F_e')$, no change in the curvature is observed in the presence of Gaussian beam with increase in ellipticity (**Figure 4.10**).

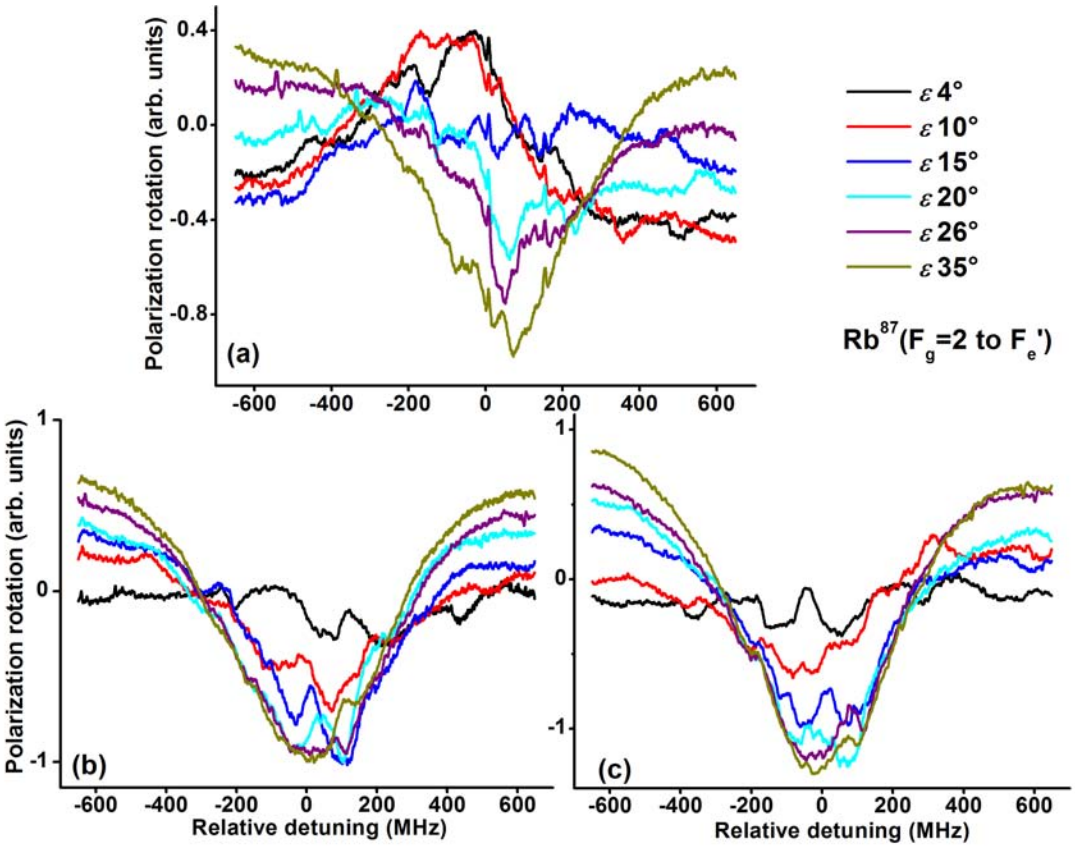

Figure 4.9: Contributions to the higher order coherences for (a) Gaussian beam, (b) LG beam $|l| = 1$ and (c) $|l| = 3$ for ellipticity $\varepsilon = 4^{\circ}, 10^{\circ}, 15^{\circ}, 20^{\circ}, 26^{\circ}, 35^{\circ}$ when the laser is detuned across the transition $Rb^{87}(F_g=2 \rightarrow F_e')$. A similar behavior is obtained for the transition $Rb^{85}(F_g=3 \rightarrow F_e')$, not shown in this thesis.

At $\varepsilon = 4^{\circ}$, the HOC extracted for transition $Rb^{87}(F_g=2 \rightarrow F_e')$ has upward and downward peaks for Gaussian and LG beams (OAM, $|l| = 1$ and 3) respectively (**Figure 4.9**). The curvature of the HOC is found to be ellipticity dependent for the Gaussian beam, flipping from an upward to downward peak with the increase in value of ellipticity (at $\varepsilon \geq 20^{\circ}$). No change in curvature is observed for LG beam with increase in ellipticity. A similar behavior has been observed for the extracted HOC for the transition $Rb^{85}(F_g=3 \rightarrow F_e')$ (not shown).

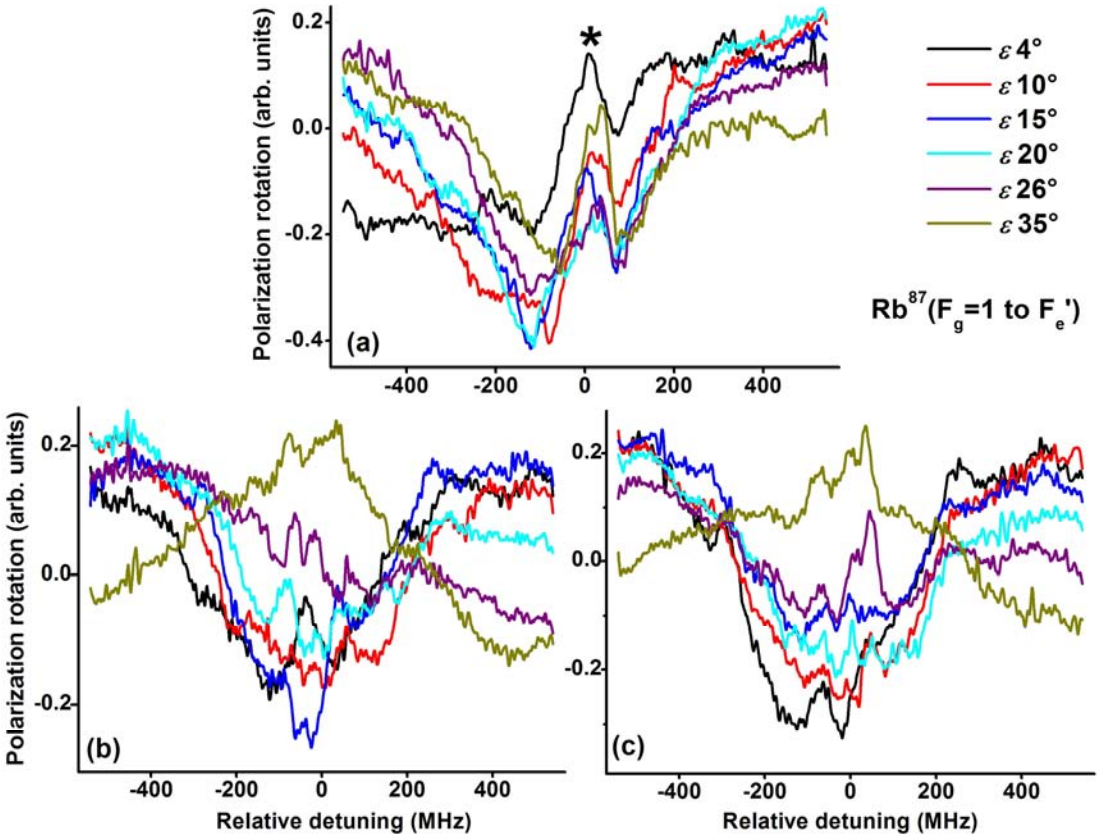

Figure 4.10: Contributions to the higher order coherences for (a) Gaussian beam, (b) LG beam $|l| = 1$ and (c) $|l| = 3$ for ellipticity $\varepsilon = 4^{\circ}, 10^{\circ}, 15^{\circ}, 20^{\circ}, 26^{\circ}, 35^{\circ}$ when the laser is detuned across the transition $Rb^{87}(F_g=1 \rightarrow F_e')$.

Summarizing, (i) The polarization rotation signal and the extracted HOC obtained with LG beam is found to be ellipticity dependent for the transitions $Rb^{85}(F_g=2 \rightarrow F_e')$ and $Rb^{87}(F_g=1 \rightarrow F_e')$, the curvature flipping with increase in the value of ellipticity. A similar trend is observed with Gaussian beam for the transition $Rb^{85}(F_g=2 \rightarrow F_e')$. The curvature of the extracted HOC due to the Gaussian beam is not found to flip for the transition $Rb^{87}(F_g=1 \rightarrow F_e')$. The curvature flip occurs consistently at a lower value of ellipticity for the LG beam than the Gaussian beam.

(ii) The ellipticity dependence of the measured polarization rotation signal and the extracted HOC is weaker for the transition $Rb^{87}(F_g=2 \rightarrow F_e')$ obtained with the LG beam, the curvature not changing with the increase in the value of ellipticity. A similar behavior is observed for the measured polarization rotation signal obtained with the Gaussian beam, but the extracted HOC is

found to be ellipticity dependent, its curvature flipping with the increase in the value of ellipticity.

From these results it is seen that the ellipticity dependent behavior of the polarization rotation signal and the extracted HOC depends on the beam profile (LG or Gaussian beam) and on the transitions studied.

4.3 Computational Analysis

The energy level diagram associated with Rb^{87} and Rb^{85} D_2 transition is shown in **Figure 4.11**. Three hyperfine transitions are associated with each of the Doppler broadened profiles of D_2 line - $Rb^{87}(F_g=1\rightarrow F_e')$, $Rb^{87}(F_g=2\rightarrow F_e')$, $Rb^{85}(F_g=2\rightarrow F_e')$ and $Rb^{85}(F_g=3\rightarrow F_e')$ (**Figure 4.11**). The polarization rotation signal was measured by detuning the probe beam over the Doppler broadened D_2 line. A computation of the polarization rotation signal taking into account all the hyperfine transitions and Doppler broadening is quite complicated. In addition, the spatial profile of the LG beam has to be taken into account. We found these complexities difficult to overcome and carried out a simpler computational analysis with degenerate two-level systems to illustrate the LG field's influence on Zeeman coherences.

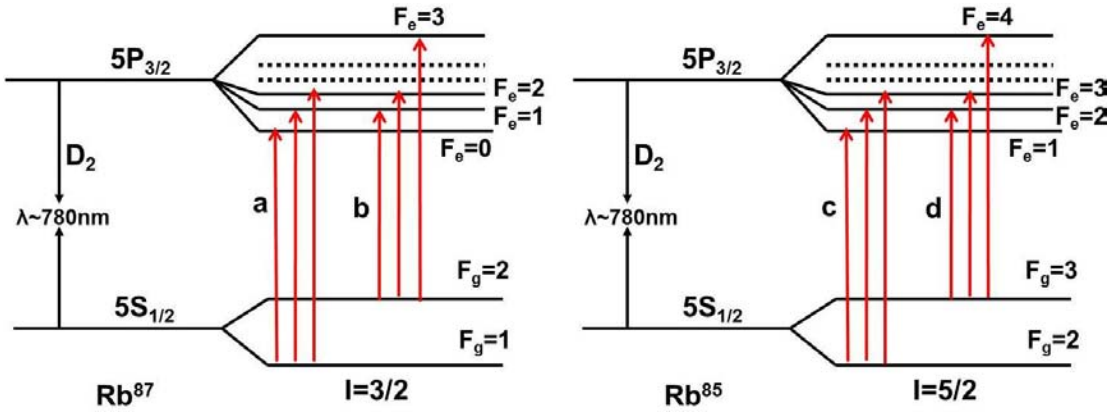

Figure 4.11: Energy level diagram for the transitions (a) $Rb^{87}(F_g=1\rightarrow F_e')$, (b) $Rb^{87}(F_g=2\rightarrow F_e')$, (c) $Rb^{85}(F_g=2\rightarrow F_e')$ and (d) $Rb^{85}(F_g=3\rightarrow F_e')$.

To choose the two - level systems, the relative hyperfine transition strengths ($S_{FF_e'}$) (Steck, 2010) were considered (**Table 4.1**). The $S_{FF_e'}$ provides the measure of the relative strength of each of the $F_g \rightarrow F_e'$ hyperfine transitions and the dominant transition in each of the Doppler profile was assumed to be representative of the entire profile.

$$S_{FF_e'} = \left(2F_e' + 1\right)(2J_g + 1)\begin{Bmatrix} J_g & J_e & 1 \\ F_e' & F_g & I \end{Bmatrix}^2, \tag{4.5}$$

where, I is the total nuclear angular momentum, J_g and J_e represents the total angular momentum quantum number of the ground and the excited states, respectively and the term in curly bracket is the Clebsch - Gordon coefficient. $S_{FF_e'}$ is independent of the particular ground state sublevel chosen and obeys the sum rule (Steck, 2010),

$$\sum_{F_e'} S_{FF_e'} = 1. \tag{4.6}$$

The chosen two - level systems either exhibit EIT or EIA. The systems are either closed (no loss of population) or open (some population is lost to the other hyperfine ground states). It can be seen [**Table 4.1** (Steck, 2010)] that for the Doppler profiles $Rb^{87}(F_g=2\rightarrow F_e')$ and $Rb^{85}(F_g=3\rightarrow F_e')$, the pure transitions $Rb^{87}(F_g=2\rightarrow 3)$ and $Rb^{85}(F_g=3\rightarrow 4)$ respectively are found to have the maximum relative hyperfine transition strength. These two transitions form closed EIA systems and hence can be best described by $J_g = 1 \rightarrow J_e = 2$, which is the simplest EIA system (Lezama *et al.*, 1999; Renzoni *et al.*, 2001). For the Doppler profile $Rb^{85}(F_g=2\rightarrow F_e')$, the relative hyperfine transition strength is almost same for all transitions $Rb^{85}(F_g=2\rightarrow 2)$, $Rb^{85}(F_g=2\rightarrow 1)$ and $Rb^{85}(F_g=2\rightarrow 3)$ (**Table 4.1**). While the former two transitions form open and closed EIT systems respectively, the latter one forms an open EIA system. In this case we assume the Doppler profile can be represented by an EIT system and choose $J_g = 1 \rightarrow J_e = 1$(to represent an open EIT system) and $J_g = 2 \rightarrow J_e = 1$ (to represent closed EIT system) for the computation (Renzoni *et al.*, 1997).

For the Doppler profile $Rb^{87}(F_g=1\rightarrow F_e')$, the two transitions, $Rb^{87}(F_g=1\rightarrow 2)$ and $Rb^{87}(F_g=1\rightarrow 1)$ have the same relative hyperfine transition strength (**Table 4.1**). The former transition is an open EIA system and the latter an open EIT system. In this case no clear cut choice of a two - level system is possible. Also, the extracted HOC with the Gaussian beam does not change its curvature (**Figure 4.10**) unlike the HOC extracted for $Rb^{85}(F_g=2\rightarrow F_e')$ and $Rb^{87}(F_g=2\rightarrow F_e')$ [**Figure 4.8** and **4.9**]. Therefore, no specific conclusions could be drawn in this case.

Table 4.1: The relative hyperfine transition strength for all the hyperfine transitions (Steck, 2010).

Doppler profile	Pure transitions	Relative Hyperfine transition strength	The computational system that has been chosen
$Rb^{87}(F_g=2\rightarrow F_e')$	$Rb^{87}(F_g=2\rightarrow 3)$	$7/10 \approx 0.7$	$Rb^{87}(F_g=2\rightarrow 3)$ – closed transition, EIA system. Two level system, $J_g = 1 \rightarrow J_e = 2$ chosen as the representative of the entire profile.
	$Rb^{87}(F_g=2\rightarrow 2)$	$1/4 \approx 0.25$	
	$Rb^{87}(F_g=2\rightarrow 1)$	$1/20 \approx 0.05$	
$Rb^{85}(F_g=3\rightarrow F_e')$	$Rb^{85}(F_g=3\rightarrow 4)$	$9/14 \approx 0.643$	$Rb^{85}(F_g=3\rightarrow 4)$ – closed transition, EIA system. Two level system, $J_g = 1 \rightarrow J_e = 2$ chosen as the representative of the entire profile.
	$Rb^{85}(F_g=3\rightarrow 3)$	$5/18 \approx 0.278$	
	$Rb^{85}(F_g=3\rightarrow 2)$	$5/63 \approx 0.079$	
$Rb^{85}(F_g=2\rightarrow F_e')$	$Rb^{85}(F_g=2\rightarrow 3)$	$14/45 \approx 0.311$	$Rb^{85}(F_g=2\rightarrow 2)$ and $Rb^{85}(F_g=2\rightarrow 1)$ – open and closed transitions respectively, EIT system. Two level systems, $J_g = 1 \rightarrow J_e = 1$ and $J_g = 2 \rightarrow J_e = 1$ chosen as the representative of the entire profile.
	$Rb^{85}(F_g=2\rightarrow 2)$	$7/18 \approx 0.389$	
	$Rb^{85}(F_g=2\rightarrow 1)$	$3/10 \approx 0.3$	
$Rb^{87}(F_g=1\rightarrow F_e')$	$Rb^{87}(F_g=1\rightarrow 2)$	$5/12 \approx 0.417$	$Rb^{87}(F_g=1\rightarrow 2)$ transition – open EIA system and $Rb^{87}(F_g=1\rightarrow 1)$ transition – open EIT system. No clear cut choice of two level system is possible.
	$Rb^{87}(F_g=1\rightarrow 1)$	$5/12 \approx 0.417$	
	$Rb^{87}(F_g=1\rightarrow 0)$	$1/6 \approx 0.166$	

4.4 Computational results

The two-level atomic systems $J_g = 1 \rightarrow J_e = 1$, $J_g = 2 \rightarrow J_e = 1$ and $J_g = 1 \rightarrow J_e = 2$ that were chosen to represent the EIT and the EIA systems are shown in the **Figure 4.12**.

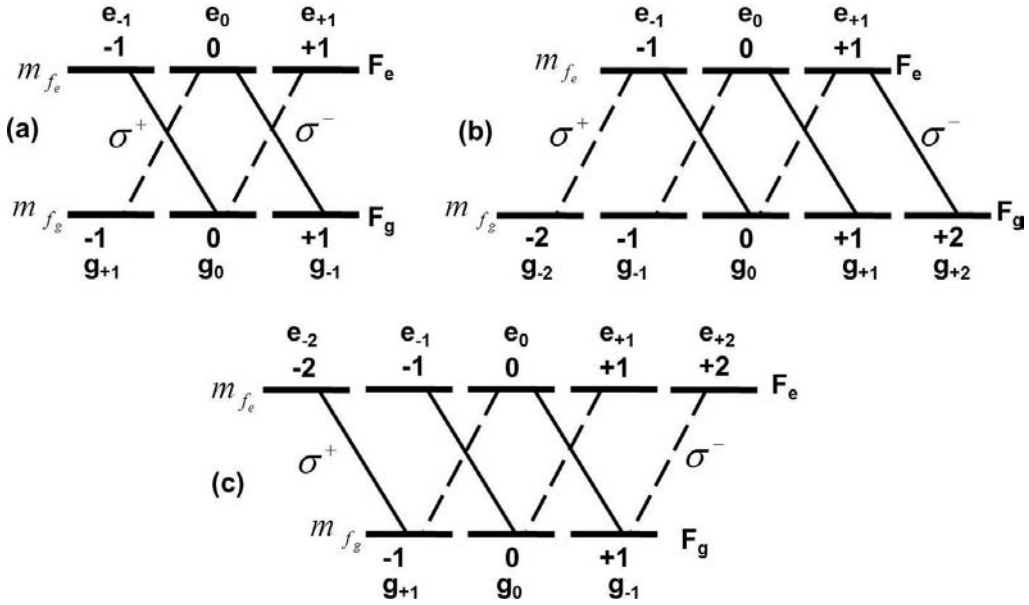

Figure 4.12: Atomic level diagram for the transitions (a) $J_g = 1 \rightarrow J_e = 1$, (b) $J_g = 2 \rightarrow J_e = 1$ and (c) $J_g = 1 \rightarrow J_e = 2$.

As discussed in **Section 2.2**, the unperturbed Hamiltonian H_o and the magnetic interaction energy H_B are given by (2.3) and (2.4). Expression for the atom-field interaction Hamiltonian H_I is given by

$$H_I = \sum_{\substack{i,j \\ i \neq j}} |i\rangle\langle j| \left\{ \left(d_{ij}E\right)_{\sigma+} + \left(d_{ij}E\right)_{\sigma-} \right\} + h.c, \tag{4.7}$$

where, *h.c* is the Hermitian conjugate of the first term in (4.7). The quantization axis was chosen along the magnetic field direction. The electric field vector associated with the probe beam propagating along the *z* direction and polarized in the *x* direction is given by

$$\vec{E} = E_o \cos\left(\omega_{pr} t\right)\ \hat{e}_x \tag{4.8}$$

$$\hat{e} = \hat{e}_x \cos\varepsilon + i \sin\varepsilon = -\hat{e}_{+1} \cos\left(\varepsilon - \pi/4\right) + i \sin\left(\varepsilon - \pi/4\right), \tag{4.9}$$

where, ω_{pr} is the frequency of the probe beam and $\hat{e}_x$ is unit polarization vector, $\hat{e}_{\pm} = \mp(\hat{e}_x + \hat{e}_y)/\sqrt{2}$ are its cyclic basis vectors and $\varepsilon = -\frac{\pi}{4} \le \varepsilon \le +\frac{\pi}{4}$, the ellipticity of the probe field (Brazhnikov *et al.*, 2005; Brazhnikov *et al.*, 2006).

The optical Bloch equations obtained for the two-level atomic system are numerically solved under the steady state conditions (Rochester, 2008). The polarization rotation angle per unit length, φ for the atomic transition $J_g = 1 \rightarrow J_e = 2$ is given by (Malakyan *et al.*, 2004)

$$\varphi = \sum_{\substack{i,j \\ i \neq j}} \frac{\Pi_0 \lambda^2}{16\pi\ \Omega} \sec(2\varepsilon) \left\{ \left(\cos\varepsilon + \sin\varepsilon\right) \mathrm{Re}[\rho_{e_i g_j}{}^{-}] + \left(\cos\varepsilon - \sin\varepsilon\right) \mathrm{Re}[\rho_{e_i g_j}{}^{+}] \right\}. \quad \textbf{(4.10)}$$

For a closed $J_g \rightarrow J_e$ transition it was shown that (Sobelman, 1992)

$$\Pi_0 = \frac{4\nu_o{}^3}{3c^2} \frac{1}{2J_e + 1} \left\langle \alpha_e J_e \| \ r \ \| \alpha_g J_g \right\rangle^2, \quad \textbf{(4.11)}$$

where, $\rho_{e_i g_j}{}^{+}$ and $\rho_{e_i g_j}{}^{-}$ represents the optical transitions satisfying the selection rule $\Delta m = \pm 1$ respectively. The angled bracket in (4.11) represents the reduced matrix element which is defined in (2.7) and ν_o is the frequency difference between the ground and the excited states in the absence of the magnetic field. To compute the polarization rotation angle for the LG beam, Ω in (4.10) is replaced by Ω_{LG} (with Ω^o_{LG} treated as a constant). A double integration has to be carried out over parameters r and ϕ. As the dimension of the density matrix increases (more than 4×4), the computational analysis with a double integration becomes intractable. Therefore the integration was carried out over r, varying it from 0 to w_o [ignoring the z dependence as in (2.1)], and ϕ was set to 0 as it has been found that the rotation signal is unchanged for all values of ϕ (0 to 2π). The expression for polarization rotation angle per unit length with a LG field is given by

$$\varphi_{LG} = \int_{r=0}^{w_o} \sum_{\substack{i,j \\ i \neq j}} \frac{\Pi_0 \lambda^2 \sec(2\varepsilon) \left\{ \left(\cos\varepsilon + \sin\varepsilon\right) \mathrm{Re}[\rho_{e_i g_j}{}^{-}] + \left(\cos\varepsilon - \sin\varepsilon\right) \mathrm{Re}[\rho_{e_i g_j}{}^{+}] \right\}}{16\pi\ \Omega^o_{LG} \left(\frac{r}{w_o}\right)^{|l|} e^{-\frac{r^2}{w_o{}^2}}} r dr. \quad \textbf{(4.12)}$$

The polarization rotation was computed as a function of one-photon detuning. However no flipping was observed in the curvature for both the EIT and the EIA systems (figure not shown). Therefore the polarization rotation and HOC were analyzed in terms of openness of the transition and for this purpose these observables were studied as a function of branching ratio, b_2.

In order to investigate the influence of the Gaussian and LG beam profiles on the HOC, as discussed in the previous chapter (**Section 3.3.2**), the repopulation matrix Λ_Γ (3.16) is rewritten such that the individual contributions to the TOC channel from the excited state coherences can be separated out in the computation (Ram *et al.*, 2009). Here *A* given by (3.17) in the third chapter is a 3×3 matrix (for the transitions $J_g = 1 \rightarrow J_e = 1$ and $J_g = 1 \rightarrow J_e = 2$) and 5×5 matrix (for the transition $J_g = 2 \rightarrow J_e = 1$).

The normalized excited state - HOC, ρ_{e-1e+1} (with $\Delta m = \pm 2$) was calculated as a function of the branching ratio, b_2 (varying it from 1 to 0) with Gaussian and LG fields at $\varepsilon = 0^\circ$ and 35° for the two-level atomic systems $J_g = 1 \rightarrow J_e = 2$, $J_g = 2 \rightarrow J_e = 1$ and $J_g = 1 \rightarrow J_e = 1$ respectively. The branching ratio components $b_0 \& b_1$ are set as 1. The OAM associated with the LG beam is taken as $|l| = 1$ with $\Gamma/\gamma = 20$, $\Gamma/\Omega_G = \Gamma/\Omega_{LG}^o = 1$, Δ=1, $\omega_L = 0.35$ MHz and $w_o = 3$mm. No difference was observed between results computed for $|l| = 1$ and $|l| = 3$ (not shown).

The calculated HOC, ρ_{e-1e+1} as a function of b_2, is found to change with an increase in the value of ellipticity in the presence of the Gaussian beam for the EIA system (transition $J_g = 1 \rightarrow J_e = 2$) [**Figure 4.13 (a) - (i)** and **(iii)**]. No such ellipticity dependent behaviour is seen for the LG beam [**Figure 4.13 (a) - (ii)** and **(iv)**] in this case. No significant difference can be seen in the behaviour of HOC, ρ_{e-1e+1} with increase in ellipticity in the presence of both Gaussian and LG beams for the EIT system (transitions $J_g = 1 \rightarrow J_e = 1$ and $J_g = 2 \rightarrow J_e = 1$) when b_2 is varied it from 1 to 0 [**Figure 4.13 (b)**].

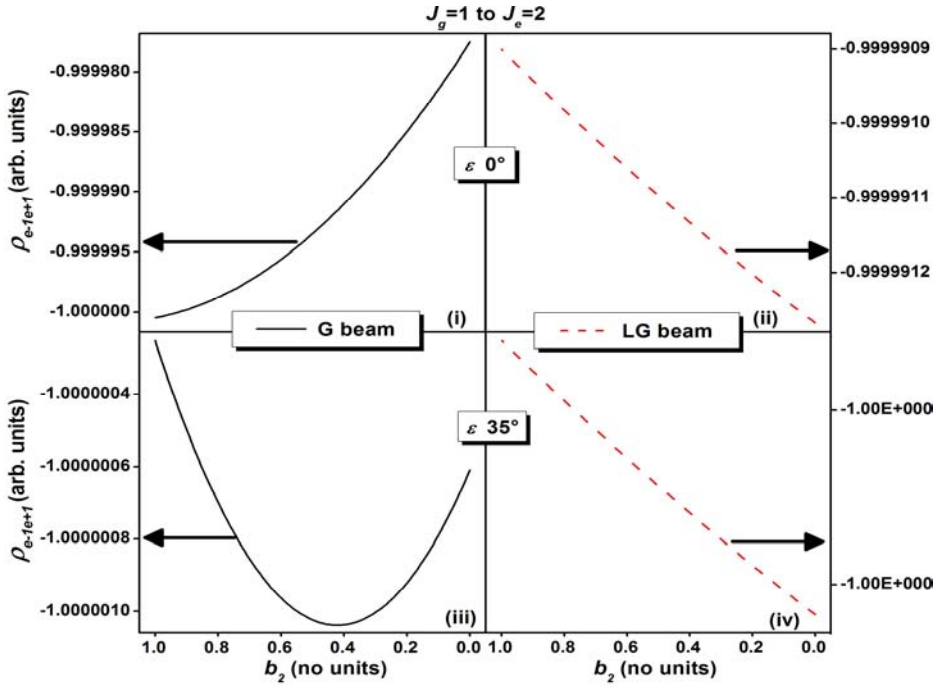

(a)

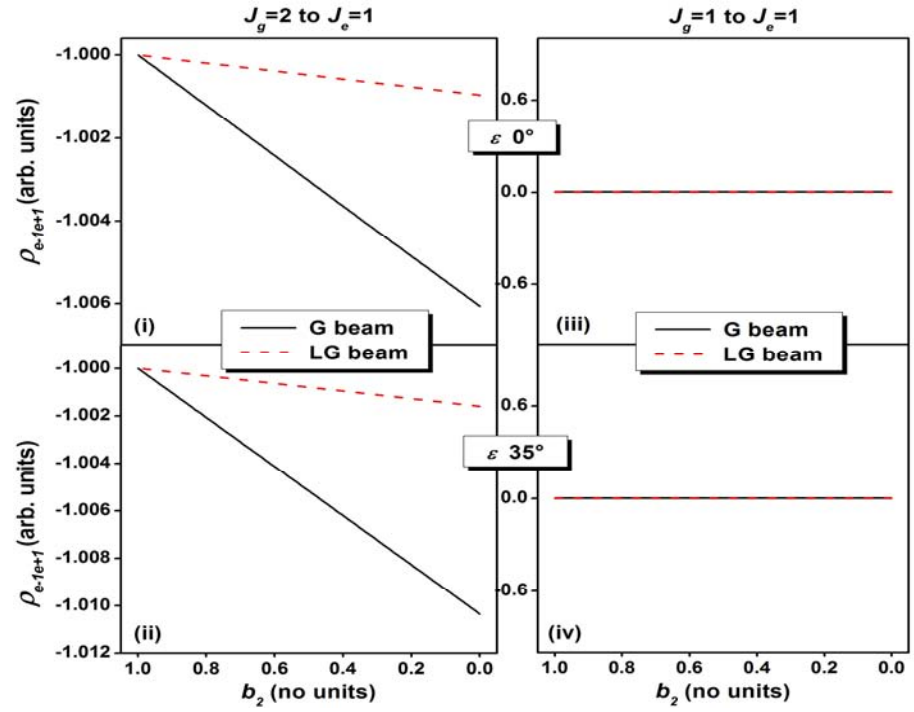

(b)

Figure 4.13: Calculated excited state - HOC, ρ_{e-1e+1} for (a) transition $J_g = 1 \rightarrow J_e = 2$ with (i), (iii) Gaussian beam and (ii), (iv) LG beam at ε=0° and 35° respectively (b) Panels (i),(ii) and (iii), (iv) transitions $J_g = 2 \rightarrow J_e = 1$ and $J_g = 1 \rightarrow J_e = 1$ respectively at ε =0° and 35°, using $\Gamma/\gamma = 20$, $\Gamma/\Omega_G = \Gamma/\Omega_{LG}^o = 1$, Δ=1, $\omega_L = 0.35$ MHz, $|l| = 1$ and $w_o = 3$mm.

From these results it can be inferred that when the TOC process ($\Delta m = \pm 2$ coherence) is varied by varying b_2, the evolution of excited state Zeeman coherence ρ_{e-1e+1} with ellipticity is found to depend on the beam profile for the EIA system unlike the EIT system.

This plot could be better understood by plotting $\left\{\rho_{e-1e+1}\big|_{\mathrm{LG}} - \rho_{e-1e+1}\big|_{\mathrm{G}}\right\}_{b_i=1}$ as a function of ellipticity with $b_i = 1$(closed system) and all other parameters remaining the same as used in **Figure 4.13**. The difference in the magnitude of excited state - HOC, ρ_{e-1e+1} (with $\Delta m = \pm 2$) was calculated between LG and Gaussian beams and plotted as a function of ellipticity for the transitions $J_g = 1 \rightarrow J_e = 1$, $J_g = 2 \rightarrow J_e = 1$ and $J_g = 1 \rightarrow J_e = 2$ (**Figure 4.14**).

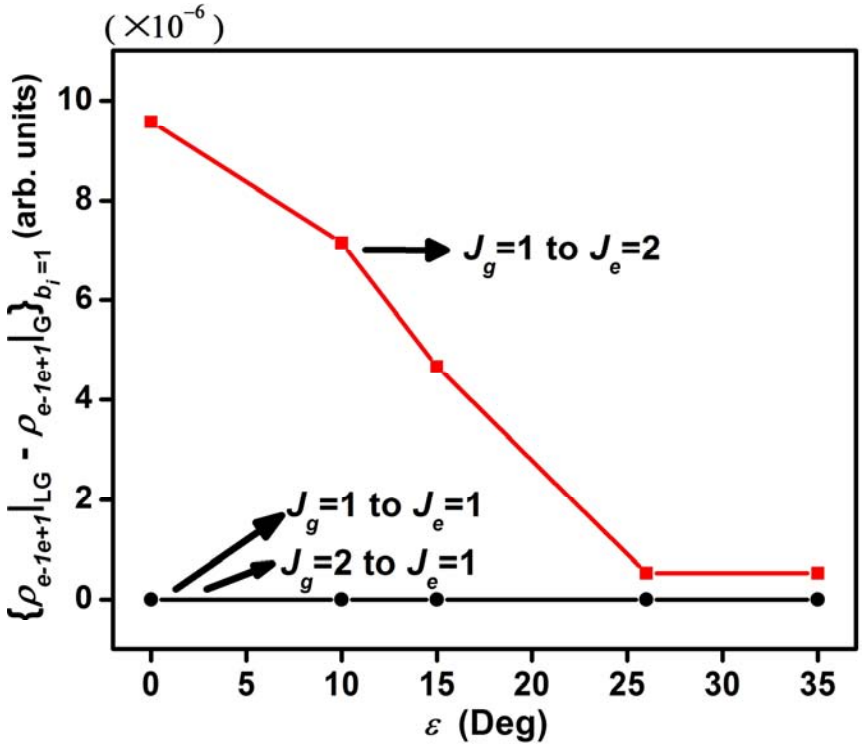

Figure 4.14: The difference in the magnitude of HOC, ρ_{e-1e+1} between LG and Gaussian beams plotted as a function of ellipticity for the transitions $J_g = 1 \rightarrow J_e = 2$, $J_g = 2 \rightarrow J_e = 1$ and $J_g = 1 \rightarrow J_e = 1$. The branching ratio components, b_i is set as 1. All the other parameters are the same as those used in **Figure 4.13**.

It is seen that $\left\{\rho_{e-1e+1}\big|_{\mathrm{LG}} - \rho_{e-1e+1}\big|_{\mathrm{G}}\right\}_{b_i=1}$ is distinctly different for the EIA system, decreasing with increase in ellipticity. This suggests that for the EIA systems, the ellipticity

dependence of the Zeeman coherence, ρ_{e-1e+1} depends on the spatial profile of the probe optical field. A corresponding observation can also be made from the experimental data: The ellipticity dependence of the extracted HOC contribution for $Rb^{87}(F_g=2\rightarrow F_e')$ also depends on the spatial profile of the probe optical field, changing curvature with ellipticity only for a Gaussian beam [**Figure 4.9 (a)**].

For the EIT system, $\left\{\rho_{e-1e+1}\big|_{\mathrm{LG}} - \rho_{e-1e+1}\big|_{\mathrm{G}}\right\}_{b_i=1}$ is zero for all values of ellipticity. A corresponding observation can again be made from experiment. The extracted HOC contribution for $Rb^{85}(F_g=2\rightarrow F_e')$ evolve with ellipticity in similar fashion for both LG and Gaussian beams, although the curvature is found to flip at different values of ellipticity for both the beam profiles (**Figure 4.8**).

The difference between EIT and EIA systems subject to Gaussian and LG fields can also be seen by plotting the difference in the polarization rotation signal (φ) in the presence and in the absence of the TOC process involving $\Delta m = \pm 2$ coherence - $(\varphi)_{b_2(1)} - (\varphi)_{b_2(0)}$ as a function of ellipticity (ε) (**Figure 4.15**). There is not much difference in the ellipticity dependence of $(\varphi)_{b_2(1)} - (\varphi)_{b_2(0)}$ between Gaussian and LG fields for the EIT transition [**Figure 4.15 (ii)** and **(iii)**]. However, a distinct difference is observed in the case of the EIA transition [**Figure 4.15 (i)**]. This suggests that the TOC process which is crucial to the observation of EIA depends on the spatial profile of the incident optical field.

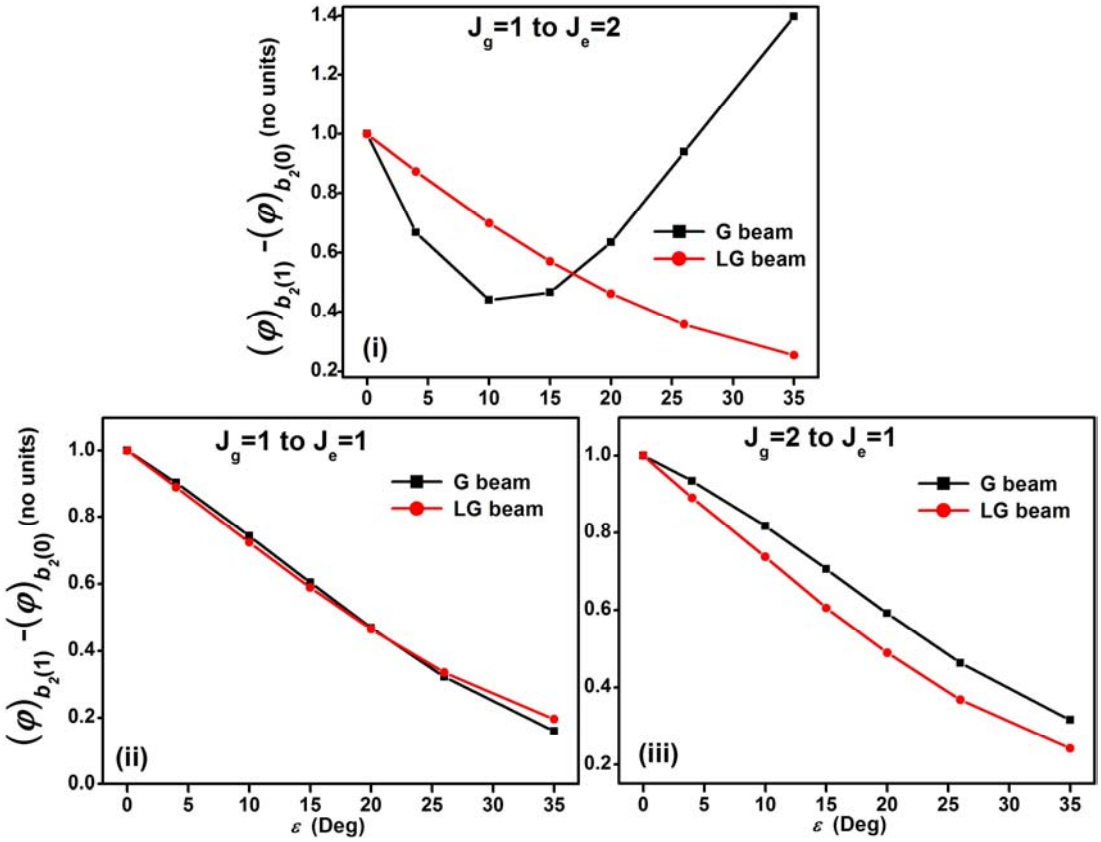

Figure 4.15: Difference in the calculated polarization rotation signal at $b_2(1)$ and $b_2(0)$ as a function of ellipticity (ε) for Gaussian and LG beams (i) $J_g = 1 \rightarrow J_e = 2$, (ii) $J_g = 1 \rightarrow J_e = 1$ and (iii) $J_g = 2 \rightarrow J_e = 1$ transitions respectively. All the other parameters are the same as those used in **Figure 4.13**.

In a standard density matrix computation, Hanle EIA resonances transform to EIT resonances when b_2 is set to zero, i.e., by removing the TOC contribution from $\Delta m = \pm 2$ coherences (Ram *et al.*, 2009). When the Hanle EIA (b_2=1) and EIT (b_2 =0) resonance amplitudes are plotted as a function of ellipticity [**Figure 4.16(b)**], it is clear that the effect of suppression of TOC with a Gaussian field is much more prominent than with a LG field. The associated Hanle profiles for $J_g = 1 \rightarrow J_e = 2$ for $\varepsilon = 0^\circ$, 15° and 35° are shown in **Figure 4.16(a)**. The OAM associated with the LG beam is taken as $|l| = 1$ with $\Gamma/\gamma = 1000$, $\Gamma/\Omega_G = \Gamma/\Omega_{LG}^o = 5$, Δ=0, $b_0 = b_1 = 1$ and $w_o = 3\text{mm}$. This again suggests that the TOC process involving $\Delta m = \pm 2$ coherences depend on the spatial profile of the incident optical field.

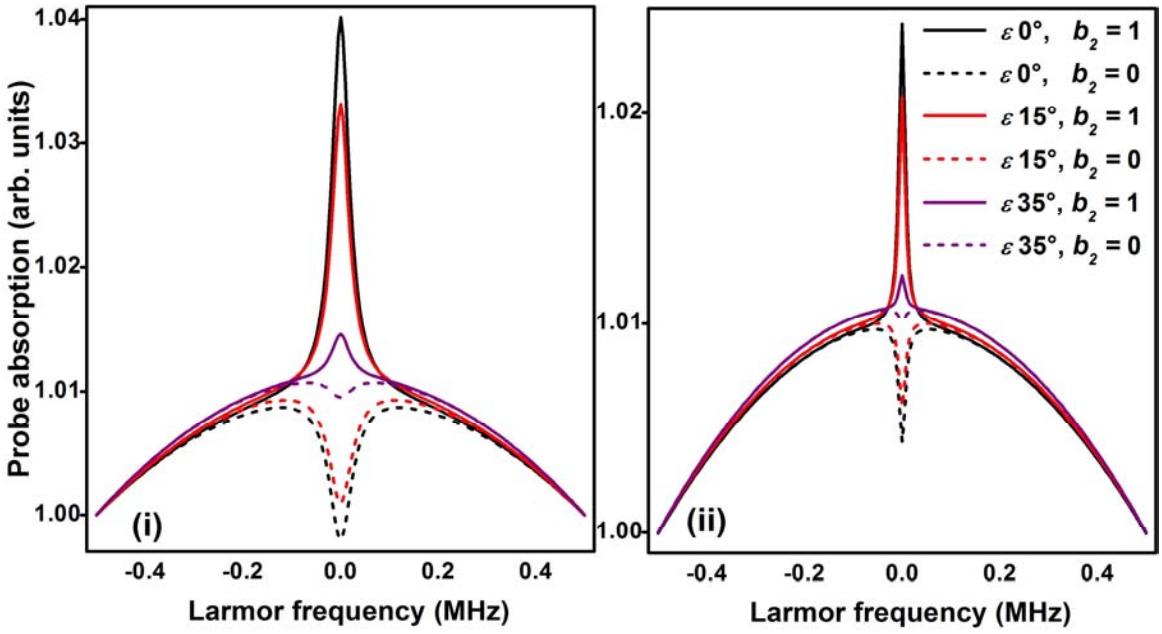

(a)

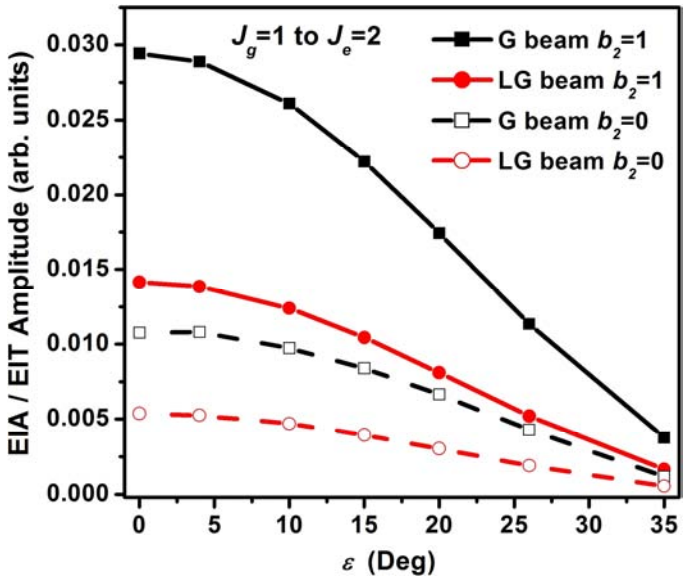

(b)

Figure 4.16: (a) The calculated Hanle resonance for the transition $J_g = 1 \rightarrow J_e = 2$ with (i) Gaussian and (ii) LG fields for ellipticity $\varepsilon = 0^\circ$, 15° and 35° in the presence and in the absence of TOC with $\Delta m = \pm 2$ coherences by turning on or off b_2,(b) Computed EIA / EIT amplitude as a function of ellipticity for the transition $J_g = 1 \rightarrow J_e = 2$ with Gaussian and LG fields, using $\Gamma / \gamma = 1000$, $\Gamma / \Omega_G = \Gamma / \Omega_{LG}^o = 5$, $\Delta = 0, b_0 = b_1 = 1$, $|l| = 1$ and $w_o = 3\text{mm}$.

4.5 Conclusions

In summary, we have studied the ellipticity dependence of polarization rotation signals for the D_2 line of Rb atoms with Gaussian and LG probe fields. This study enables us to determine the influence of the LG beam on higher order Zeeman coherences by extracting their contribution from the measured data. Results were analyzed computationally by choosing a degenerate two - level EIT or EIA system, representative of the entire Doppler profile. We find that the extracted HOC contribution for $Rb^{87}(F_g=2\rightarrow F_e')$ (treated computationally with an EIA system) changes curvature with ellipticity only for a Gaussian beam while for $Rb^{85}(F_g=2\rightarrow F_e')$ (treated computationally with an EIT system), a change in curvature is observed for both the optical fields at different values of ellipticity. Correspondingly, it is shown that when the TOC process involving $\Delta m = \pm 2$ coherence is varied, the ellipticity dependence of the excited state Zeeman coherence ρ_{e-1e+1} was found to depend on the spatial profile of the probe optical field for an EIA system but not for EIT system. It is also shown that for the EIA system, there is a distinct difference in the way the Gaussian and LG fields influences the TOC process involving $\Delta m = \pm 2$ coherence.

CHAPTER 5

Summary and conclusions

5.1 Summary of research work

This thesis focuses on the interaction of the Rubidium (Rb) atoms with a coherent Laguerre-Gaussian (LG) optical field with spatially varying phase factor and mode amplitude. Detailed computational and experimental studies have been carried out to understand the effect of the LG field on Zeeman coherence induced phenomena like electromagnetically induced transparency (EIT), electromagnetically induced absorption (EIA) and nonlinear magneto-optical rotation (NMOR). EIT and EIA resonances obtained in Hanle configuration are significantly narrower with a LG field compared to a Gaussian field. This suggests that optical fields with non-zero orbital angular momentum (OAM) produce long-lived Zeeman coherences. The narrowing is observed only for atomic transit time limited resonances and not for spin-exchange collision limited resonances. Thus the spatial profile of the LG field influences resonance line shapes only if the relaxation time is dependent on spatial coordinates as in transit time relaxation. The influence of the LG field on higher order Zeeman coherences (with $\Delta m \geq \pm 2$) has been investigated by extracting their contribution from ellipticity dependent polarization measurements as a function of laser detuning. This study shows that EIA systems (driven by excited state coherences) couple differently with the LG field compared to EIT systems (driven by ground state coherences).

A detailed list of summary and conclusions is presented below.

- The LG beam profile brings about a significant narrowing in the line shape of the Hanle resonance in comparison to a Gaussian beam. We have shown by computation and

experiment that this narrowing and hence long lived Zeeman coherences can be attributed to the non-zero azimuthal mode index of the LG field. LG field induced narrowing of EIT/EIA profiles may have several important applications such as atomic clocks, slow light etc.

- NMOR due to the transit effect (NMOR-I) and the coherence effect (NMOR-II) have been measured for the LG beam. LG beam brings about a narrower NMOR-I profile in comparison to the Gaussian beam. There is no significant change in the line-widths of the NMOR-II between the Gaussian and LG beam profiles. Unlike the transit effect NMOR, the induced atomic coherence persists even if the atom leaves the laser beam. Therefore the presence of OAM in the optical field does not influence the line-width in this case.

- The nonlinear magneto-optical rotation response of the $F_g=2 \rightarrow F_e' = 3$ transition of Rb^{87} with magnetic field applied parallel (Faraday geometry) and perpendicular (Voigt geometry) to the probe field (Gaussian or LG) direction was studied. The extent of narrowing induced by the LG beam, when compared with the Gaussian beam, was found to be more in the case of the Voigt geometry.

- It was shown that the influence of the LG field depends on the nature of the Zeeman coherences created ($\Delta m = \pm 1$ or $\Delta m = \pm 2$ in this case) which could account for the difference in extent of narrowing observed for nonlinear Faraday and Voigt rotation signals subject to Gaussian and LG fields. Thus it is seen that the influence of the LG field on the Zeeman coherence lifetime is polarization dependent.

- The ellipticity dependence of polarization rotation signals has been studied for the D_2 line of Rb atoms with Gaussian and LG probe fields system and the contributions to the Zeeman coherences have been extracted from the measured data. Results were analyzed computationally by choosing a degenerate two - level EIT or EIA system, representative of the entire Doppler profile.

- The polarization rotation signal and the extracted HOC obtained with LG beam is found to be ellipticity dependent for the transitions $Rb^{85}(F_g=2 \rightarrow F_e')$ (treated computationally with an EIT system), the curvature flipping with increase in the value of ellipticity. While a similar trend is observed with Gaussian beam, the curvature flip occurs

consistently at a lower value of ellipticity for the LG beam than the Gaussian beam.

- The ellipticity dependence of the measured polarization rotation signal and the extracted HOC is weaker for the transition $Rb^{87}(F_g=2\rightarrow F_e')$ (treated computationally with an EIA system) obtained with the LG beam, the curvature not changing with the increase in the value of ellipticity. A similar behavior is observed for the measured polarization rotation signal obtained with the Gaussian beam, but the extracted HOC is found to be ellipticity dependent, its curvature flipping with the increase in the value of ellipticity.
- It was shown that when the strength of the TOC process ($\Delta m = \pm 2$ coherence) is varied, the ellipticity dependence of the excited state Zeeman coherence ρ_{e-1e+1} was found to depend on the spatial profile of the probe optical field for an EIA system but not for EIT system.
- It was also shown that for the EIA system there is a distinct difference in the way the Gaussian and LG fields influences the TOC process involving $\Delta m = \pm 2$ coherence.

5.2 Future outlook of research work

- The presence of buffer gas in a vapour cell results in the atoms diffusing through the laser beam thus increasing the Zeeman coherence lifetime. It would be of interest to verify the effect of the LG beam profile on the Zeeman coherence lifetime and on the nature of the higher order coherences that are created in the presence of a buffer gas.
- It has been shown that, for the EIA system, while manipulating the TOC contribution from $\Delta m = \pm 2$ coherences (by switching 'on' or 'off' the branching ratio component b_2), the effect of suppression of the TOC ($\Delta m = \pm 2$) is more prominent with a Gaussian beam in comparison to the LG beam. This observation needs to be explored experimentally by investigating the influence of the LG field on the TOC process for open and closed EIA system.
- EIT has been computationally studied for a lambda system using LG beam and it has been predicted that LG field brings about a steeper dispersion in comparison to the

Gaussian beam. It was also shown computationally that the LG beam profile reduces the group velocity of the light pulse in comparison to a Gaussian beam. It would be interest to verify these predictions by carrying out EIT measurements with a LG beam either for a lambda like system or for a degenerate two-level system

- It would also be of interest to carry out slow light measurements with LG field. This study will enable us to verify if the storage time, the time delay and the spatial compression is enhanced by replacing the Gaussian beam with the LG field as predicted in this study.

REFERENCES

1. **Akulshin, A. M., S. Barreiro and A. Lezama** (1998). Electromagnetically induced absorption and transparency due to resonant two-field excitation of quasidegenerate levels in Rb vapor. *Phys. Rev. A* **57** 2996.

2. **Alexandrov, E. B., M. V. Balabas, A. S. Pasgalev, A. K. Vershovskii and N. N. Yakobson** (1996). Double-Resonance Atomic Magnetometers: from Gas Discharge to Laser Pumping. *Laser Phys.* **6**, 244.

3. **Allen, L., M. W. Beijersbergen, R. J. C. Spreeuw and J. P. Woerdman** (1992). Orbital angular momentum of light and the transformation of Laguerre-Gaussian laser modes. *Phys. Rev A* **45**, 8185.

4. **Allen, L., M. Babiker and W.L. Power** (1994). Azimuthal Doppler shift in light beams with orbital angular momentum. *Opt. Commun.* **112**, 141.

5. **Allen, L., M. Babiker, W. K. Lai and V. E. Lembessis** (1996). Atom dynamics in multiple Laguerre-Gaussian beams. *Phys. Rev A* **54**, 4259.

6. **Allen, L., A. M. Barnett and M. L. Padgett** (2003). *Optical angular momentum*. IOP publishing limited.

7. **Alnis, J. and M. Auzinsh** (2001). Reverse dark resonance in Rb excited by a diode laser. *J. Phys. B: At. Mol. Opt. Phys.* **34**, 3889.

8. **Andrews, D. L.** (2008). *Structured Light and Its Applications*: *An Introduction to Phase-Structured Beams and Nano-scale Optical Forces*. Elsevier Inc.

9. **Arimondo, E. (**1996). *Progress in Optics*, edited by E. Wolf (Elsevier, Amsterdam), Vol. XXXV, p. 257.

10. **Arlt, J., K. Dholakia, L. Allen and M. J. Padgett** (1998). The production of multiringed Laguerre−Gaussian modes by computer-generated holograms. *J. Mod. Opt.* **45**, 1231.

11. **Arlt, J., R. Kuhn and K. Dholakia** (2001). Spatial transformation of Laguerre-Gaussian laser modes. *J. Mod. Opt.* **48**, 783.

12. **Barkov L. M., D. A. Melik-Pachayev and M. S. Zolotorev** (1989) Nonlinear Faraday rotation in samarium vapor. *Opt. Commun.* **70** 467.

13. **Barreiro, S. and J. W. R. Tabosa** (2003). Generation of Light Carrying Orbital Angular Momentum via Induced Coherence Grating in cold atoms. *Phys. Rev. Lett.* **90**, 133001.

14. **Barreiro, S., J. W. Tabosa, H. Failache and A. Lezama** (2006). Spectroscopic Observation of the Rotational Doppler Effect. *Phys. Rev. Lett.* **97**, 113601.

15. **Basistiy, I. V., V. V. Slyusar, M. S. Soskin, M. V. Vasnetsov and A. Ya. Bekshaev** (2003) Manifestation of the rotational Doppler effect by use of an off-axis optical vortex beam. *Opt. Lett.* **28**, 1185.

16. **Bazhenov, V. Y., M.V. Vasnetsov and M.S. Soskin** (1990). Laser beams with screw dislocations in their wavefronts. *JETP Lett.* **52**, 429.

17. **Boyd, R. W.** (2003). *Nonlinear Optics* 2nd ed., Academic, San Diego.

18. **Bransden, B. H. and C. J. Joachain** (2004). *Physics of atoms and molecules,* Pearson Education, 2nd ed.

19. **Brazhnikov, D. V., A. M. Tumaikin, V. I. Yudin and A. V. Taichenachev** (2005). Electromagnetically induced absorption and transparency in magneto-optical resonances in an elliptically polarized field. *J. Opt. Soc. Am. B* **22**, 57.

20. **Brazhnikov, D. D., A. V. Taichenachev, A. M. Tumaikin, V. I. Yudin, S. A Zibrov, Ya. O. Dudin, V. V. Vasil'ev and V. L. Velichansky** (2006). Features of Magneto-Optical Resonances in an Elliptically Polarized Traveling Light Wave. *JETP Lett* **83,** 64.

21. **Budker, D., V. V. Yashchuk and M. Zolotorev** (1998). Nonlinear Magneto-optic Effects with Ultra-narrow Widths. *Phys. Rev. Lett.* **81**, 5788.

22. **Budker, D., D. F. Kimball, S. M. Rochester, V. V. Yashchuk and M. Zolotorev** (2000). Sensitive magnetometry based on nonlinear magneto-optical rotation. *Phys. Rev. A*, **62**, 043403.

23. **Budker, D., W. Gawlik, D. F. Kimball and S. M. Rochester** (2002). Resonant nonlinear magneto-optical effects in atoms. *Rev. Mod. Phys.* **74** 1153.

24. **Budker, D., D. F. Kimball and D. P. DeMille** (2004). *Atomic Physics* Oxford University Press.

25. **Chen, X., V. L. Telegdi and A. Weis** (1987). Magneto-optical rotation near the caesium D2 line(Macaluso-Corbino effect) in intermediate fields: I. Linear regime. *J. Phys. B* **20**, 5653.

26. **Chen, X., V. L. Telegdi and A. Weis** (1990). Quantitative study of the nonlinear Macaluso-Corbiino (resonant Faraday) effect in Cs. *Opt. Commun.* **74**, 301.

27. **Corney, A.** (1977). *Atomic and Laser Spectroscopy*. Oxford University Press, Oxford.

28. **Courtial, J., K. Dholakia, L. Allen and M. J. Padgett** (1997). Second-harmonic generation and the conservation of orbital angular momentum with high-order Laguerre-Gaussian modes. *Phys. Rev. A* **56**, 4193.

29. **Dancheva, Y., G. Alzetta, S. Cartaleva, M. Taslakov and Ch. Andreeva** (2000). Coherent effects on the Zeeman sublevels of hyperfine states in optical pumping of Rb by monomode diode laser. *Opt. Commun.***178**, 103.

30. **Dimitrijević, J., A. Krmpot, M. Mijailović, D. Arsenović, B. Panić, Z. Grujić and B. M. Jelenković** (2008). Role of transverse magnetic fields in electromagnetically induced absorption for elliptically polarized light. *Phys. Rev. A* **77**, 013814.

31. **Drake, K. H., W. Lange and J. Mlynek** (1988). Nonlinear Faraday and Voigt effect in a J=1 to J′=0 transition in atomic samarium vapor. *Opt. Commun.***66**, 315.

32. **Ducloy, M., M. P. Gorza and B. Decomps** (1973). Higher-order nonlinear effects in a gas laser: Creation and detection of an hexadecapole moment in the neon $2p_4$ level. *Opt. Commun.* **8**, 21.

33. **Dutton, Z. and J. Ruostekoski** (2004). Transfer and Storage of Vortex States in Light and Matter Waves. *Phys. Rev. Lett.* **93**, 193602.

34. **Faraday, M.** (1855). *Experimental Research* Taylor and Francis, London, Vol. III, p. 2164.

35. **Fleischhauer, M. and M. D. Lukin** (2000). Dark-State Polaritons in Electromagnetically Induced Transparency. *Phys. Rev. Lett.* **84**, 5094.

36. **Fleischhauer, M. and M. D. Lukin** (2002). Quantum memory for photons: Dark-state Polaritons. *Phys. Rev. A* **65**, 022314.

37. **Fleischhauer, M., A. Imamoglu and J. P. Marangos** (2005). Electromagnetically induced tranparency: optics in coherent media. *Rev. Mod. Phys.* **77** 633.

38. **Friese, M. E. J., J. Enger, H. Rubinsztein-Dunlop and N. R. Heckenberg** (1996). Optical angular-momentum transfer to trapped absorbing particles. *Phys. Rev. A* **54,** 1593.

39. **Gawlik, W.** (1994). Modern Nonlinear Optics, Advances in Chemical Physics Series, vol 85. John Wiley and Sons, Inc.

40. **Gerry, C. and P. Night** (2005). *Introductory Quantum optics* Cambridge University Press, Cambridge, England.

41. **Giraud-Cotton, S., V. P. Kaftandjian and L. Klein** (1985). Magnetic optical activity in intense laser fields. I. Self-rotation and Verdet constant. *Phys. Rev. A* **32**, 2211.

42. **Goodman, J. W.** (1968). *Introduction to Fourier Optics*, McGraw-Hill Book Co., New York, N.Y.

43. **Goren, C., A. D. Wilson-Gordon, M. Rosenbluh and H. Friedmann** (2003). Electromagnetically induced absorption due to transfer of coherence and to transfer of population. *Phys. Rev. A* **67**, 033807.

44. **Hamid. R., M. Celik, E. Sahin and A. Ch. Izmailov** (2006). Sub-Doppler absorption resonances of ring-shaped laser beams in a thin vapor cell *Laser Phys.* **16**, 1621.

45. **Hänsch, T. W., I. S. Shahin and A. L. Schawlow** (1971). High-Resolution Saturation Spectroscopy of the Sodium D Lines with a Pulsed Tunable Dye Laser. *Phys. Rev. Lett.* **27**, 707.

46. **Harper, W.** (1972). Optical pumping. *Rev. Mod. Phys.* **44,** 169.

47. **Harper, W. and A. C. Tam** (1977). Effect of rapid spin exchange on the magnetic-resonance spectrum of alkali vapors. *Phys. Rev. A*, **16**, 1877.

48. **Harris, S. E., J. E. Field and A. Imamoğlu** (1990). Nonlinear optical processes using electromagnetically induced transparency. *Phys. Rev. Lett*. 64, 1107.

49. **Harris, S. E., J. E. Field and A. Kasapi** (1992). Dispersive properties of electromagnetically induced transparency. *Phys. Rev. A* **46**, R29.

50. **Harris, M., C.A. Hill, P. R. Tapster and J. M. Vaughan** (1994). Laser modes with helical wave-fronts. *Phys. Rev. A* **49**, 3119.

51. **Harris, S.E.** (1997). Electromagnetically Induced Transparency. *Phys. Today* **50**, 36.

52. **Harris, S. E. and Y. Yamamoto** (1998). Photon Switching by Quantum Interference. *Phys. Rev. Lett.* **81**, 3611.

53. **Harris, S. E. and L. V. Hau** (1999). Nonlinear Optics at Low Light Levels. *Phys. Rev. Lett.* **82**, 4611.

54. **Harris, S.E.** (2000). Ponder motive Forces with Slow Light. *Phys. Rev. Lett.* **85**, 4032.

55. **Hau, L. V., S. E. Harris, Z. Dutton and C. H. Behroozi** (1999). Light speed reduction to 17 metres per second in an ultracold atomic gas. *Nature (London)* **397**, 594.

56. **He, H., N. R. Heckenberg and H. Rubinsztein- Dunlop** (1995). Optical Particle Trapping with Higher-order Doughnut Beams Produced Using High Efficiency Computer Generated Holograms. *J. mod. Optics***. 42,** 217.

57. **Holmes, B. W. and J. A. R. Griffith** (1995). A detailed study of the effects of weak magnetic fields on the forward scattering of resonant laser light by sodium vapour. *J. Phys. B* **28**, 2829.

58. **Hovde, C., B. Patton, E. Corsini, J. Higbie and D. Budker** (2010). Sensitive optical atomic magnetometer based on nonlinear magneto-optical rotation. *Proc. SPIE* 7693, 769313.

59. **Huard, S.** (1997). *Polarization of Light*, Wiley, New York.

60. **Kotlyar, V. V., S. N. Khonina, A. A. Kovalev, V. A. Soifer, H. Elfstrom and J. Turunen** (2006). Diffraction of a plane, finite-radius wave by a spiral phase plate. *Opt. Lett.* **31**, 1597.

61. **Lam, J. F. and R. L. Abrams** (1982). Theory of nonlinear optical coherences in resonant degenerate four-wave mixing *Phys. Rev. A* **26**, 1539.

62. **Ledbetter, M. P., I. M. Savukov, V. M. Acosta and D. Budker** (2008). Spin-exchange-relaxation-free magnetometry with Cs vapor. *Phys. Rev. A* **77**, 033408.

63. **Lembessis, V. E.** (1999). A mobile atom in a Laguerre–Gaussian laser beam, *Optics Comm.* **159**, 243.

64. **Lezama, A., S. Barreiro and A. M. Akulshin** (1999). Electromagnetically induced absorption. *Phys. Rev. A* **59**, 4732.

65. **Lezama, A., G. C. Cardoso and J. W. R. Tabosa** (2000). Polarization dependence of four-wave mixing in a degenerate two-level system. *Phys. Rev. A* **63**, 013805.

66. **Lighthill, M. J.** (1965). Group velocity, *IMA journal of Applied Mathematics* **1**, 1.

67. **Liu, Ch., Z. Dutton, C. H. Behroozi and L. V. Hau** (2001). Observation of coherent optical information storage in an atomic medium using halted light pulse. *Nature (London)* **409**, 490.

68. **Łobodziński, B. and W. Gawlik** (1996). Multipole moments and trap states in forward scattering of resonance light. *Phys. Rev. A* **54**, 2238.

69. **Loudon, R.** (1983). *The Quantum Theory of Light* Oxford University Press 2nd Ed.

70. **Lukin, M. D., S. F. Yelin and M. Fleischhauer** (2000). Entanglement of Atomic Ensembles by Trapping Correlated Photon States.

71. **Lukin, M. D. and A. Imamoglu** (2001). Controlling photons using electromagnetically induced transparency. Nature, **413**, 273.

72. **MacAdam, K. B., A. Steinbach and C. Wieman** (1992). A narrow-band tunable diode laser system with grating feedback, and a saturated absorption spectrometer for Cs and Rb. *Am. J. Phys.* **60**, 1098.

73. **Macaluso, D. and O. M. Corbino** (1898). *C.R. Hebd Seances Acad. Sci*., **127**, 548.

74. **Marangos, J. P.** (1998). Tropical review of electromagnetically induced transparency *J. Mod. Opt.* **45**, 471-503.

75. **Marcuse, D.** (1982). *Light transmission optics* 2nd ed., Van Nostrand Reinhold electrical/ computer science and engineering series.

76. **Malakyan, Yu. P., S. M. Rochester, D. Budker, D. F. Kimball and V. V. Yashchuk** (2004). Nonlinear magneto-optical rotation of frequency modulated light resonant with a low-J transition. *Phys. Rev. A* **69** 013817.

77. **Matsko, A. B., I. Novikova, M. S. Zubairy and G. R. Welch** (2003). Nonlinear magneto-optical rotation of elliptically polarized light. *Phys. Rev. A* **67**, 043805.

78. **McLeant, R. J., R. J. Ballagh and D. M. Warrington** (1985). Population trapping in the neon $2p_3$ to $1s_4$ transition. *J. Phys. B: At. Mol. Phys.* ***18,*** 2371.

79. **Nienhuis, G. and F. Schuller** (1998). Magneto-optical effects of saturating light for arbitrary field direction. *Opt. Commun.* **151**, 40.

80. **Nishina, Y. and B. Lax** (1969). Interband Faraday rotation and Voigt effecr in Ge. *J. Phys. Chem. Solids* **30**, 739.

81. **Novikova, I., A. B. Matsko, V. A. Sautenkov, V. L. Velichansky, M. O. Scully and G. R. Welch** (2000). Ac-Stark shifts in the nonlinear Faraday effect. *Opt. Lett.* **25**, 1651.

82. **Novikova, I., A. B. Matsko, V. L. Velichansky, M. O. Scully and G. R. Welch** (2001). Compensation of ac Stark shifts in optical magnetometry. *Phys. Rev. A* **63**, 063802.

83. **Novikova, I.** (2003a). NMOE in optically dense Rb vapour, dissertation available at http://walsworth.physics.harvard.edu/publications/2003_Novikova_TAMUPhDThesis.pdf.

84. **Novikova, I.** (2003b). The procedure to extract the contributions to HOC can be found in Novikova (2003a). It was explained by I. Novikova through private correspondence.

85. **Nye, J. F. and M.V. Berry** (1974). Dislocations in wave trains. *Proc. R. Soc. London, Series A: Math. Phys.Eng. Sci.* **336**, 165.

86. **Omont, A.** (1977). Irreducible components of the density matrix: application to optical pumping. *Prog. Quantum Electronics,* **5**, 69.

87. **Patnaik, A. K. and G. S. Agrawal** (2000). Laser field induced birefringence and enhancement of magneto-optical rotation. *Optics Comm* **179**, 97.

88. **Patnaik, A. K., S. H. Paul, G. S. Agarwal, G. R. Welch and M. O. Scully** (2007). Measurement of ground-state decoherence via interruption of coherent population trapping. *Phys. Rev. A* **75**, 023807.

89. **Phillips, D. F., A. Fleischhauer, A. Mair, R. L. Walsworth and M. D. Lukin** (2001). Storage of Light in Atomic Vapor. *Phys. Rev. Lett.* **86**, 783.

90. **Power, W. L., L. Allen, M. Babiker and V. E. Lembessis** (1995). Atomic motion in light beams possessing orbital angular momentum. *Phys. Rev. A* **52**, 479.

91. **Pugatch, R., M. Shuker, O. Firstenberg, A. Ron and N. Davidson** (2007). Topological stability of stored optical vortices. *Phys. Rev. Lett.* **98**, 203601.

92. **Purves, G. T.** (2006). Absorption and dispersion in atomic vapors: Application to interferometry, dissertation available online at http://massey.dur.ac.uk/resources/gt purves/gtp_thesis/Intro.pdf.

93. **Pustelny, S.** (2007). Nonlinear magneto-optical effects, dissertation available online at http://www.if.uj.edu.pl/pl/ZF/qnog/tutorials/DrSzymonPustelny.pdf.

94. **Ram N, Anupriya J, Pattabiraman M and Vijayan C** (2009). Role of transfer of coherence in the enhanced absorption Hanle effect with two optical fields. *J. Phys. B: At. Mol. Opt. Phys.* **42** 175504.

95. **Renzoni, F., W. Maichen, L. Windholz and E. Arimondo** (1997). Coherent population trapping with losses observed on the Hanle effect of the D_1 sodium line. *Phys. Rev. A* **55**, 3710.

96. **Renzoni, F. and E. Arimondo** (1998). Population-loss-induced narrowing of dark resonances. *Phys. Rev. A* **58**, 4717.

97. **Renzoni, F., C. Zimmermann, P. Verkerk and E. Arimondo** (2001). Enhanced absorption Hanle effect on the $F_g=F \rightarrow F_e=F+1$ closed transitions. *J. Opt. B: Quantum Semiclass. Opt.* **3** S7.

98. **Ressler, N. W., R. H. Sands and T. E. Stark** (1969). Measurement of Spin-Exchange Cross Sections for Cs^{133}, Rb^{87}, Rb^{85}, K^{39}, and Na^{23}. *Phys. Rev.* **184**, 102.

99. **Rigrod, W. W.** (1963). Isolation of axi-symmetrical optical resonator modes. *Appl. Phys. Lett.* **2**, 51.

100. **Rochester, S. M. and D. Budker** (2000). Atomic polarization visualized. *Am. J. Phys.* **60**, 450.

101. **Rochester, S. M., D. S. Hsiung, D. Budker, R. Y. Chiao, D. F. Kimball and V. V.Yashchuk** (2001). Self-rotation of resonant elliptically polarized light in collision-free rubidium vapour. *Phys. Rev. A* **63**, 043814.

102. **Rochester, S.** (2008). 'AtomicDensityMatrix' a user-extensible mathematica based atomic density matrix package, available online at *http://budker.berkeley.edu/ADM*. **Malakyan** (2004) maybe consulted for the theoretical framework used in the package.

103. **Sacherlasertechnik** (2003). http://www.sacher-laser.com. User's manual.

104. **Schawlow, A. L.** (1982). Spectroscopy in a new light. **54**, 697.

105. **Schuller. F., M. J. D. Macpherson, D. N. Stacey, R. B. Warrington and K. P. Zetie** (1991). The Voigt effect in a dilute atomic vapour. *Opt. Commun.* **86**, 123.

106. **Scully, M. O. and M. S. Zubairy** (1997). *Quantum Optics* Cambridge University Press, Cambridge, England.

107. **Seltzer, S. J., D. J. Michalak, M. H. Donaldson, M. V. Balabas, S. K. Barber, S. L. Bernasek, M.-A. Bouchiat, A. Hexemer, A. M. Hibberd, D. F. Jackson Kimball, C. Jaye, T. Karaulanov, F. A. Narducci, S. A. Rangwala, H. G. Robinson, A. K. Shmakov, D. L. Voronov, V. V. Yashchuk, A. Pines and D. Budker** (2010). Investigation of Anti-Relaxation Coatings for Alkali-Metal Vapor Cells Using Surface Science Techniques. *J. Chem. Phys.* **133**, 144703.

108. **Sobelman, I. I.** (1992). *Atomic Spectra and Radiative Transitions* Springer, Berlin.

109. **Ståhlberg, B., P. Jungner, T. Fellman and Å. Lindberg** (1990). Nonlinear forward scattering of resonant laser light from excited neon systems. *Appl. Phys. B* **50**, 547.

110. **Steck, D. A.** (2010). Rubidium 85 D Line Data, Rubidium 87 D Line Data, available online at http://steck.us/alkalidata (revision 2.1.4).

111. **Tabosa, J. W. R. and D. V. Petrov** (1999). Optical Pumping of Orbital Angular Momentum of Light in Cold Cesium Atoms. *Phys. Rev. Lett.* **83**, 4967.

112. **Taichenachev, A. V., A. M. Tumaikin and V. I. Yudin** (1999). Electromagnetically induced absorption in a four-state system *Phys.Rev. A* **61**, 011802 (R).

113. **Tamm, C. and C. O. Weiss** (1990). Bistability and optical switching of spatial patterns in a laser, *J. Opt. Soc. Am. B: Opt. Phys.* **7**, 1034.

114. **Tremblay, P. and C. Jacques** (1990). Optical pumping with two finite linewidth lasers. *Phys. Rev. A* **41**, 4989.

115. **Turchette, Q. A., C. J. Hood, W. Lange, H. Mabuchi, and H. J. Kimble** (1995). Measurement of Conditional Phase Shifts for Quantum Logic. *Phys. Rev. Lett.* **75**, 4710.

116. **Vaughan, J. M. and D. V. Willetts** (1979). Interference properties of a light beam having a helical wave surface. *Opt. Commun.* **30**, 263.

117. **Vaughan, J. M. and D. V. Willetts** (1983). Temporal and interference fringe analysis of TEM_{01}* laser modes. JOSA, Vol. **73**, 1018.

118. **Weber, H. J. and G. B. Arfken** (2005). *Essential Mathematical Methods for Physicists* Academia press, California.

119. **Wieman, C. E. and L. Hollberg** (1991). Using diode lasers for atomic physics. *Rev. Sci. Instrum.* **62**, 1.

120. **Willetts, D. V. and J. M. Vaughan** (1980). Properties of a laser mode with a helical cophasal surface. *Laser Advances and Applications*, B. S. Wherrett, ed., Wiley, New York, 1980, pp. 51.

121. **Yashchuk, V. V., D. Budker, W. Gawlik, D. F. Kimball, Yu. P. Malakyan, and S. M. Rochester** (2003). Selective addressing of high-rank atomic polarization moments. *Phys. Rev. Lett*. 90, 253001.

LIST OF PAPERS BASED ON THESIS

1. Hanle electromagnetically induced transparency and absorption resonances with a Laguerre Gaussian beam, J. Anupriya, Nibedita Ram and M. Pattabiraman, *Phys Rev A* **81** 043804 (2010).

CONFERENCE PRESENTATIONS

1. Hanle electromagnetically induced transparency and absorption resonances with a Laguerre Gaussian beam, J. Anupriya, Nibedita Ram and M. Pattabiraman, Poster presented at Third international conference on "Current Developments in Atomic, Molecular, Optics and Nano Physics" (CDAMOP- 2011), University of Delhi, New Delhi, December 2011.

2. Role of transfer of coherence in Enhanced Absorption Hanle effect with two optical fields, Nibedita Ram, J. Anupriya, M. Pattabiraman and C. Vijayan, Poster presented at Topical Conference on "Interaction of EM Radiation with Atoms, Molecules and Clusters" (TC-2010), RRCAT Indore, March 2010.

3. Study of Laguerre Gaussian beam induced azimuthal Doppler shift using saturation absorption spectroscopy, J. Anupriya, Nibedita Ram and M. Pattabiraman, Poster presented at DAE-BRNS symposium on "Atomic, Molecular and Optical Physics", Inter University Accelerator centre, New Delhi, February 2009.

DOCTORAL COMMITTEE

Chairman:	Head, Department of Physics
Academic Guide:	Dr. M. Pattabiraman, Department of Physics
Members:	Dr. V. Sankaranarayanan, Department of Physics
	Dr. M. V. Satyanarayana, Department of Physics
	Dr. Anil Prabhakar, Department of Electrical Engineering
	Dr. Mangala Sunder Krishnan, Department of Chemistry